UNIVERSITY OF OKLAHOMA

GRADUATE COLLEGE

CYCLOPENTANONE ALDOL CONDENSATION

EFFECTS OF SURFACE SILANIZATION, ACETONE AND WATER CO-FEEDING

ON CATALYTIC BEHAVIORS OF MAGNESIUM OXIDE-BASED SOLIDS

A DISSERTATION

SUBMITTED TO THE GRADUATE FACULTY

in partial fulfillment of the requirements for the

Degree of

DOCTOR OF PHILOSOPHY

By

DUONG T. NGO

Norman, Oklahoma

2018

CYCLOPENTANONE ALDOL CONDENSATION

EFFECTS OF SURFACE SILANIZATION, ACETONE AND WATER CO-FEEDING

ON CATALYTIC BEHAVIORS OF MAGNESIUM OXIDE-BASED SOLIDS

A DISSERTATION APPROVED FOR THE

SCHOOL OF CHEMICAL, BIOLOGICAL AND MATERIALS ENGINEERING

BY

Dr. Daniel E. Resasco, Chair

Dr. Steven P. Crossley

Dr. Lance L. Lobban

Dr. Jeffrey H. Harwell

Dr. Elizabeth C. Butler

Acknowledgments

First and foremost, I would like to express my sincere gratitude to Dr. Daniel Resasco, my advisor during the 5-year Ph.D. program at the University of Oklahoma. His deep knowledge and outstanding experience have motivated me to explore and master the field of heterogeneous catalysis. Moreover, thanks to Dr. Resasco's precious advice, I have truly learned how to write scientific papers and perform oral presentations professionally. Thereafter, I would like to thank Dr. Steven Crossley, Dr. Lance Lobban, Dr. Jeffrey Harwell, Dr. Elizabeth Butler and Dr. Daniel Glatzhofer for serving my Ph.D. committee. My appreciation is then to Dr. Tawan Sooknoi, Dr. Bin Wang and Dr. Qiaohua Tan, the co-authors of my published papers. I would also like to acknowledge Dr. Preston Larson and Dr. Andrew Madden for characterization measurements, along with all lecturers in my graduate courses.

Next, I want to thank my colleagues at School of Chemical, Biological and Materials Engineering (Gallogly College of Engineering, the University of Oklahoma). It was my pleasure to work with talented and energetic people, especially Tu Pham, Nhung Duong, Gengnan Li, Tania Vitery, Puridej Warakunwit, Zheng Zhao, Lawrence Barrett and Felipe Anaya. Another credit goes to Basic Energy Sciences (Office of Science, the U.S. Department of Energy) for financial support. Such funding guaranteed not only my research progress but also the quality of studies.

Finally, I would like to dedicate this work to my beloved family, where I have been raised and educated since childhood. Despite starting the Ph.D. program with much

interest and ambition, I was soon surrounded by difficulties and challenges. My research in fact resembled a fluctuating sine wave rather than a route decorated with high notes. Whenever I felt depressed or vitalized, family was always the first place to share emotions and seek for encouragement. After each morale-boosting talk, I became more confident and determined to pursue long-term projects. The unconditional help from family did provide me with both physical and mental strengths to accomplish this dissertation, a memorable milestone of my life.

Norman, Oklahoma

United States of America

November 16th, 2018

Duong Ngo

Table of Contents

List of Tables

List of Figures

Abstract

Cyclopentanone is a promising building block in the conversion of biomass to fuels. It can be readily obtained from furanics derived from biomass and can be converted to intermediate products in the molecular weight range compatible with fuels via C-C bond forming reactions. Among them, aldol condensation is a promising route. Conventional MgO catalysts are intrinsically active to catalyze this reaction, but they usually exhibit low surface areas and low stability in the presence of liquid water. The nitrate-citrate combustion method results in high-surface-area oxides with high condensation activity, but they are still susceptible to water attack. Here, hydrophobic MgO-based catalysts functionalized with octadecyltrichlorosilane (OTS) are shown to exhibit remarkable stability in the liquid phase under conditions in which a conventional MgO deactivates in short time.

The second topic addresses another important biomass upgrading process: the cross-aldol condensation of cyclopentanone (C) and acetone (A), the latter derived from the ketonization of acetic acid. The four primary products, especially 2-cyclopentylidenecyclopentanone ([C]C) and 2-isopropylidenecyclopentanone ([C]A), can be hydrodeoxygenated into high octane-numbered hydrocarbons. Here, the cross-aldol condensation is catalyzed by MgO-NC, the unmodified solid prepared via nitrate-citrate combustion. Initial rates at 200°C with various A-to-C feed ratios indicate the dominance of [C]-activated products. These runs, combined with DFT calculations and adsorption measurements, confirm both the preferential chemisorption and α-H abstraction of

cyclopentanone on an MgO surface with respect to acetone. For each ketone reactant, α-H abstraction is rate-limiting as the total rate of formation of [C]-activated products remains constant, while that of [A]-activated products increases proportionally to the A-to-C feed ratio. The product distribution – particularly [C]A-to-[C]C ratio – is however controlled by subsequent C-C coupling equilibria, along with molar concentrations of A and C in cyclohexane.

The third topic provides details on how external water affects an MgO-catalyzed cyclopentanone self-aldol condensation. It is first found that a high OTS loading on MgO changes the rate-limiting step from α-H abstraction to C-C coupling, mostly due to increasing steric hindrance. Regarding water responses, the initial rate on hydrophilic MgO-NC drops rapidly along added water amounts simply due to site blockage. For hydrophobic MgO-OTS, this initial rate is appreciably improved in water vapor and only decreases in excess liquid water. It is proposed that surface OTS molecules drastically depopulate active sites for cyclopentanone chemisorption, but the catalytic activity can be partially recovered by Mg^{2+}-bound water clusters. These clusters can polarize free cyclopentanone molecules through hydrogen bonds, thus lowering the energy barrier for C-C coupling. Such water assistance is only observed when MgO is functionalized with OTS. Octadecyl-less post-calcined MgO-OTS is shown to experience a sharp rate drop, similar to the one observed on silane-free MgO-NC.

Keywords

- aldol condensation

- cyclopentanone

- acetone

- water

- co-feeding

- magnesium oxide

- nitrate-citrate combustion

- deactivation

- functionalization

- hydrophobization

- octadecyltrichlorosilane

- nucleophilic addition

- chemisorption

- α-H abstraction

- C-C coupling

1. Improving stability of cyclopentanone self-aldol condensation MgO-based catalysts by surface hydrophobization with organosilanes

1.1. Introduction

The combination of multistage thermal conversion of biomass and a catalytic cascade of C-C bond forming reactions followed by hydrodeoxygenation appears as an attractive strategy for the production of biomass-derived fuel components [1-5]. This strategy minimizes several drawbacks found in the more conventional pyrolysis/hydrotreating approach [6-10]. Furfural is among the most abundant components obtained from this multistage thermal conversion process [2]. While furfural is by itself an economically important aldehyde used in the synthesis of various chemicals [11-14], it is rather unstable and prone to coke formation, which causes rapid catalyst deactivation during upgrading. Recently, Hronec and co-workers [15,16] have called attention to an appealing path to produce a much more stable intermediate, cyclopentanone (**Figure 1**). That is, under hydrogen atmosphere and in the presence of water, furfural can be converted to cyclopentanone via the Piancatelli rearrangement combined with a two-step selective hydrogenation, before and after the arrangement; i.e., first, the -CO group in furfural is hydrogenated to –OH and then, the C=C double bond in cyclopentenone is saturated [17-21]. As a potential coupling agent, this non-toxic cyclic ketone has been utilized in the alkylation of phenolic compounds and, more particularly, the self-aldol condensation followed by hydrodeoxygenation to form bicyclopentyl, a promising fuel component [22]. A few attempts to optimize the catalysts that maximize C_5-C_5 coupling have been described

in the literature, using both solid acids and solid bases [23,24]. Yang *et al.* [25] investigated the self-condensation of pure cyclopentanone at 150°C on basic hydrotalcites and alkaline earth metal oxides and found high yields to 2-cyclopentylidenecyclopentanone. Likewise, Liang *et al.* [26] reported 100% selectivity to this dimer at 80% conversion over an MgO-ZrO$_2$ catalyst at 130°C and 1 atm. Other authors have also used cyclopentanone as a co-reactant with aldehydes to obtain a broader range of fuel-resembling intermediates. For example, the combination of cyclopentanone and furfural has been proposed by Ordonez *et al.* [27], using MgO-ZrO$_2$ as a catalyst operating under mild reaction conditions (20 - 50°C) in an aqueous phase. At all furfural/cyclopentanone molar ratios (1:1 to 10:1), only cross-condensates were obtained due to the high affinity of furfural and the catalyst surface. Similarly, 2-cyclopentylidenecyclopentanone was also absent from the product mixtures in the study by Huber's group [28], who used solvent-free conditions for the reaction between cyclopentanone and butanal at 140°C. Despite excess amounts of cyclopentanone and excellent activity of the solid base MgAl-HT, only cross-condensation products were obtained with 80% selectivity to cyclopentanone-activated adducts. Due to the very high yields and selectivity in which cyclopentanone can be produced from furfural [15,16], it is still interesting to investigate the production of the stable compound bicyclopentyl which may have desirable fuel properties [29,30].

The base-catalyzed self-condensation of cyclopentanone follows a nucleophilic addition (A$_N$) mechanism, in which the first step is the generation of an enolate intermediate resulting from the abstraction of a proton by the basic site from the C in the α position [31]. The second step that involves the C-C bond formation may occur either via

reaction of an adsorbed molecule and a molecule in the fluid (Eley-Rideal model) or via a bimolecular surface reaction (Langmuir-Hinshelwood model). In the first case, the enolate is bound to the surface while the electrophile is in the fluid phase [32,33]. By contrast, in the second case, the electrophile is also adsorbed [34]. The subsequent steps are C-C coupling, reprotonation, and dehydration. The resulting dimeric product (2-cyclopentylidenecyclopentanone) is also able to donate a proton to the surface for another condensation step that yields the trimeric product 2,5-dicyclopentylidenecyclopentanone.
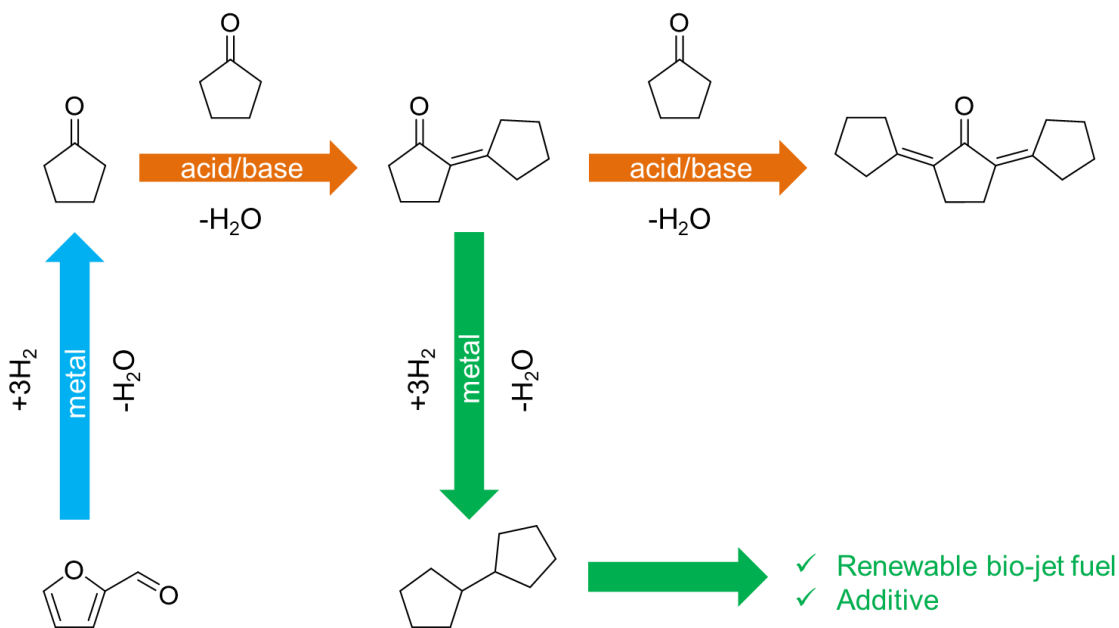
Figure 1. Cyclopentanone self-aldol condensation as an intermediate process in upgrading biomass-derived furfural.

MgO is a typical basic oxide commonly used in aldol-condensation and widely investigated [35]. While it is beneficial to enhance the surface area of MgO for higher reaction rates, this enhancement also increases the uptake of undesirable nucleophiles such as water and product oligomers, which accelerate deactivation, as shown in several studies [25,36-38]. Finding catalytic materials that are effective for aldol condensation and at the same time more resistant to deactivation than conventional basic catalysts is an appealing objective. Therefore, the main goal of this contribution has been investigating novel materials with improved stability during aldol condensation. We have found that MgO modified with mesoporous silica and subsequently grafted with an organosilane (e.g. octadecyltrichlorosilane) [39,40] that renders the surface hydrophobic greatly improves catalyst stability.

1.2. Experimental

1.2.1. Synthesis of catalytic materials

1.2.1.1. Combustion method

MgO-NC. A mixture of 25.6 g of $Mg(NO_3)_2.6H_2O$ (Aldrich, 99.9 %, 0.1 mol) and 30 mL of water was stirred vigorously for 15 mins at 80^oC. Then, a solution containing 19.2 g of citric acid (Aldrich, 99.5 %, 0.1 mol) in 20 mL of water was added to the mixture, which was continuously heated and stirred until half of the liquid vaporized, leaving a viscous gel. This gel was subsequently calcined overnight under static air at 550^oC, during which time, combustion of citric acid took place, producing a characteristic fluffy, high-

surface-area MgO material [41 , 42], noted here as MgO-NC (for nitrate-citrate combustion).

1.2.1.2. Hydrophobization method

MgO@mSiO₂ composite.   As demonstrated in previous investigations of analogous materials based on TiO_2 photo-oxidation catalysts [43,44], it is possible to enhance the overall surface area without complete blockage of the TiO_2 active sites [45]. To prepare this hybrid material, 2 g of the parent MgO-NC were stirred vigorously for 15 mins at room temperature in a mixture of 4 mL of NH_4OH (50% v/v) and 40 mL of water. Subsequently, a 0.1 M solution of cetyltrimethylammonium bromide (CTAB) in a 1:2 vol. ratio of ethanol-water was added to the suspension, while continuously stirring for 30 mins. Then, variable amounts of tetraethyl orthosilicate (TEOS) were introduced dropwise. The resulting suspension was stirred overnight, centrifuged, and washed 3 times with ethanol. The separated solid was dried at 100ºC overnight and calcined under static air at 400ºC for 6 hours to obtain the MgO@mSiO₂ composite.

Functionalization with octadecyltrichlorosilane (OTS). The following method was used to hydrophobize the MgO-based materials. First, 0.45 mL of water was dropped onto 1 g of MgO-NC or MgO@mSiO₂, and the resulting wet solid was suspended in a 1:50 v/v OTS-toluene solution.   Then, the suspension was shaken for 5 mins and stirred overnight, followed by centrifugation and 3 washes with ethanol. The separated solid was finally dried overnight at 110ºC to yield MgO-OTS (or MgO@mSiO₂-OTS), in which OTS has reacted with surface OH groups to generate a hydrophobic surface.

In this paper, we prepared two types of $MgO@mSiO_2$-OTS and one type of MgO-OTS with nominal compositions of (49 wt.% MgO – 21 wt.% SiO_2 – 30 wt.% OTS), (74 wt.% MgO – 10 wt.% SiO_2 – 16 wt.% OTS) and (70 wt.% MgO – 30 wt.% OTS) respectively. The catalyst with the first nominal composition, which was mainly used to study the catalytic activity and stability, would be mostly referred to as $MgO@mSiO_2$-OTS for sake of simplicity.

1.2.2. *Characterization*

The final content of OTS in the $MgO@mSiO_2$-OTS sample was determined by thermogravimetric analysis (TGA). As MgO and SiO_2 are thermally stable under air, only OTS was quantitatively oxidized to CO_2 and H_2O, which were quantified by MS/TGA. For this purpose, 47.48 mg of $MgO@mSiO_2$-OTS was analyzed by heating with a linear ramp under flow of an Ar-air mixture, starting from $40^{o}C$ and increased by $2^{o}C.min^{-1}$.

Specific surface areas for samples of MgO-NC, $MgO@mSiO_2$, MgO-OTS, $MgO@mSiO_2$-OTS, and commercial MgO were obtained on a Micromeritics 2010 instrument. The value obtained for $MgO@mSiO_2$ was combined with mass spectra obtained during the TGA of $MgO@mSiO_2$-OTS to quantify the distribution of OTS functionalities on the catalyst. For sake of simplicity, we assume complete hydrolysis of the chloro-groups in OTS and monodentate anchoring. Accordingly,

$$x = \frac{n_{OTS} \times N_A}{A_{MgO@mSiO_2}} = \frac{\frac{m_{C_{18}H_{37}Si(OH)_2O^-}}{MW_{C_{18}H_{37}Si(OH)_2O^-}} \times N_A}{m_{MgO@mSiO_2} \times S_{BET\ MgO@mSiO_2}}$$

or

$$x = \frac{\dfrac{m_{C_{18}H_{37}Si(OH)_2O-}}{MW_{C_{18}H_{37}Si(OH)_2O-}} \times N_A}{\left[1 - m_{C_{18}H_{37}Si(OH)_2O-}\right] \times S_{BET\ MgO@mSiO_2}}$$

where

x	=	molecules of OTS, or $C_{18}H_{37}Si(OH)_2O-$, anchored per unit area of $MgO@mSiO_2$ in $MgO@mSiO_2$-OTS
$m_{C_{18}H_{37}Si(OH)_2O-}$	=	TGA-based content of OTS in $MgO@mSiO_2$-OTS [g.g catalyst^{-1}]
$m_{MgO@mSiO_2}$	=	TGA-based content of $MgO@SiO_2$ in $MgO@mSiO_2$-OTS [g.g catalyst^{-1}]

The morphology of MgO-NC was analyzed by TEM (Zeiss 10A). An SEM image of the final $MgO@mSiO_2$-OTS product was recorded in backscattered electron mode, combined with EDS analysis to determine whether the OTS had been fully hydrolyzed. X-ray diffraction (XRD) was used to confirm the presence of crystalline MgO in the solid prepared by the nitrate-citrate combustion.

The basicity of $MgO@mSiO_2$-OTS was characterized via temperature-programmed desorption (TPD) of adsorbed CO_2 following the method described elsewhere [46]. Briefly, in each run, 100 mg of $MgO@mSiO_2$-OTS was heated to 200°C in the TPD system with a ramp rate of 10°C.min^{-1}, under a He flow rate of 30 mL.min^{-1} and then cooled down to room temperature. A CO_2 flow rate of 30 mL.min^{-1} was then passed through the sample for 30 mins, followed by a 2-hour purge with He to remove any physisorbed CO_2.

The TPD was performed under the same He flow rate by heating to 600°C with a ramp rate of 10°C.min^{-1}.

1.2.3. Catalytic measurements

1.2.3.1. Aldol condensation under N_2

In each run, the solid catalyst (MgO-NC or MgO@mSiO$_2$-OTS) suspended in cyclohexane was placed into a 100-mL Parr reaction vessel. Before reaction, the system was purged with N_2, pressurized to 300 psia and heated to 150 – 200°C. The cyclopentanone reactant was placed in a 30-mL feeding cylinder, pressurized to 450 – 500 psia of N_2 along with an internal standard (toluene) and then injected into the reaction system, as soon as the desired temperature was stabilized. Reaction runs were carried out under a stirring speed of 750 rpm for a given reaction time. All liquids were analyzed by GC-MS and GC-FID as previously described [47].

1.2.3.2. Aldol condensation under H_2

Following a recently proposed approach [48], some of the aldol condensation runs were conducted in the presence of a Cu/SiO$_2$ catalyst under H_2. This method has shown to be effective in minimizing deactivation in the aldol condensation of acetone in the vapor phase [49]. In our case, 250 mg of 10 wt.% Cu/SiO$_2$ were placed into the 100-mL Parr reactor vessel along with the MgO-NC catalyst and the cyclohexane solvent. The system was then heated to 270°C for 3 hours under 500 psia of H_2 and cooled down to the reaction temperature of 150°C. The cyclopentanone feed was pressurized up to the target H_2

8

pressure in a 30-mL feeding cylinder along with toluene. As above, when the desired reaction temperature was stabilized, the feed was injected into the reaction system.

1.2.3.3. *Quantification of the extent of catalyst deactivation*

Catalyst deactivation during aldol condensation reactions is a common problem, which has been observed in numerous studies [25]. A common practice to model catalyst deactivation is to use an exponential decay of activity with time (t) according to the expression $a = a_0 \, e^{-k_D \, t}$, where k_D is the deactivation parameter, larger for rapidly deactivating cases and smaller for more stable catalysts. In a steady state, flow reactor, determining k_D is rather straightforward. However, evaluating deactivation in a batch reactor is much more complicated than on a flow reactor since the concentration C continuously changes, and both deactivation and reaction kinetics affect the variation of C with time. An effective method for comparing rates of deactivation in a batch reactor has been described by Apesteguia *et al.* [50,51]. In this method, the evolution of reactant concentration is plotted as a function of the product of catalyst mass and time (w x t) for two different amounts of catalyst. When there is no deactivation, the curves on the plot should coincide, but when the catalyst deactivates with time, the curves reach a plateau at different concentration values. That is, with a smaller amount of catalyst, a longer time is necessary to reach a certain conversion, thus the catalyst experiences more pronounced deactivation than in a run with a larger amount of catalyst, which for the same conversion has required a shorter period of time, with consequently lower extent of deactivation. The more different the curves with varying catalyst amounts are, the stronger the extent of

deactivation is. By contrast, when there is no deactivation, the curves for the two runs should be coincident.

1.2.3.4. Reusability of MgO@mSiO$_2$-OTS

In addition to the deactivation test using C vs. (w x t) graphs, the stability of MgO@mSiO$_2$-OTS was evaluated by re-using the catalyst in consecutive runs. In this experiment, 500 mg of MgO@mSiO$_2$-OTS was used for the first 2-hour reaction at 200°C. After each cycle, the spent catalyst was washed with acetone, dried at 100°C and saved for the next cycle, keeping the same reaction conditions. Evolution of conversion as a function of reaction cycle gave an estimate of the catalyst stability.

1.3. Results

1.3.1. Materials characterization

As depicted in **Figure 2**, the TGA of MgO@mSiO$_2$-OTS exhibits two distinct mass losses. The first one, from 40 to 200°C, can be ascribed to the evolution of water – physically adsorbed on the surface; the second loss, with a maximum at about 410°C, is clearly due to the combustion of the functional groups in air. By quantifying the evolution of CO$_2$ and H$_2$O in this region, with the assumption that Cl is no longer present in the silanized surface and Si is not evolved during TGA, one can calculate the original loading of OTS in the as-prepared catalyst. The resulting value is about 20 wt.%, which is lower than the nominal 30 wt.% initially incorporated in the preparation, indicating that a fraction of the OTS initially added to the material is not effectively anchored and is lost during the

10

post-synthesis washing steps in ethanol and centrifugation. However, the rest is strongly anchored and can resist relatively high temperatures before decomposition.
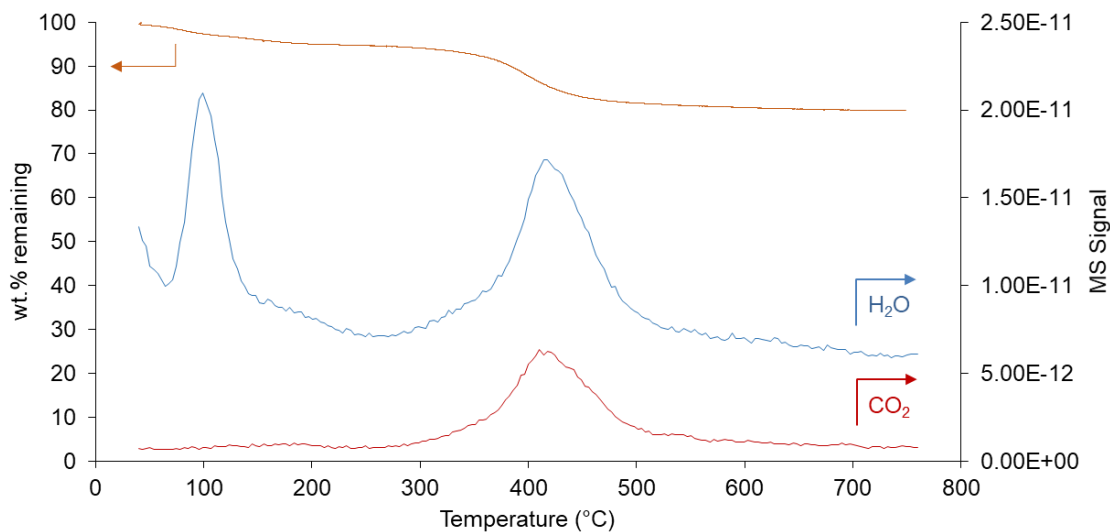
Figure 2. TGA analysis and associated mass spectra of water and CO_2 evolved from the MgO@mSiO$_2$-OTS sample as a function of temperature.

Table 1 summarizes the specific surface areas of the various materials investigated. The MgO-NC sample prepared by the combustion method exhibits a surface area of almost 100 $m^2.g^{-1}$, more than fifty times greater than that of most commercial MgO samples, demonstrating the effectiveness of the nitrate-citrate combustion method to generate oxide particles of small size. This value is further enhanced when the MgO particles are incorporated onto the structure of mesoporous silica. As shown below, when heated in the presence of mesoporous silica, the MgO particles redisperse and partially lose their crystallinity. Even more important for this work, a relatively high surface area is still

retained on the hybrid material after functionalization with OTS. By substituting the TGA-based OTS content of MgO@mSiO$_2$-OTS and the BET surface area of MgO@mSiO$_2$ into the equation in **Section 1.2.2**, we have found that there is approximately one molecule of OTS attached to a nm^2 of MgO@mSiO$_2$, or as defined above x = 1 nm^{-2}.

Table 1. Surface area, pore size, and pore volume of various MgO catalysts.

Catalyst	S$_{BET}$	Pore diameter	Pore volume
	m^2.g^{-1}	nm	cm^3.g^{-1}
MgO (commercial)	1.5	-	-
MgO-NC	97	9.5	0.22
MgO@mSiO$_2$	448	7	0.80
MgO-OTS	51	3.8	0.04
MgO@mSiO$_2$-OTS	173	4.8	0.19

Figure 3 shows the pore size distribution of the four samples. The original MgO material is composed of aggregates of non-porous MgO crystallites (**Appendix A**). Thus, the observed porosity is simply due to interparticle void spaces in the aggregates. Clearly, the incorporation of MgO onto the mesoporous silica enhances the overall porosity of the material and this porosity is partially retained upon functionalization with OTS.
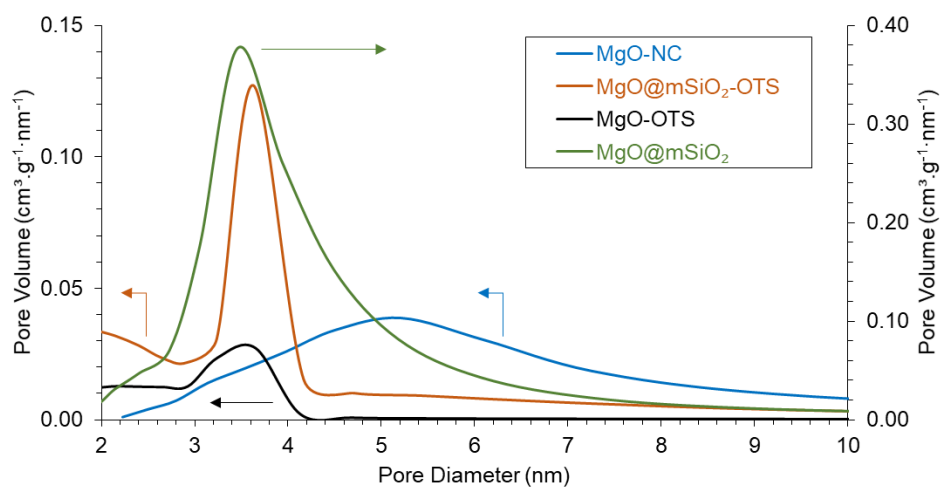
Figure 3. Pore size distribution of functionalized MgO catalysts compared to the parent MgO prepared by combustion (MgO-NC).

To further characterize the structure of the different materials investigated, XRD was conducted on the three samples: MgO-NC, MgO@mSiO$_2$ and MgO@mSiO$_2$-OTS.
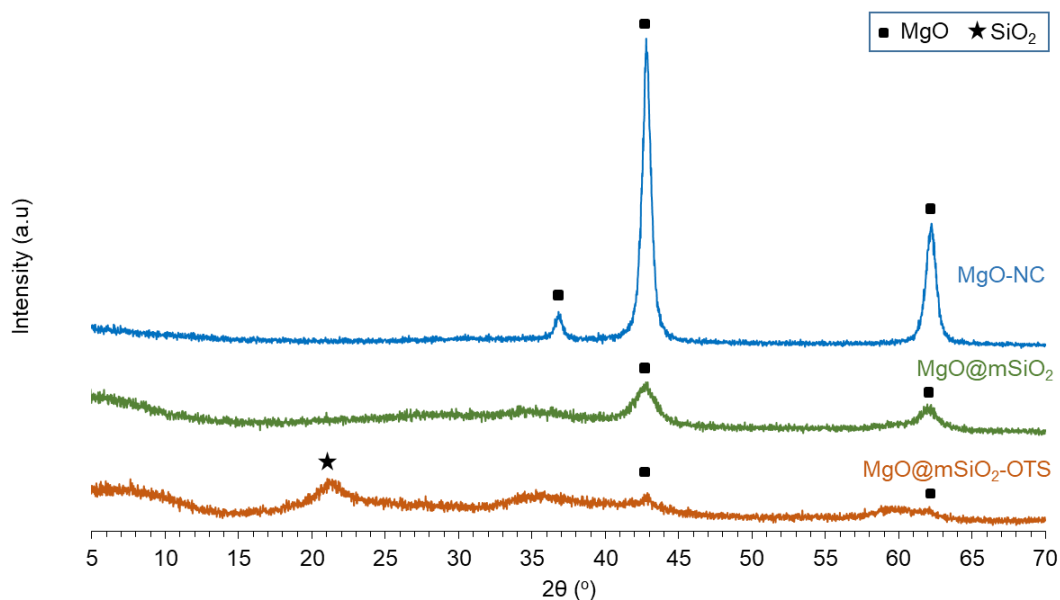
Figure 4. XRD patterns of functionalized MgO catalysts compared to the parent MgO.

As shown in **Figure 4**, the MgO-NC sample shows the typical XRD pattern of crystalline MgO (37.2^{o}, 43.0^{o} and 62.3^{o}), thus verifying the identity and purity of MgO prepared via the nitrate-citrate combustion. By contrast, the subsequent method of incorporating the mesoporous silica into the system causes a drastic loss in crystallinity of MgO. As seen in the XRD pattern for the $MgO@mSiO_2$, the peak intensity is largely reduced and the peak width is broadened. That is, the vigorous stirring in aqueous NH_4OH, followed by interaction with TEOS and surfactant and final calcination at $400^{o}C$, used to generate the hybrid $MgO@mSiO_2$ material may cause significant alterations in the morphology and crystallinity of the MgO particles, resulting in redispersion and spreading of the MgO particles onto the silica surface. It is possible that during this procedure MgO may partially dissolve, re-precipitate, and perhaps interact with SiO_2 forming highly dispersed MgO domains. In fact, the elemental mapping obtained by EDS/SEM analysis (**Appendix A**) shows a very uniform distribution of Mg and Si. During the functionalization with OTS, the low crystallinity of $MgO@mSiO_2$ experiences a further decline, as indicated by the even lower intensity and further broadening of the MgO peaks.
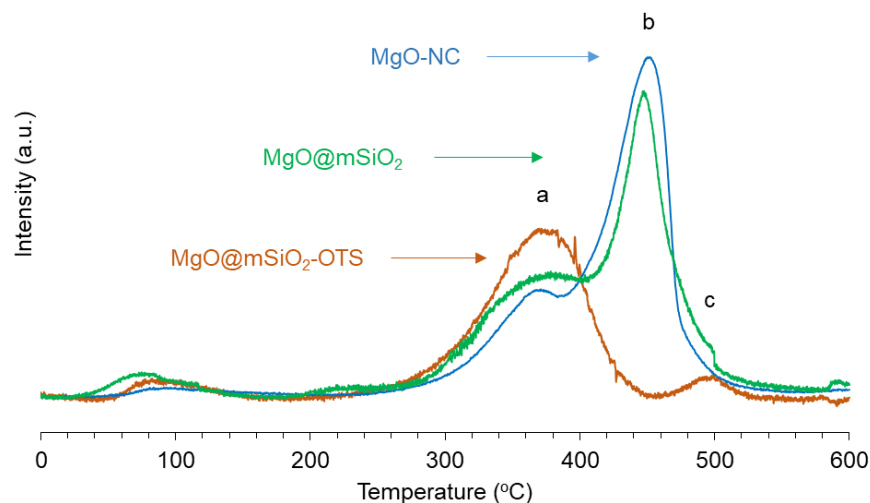
Figure 5. CO_2-TPD on MgO-NC, MgO@mSiO$_2$ and MgO@mSiO$_2$-OTS.

To quantify the density of basic sites on the samples, we used the conventional TPD of adsorbed CO_2. As shown in **Figure 5**, the MgO-NC sample exhibits two major desorption peaks, a smaller one centered at around 375°C and a dominant peak centered at around 450°C. In agreement with our previous report [46], this sample has a basic site density of 420 µmol.g^{-1}. The MgO@mSiO$_2$ sample exhibits a very similar TPD profile to that of MgO-NC, with a total basic site density of 390 µmol.g^{-1}, indicating that despite the dramatic changes in the topology of MgO, its surface chemistry remains unchanged after incorporation onto the silica surface. However, almost all sites of high basicity strength are eliminated following OTS treatment, leaving a reduced basic density of 240 µmol.g^{-1}. Particularly, most of the sites accessible to CO_2 are in the region of intermediate basicity strength (i.e., the peak centered at 375°C), while only a small desorption peak remains at around 500°C, reflecting the presence of a small amount of strong basic sites.

MgO@mSiO$_2$-OTS was subsequently tested for buoyancy in water. A few particles of this catalyst was dispersed into 5 mL of water and stirred at 750 rpm for 10 mins. **Figure 6** shows that MgO@mSiO$_2$-OTS consistently retains on top of the free surface despite several mixing attempts. Such response further indicates that the as-prepared MgO@mSiO$_2$-OTS catalyst is highly hydrophobic.
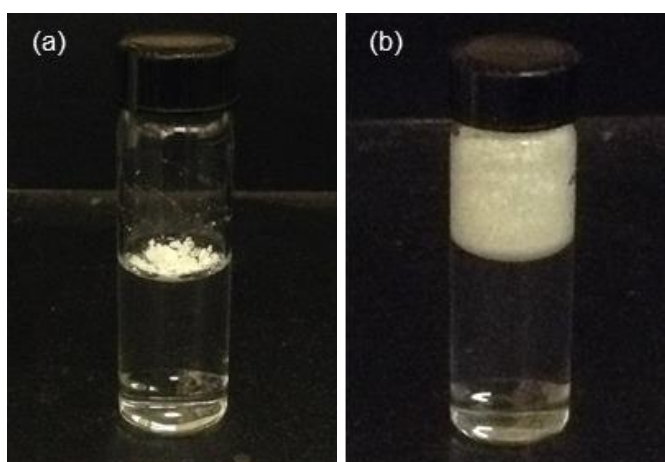
Figure 6. Buoyancy of MgO@mSiO$_2$-OTS in water.

(a) Before mixing. (b) After mixing.

Conditions: 10 mg dispersed in 5 mL of water, 750 rpm, 10 mins.

1.3.2.   Catalytic measurements

1.3.2.1.   Apparent reaction order
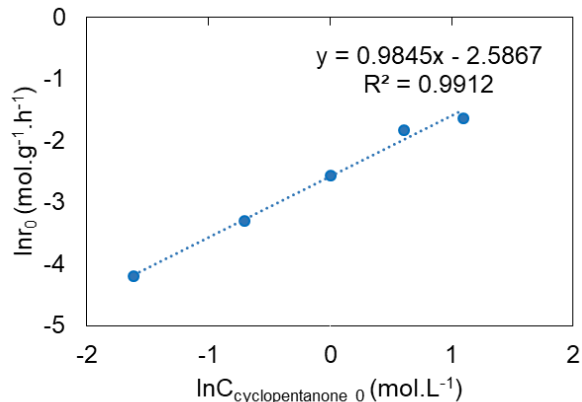
Figure 7. Apparent reaction order for cyclopentanone self-aldol condensation from

initial rate measurements.

 Reaction conditions: 0.25 g of MgO-NC, 50 mL of feed, 150°C, 450 psia in N_2, 20 mins.

In a batch reactor, it is important to decouple the kinetics from the catalyst

deactivation. Therefore, to obtain the true reaction order, initial rates of cyclopentanone

self-aldol condensation were determined in 20-min runs over the MgO-NC catalyst at a

constant temperature (150°C) and varying initial concentrations of cyclopentanone. As

shown in **Figure 7**, the ln(initial rate) vs. ln(initial concentration) plot gives a straight line

of a slope near 1.0, clearly showing the first order dependence of this reaction. This

apparent order, displayed through a broad range of initial concentrations (0.2 M to 3.0 M),

might suggest a unimolecular elementary step as the rate-determining step. As mentioned

above, the solid base-catalyzed A_N mechanism consists of aldehyde/ketone adsorption, α-

proton abstraction (enolate formation), C-C coupling, surface proton abstraction

17

(reprotonation), dehydration and product desorption. Among these steps, aldehyde/ketone adsorption, enolate formation and product desorption follow first-ordered kinetics. In several cases, such as the gas phase self-aldol condensations of propanal or acetone on anatase, enolate formation has been found to be rate-limiting [48]. Other rate-determining steps have been proposed in the literature to explain both, first- [52] and second-ordered kinetics [53,54].

1.3.2.2. Catalyst deactivation

To determine the extent of catalyst deactivation in the batch reactor, we followed the method described above [50,51] and plotted the variation of reactant concentration as a function of the catalyst mass x time product (w x t) using two different catalyst masses, namely w and 2w. As shown in **Figure 8a**, the curves for the as-prepared MgO-NC catalyst at 150°C grow clearly apart as a function of w x t, indicating a rather large extent of catalyst deactivation. Clearly, the concentration of cyclopentanone no longer changes after a relatively short reaction time.
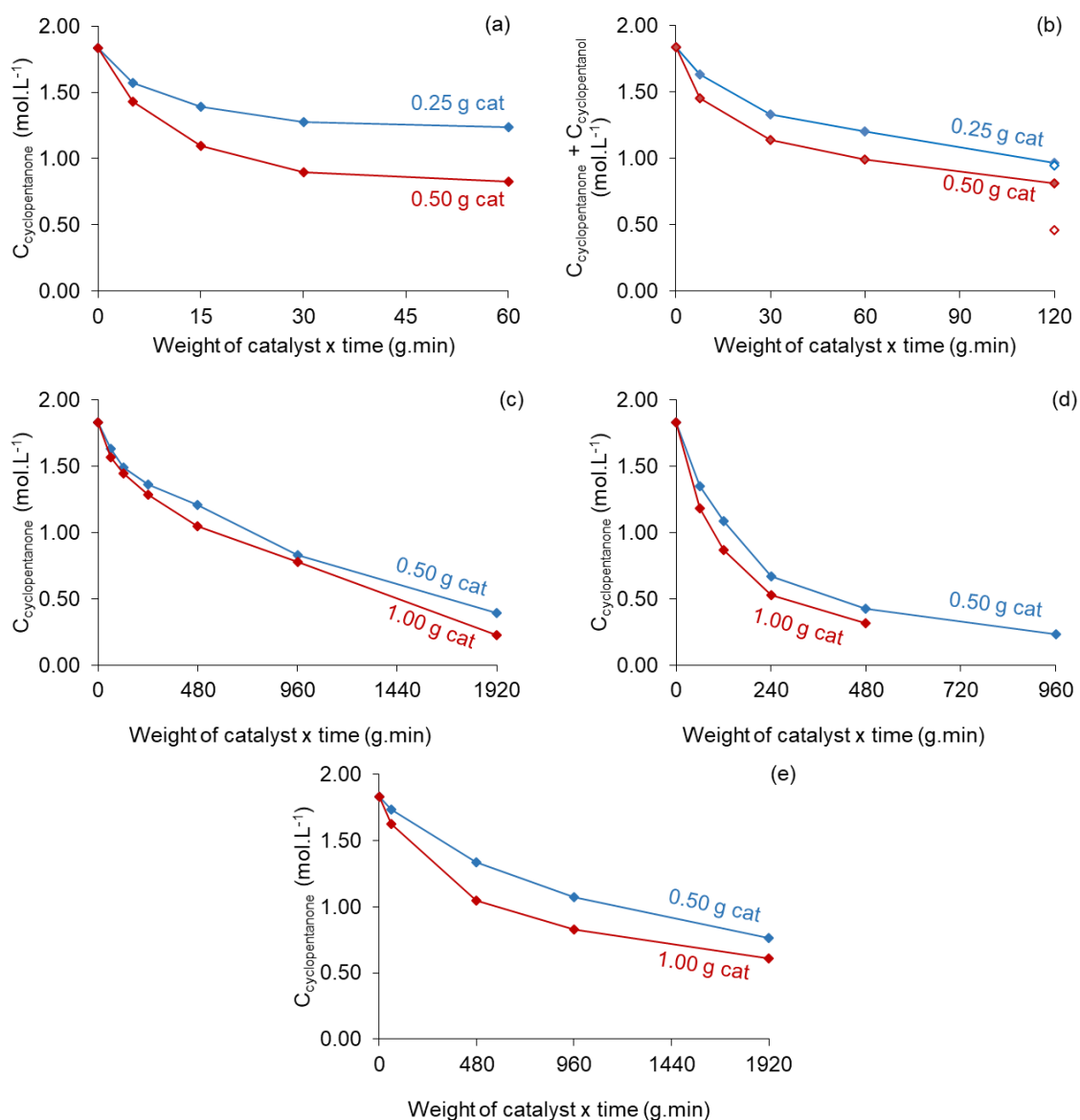
Figure 8. Evolution of concentration with reaction time as a function of the product (weight x time) over various MgO catalysts (with w and 2w) to assess catalyst deactivation.

(a) MgO-NC at 150°C. (b) MgO-NC + 0.25 g of 10 wt.% Cu/SiO_2 (H_2) at 150°C. Solid symbols – 400 psia in H_2. Open symbols – 20 psia in H_2. (c) MgO@mSiO_2-OTS at 150°C. (d) MgO@mSiO_2-OTS at 200°C. (e) MgO-OTS at 150°C.

To reduce the extent of deactivation, we conducted the reaction in the presence of 400 psia of H_2 with the addition of a Cu/SiO_2 co-catalyst to the liquid mixture. As seen in **Figure 8b**, the gap between the two curves clearly narrows, indicating a lower extent of deactivation. As previously proposed [48], the presence of Cu/SiO_2 as a hydrogenation catalyst may saturate the C-C double bond of the product and a portion of the carbonyls to non-polymerizable ketones and alcohols, thus reducing coke formation. This explanation is supported by the observed product distribution (**Appendix B**) after 8 hours, in which 2-cyclopentylcyclopentanone and 2-cyclopentylcyclopentanol are dominant C_{10} products. A shortcoming of this approach is the conversion of the cyclopentanone reactant to cyclopentanol in the presence of H_2, which leads to lower yields of the desired condensation product. By contrast, using a much lower H_2 pressure as that used in the gas phase experiments [49] results in a higher rate of catalyst deactivation. In fact, as shown in **Figure 8b**, a large gap is observed between the conversions reached with 0.25 and 0.50 grams of the catalyst after 480 and 240 mins, respectively, for the runs conducted under 20 psia of H_2 on MgO-NC. As shown in **Appendix C**, while operating at this low pressure reduces the formation of cyclopentanol, allowing a higher concentration of the feed, the formation of the unsaturated dimer (2-cyclopentylidenecyclopentanone) is still observed, which may result in catalyst deactivation by coking.

Therefore, for the cyclopentanone self-aldol condensation reaction, the simultaneous incorporation of H_2 and a hydrogenation catalyst may be detrimental to the rate of condensation. On the other hand, the hydrophobically modified catalysts MgO-OTS and MgO@mSiO$_2$-OTS show remarkable stability, even in the absence of H_2.

As can be seen in **Figure 8c** and **Figure 8d**, the curves of different catalyst masses for MgO@mSiO$_2$-OTS lie remarkably close, verifying the small extent of catalyst deactivation at both 150 and 200°C. This is remarkable since the non-functionalized catalyst deactivates even faster at the higher temperatures. Interestingly, as illustrated in **Figure 8e**, an increase in catalyst stability is also observed when the hydrophobization was directly conducted over the bare MgO substrate. In fact, as shown in **Figure 9a**, within the first 8 hours the catalytic performance of MgO-OTS is almost the same as that of MgO@mSiO$_2$-OTS. Beyond this time, MgO@mSiO$_2$-OTS shows a higher stability.

Figure 9b makes a direct comparison of the change in reaction rate for the three catalysts. The unmodified MgO-NC exhibits much greater initial rates than the functionalized catalysts. However, the rate becomes essentially zero after less than 2 hours. By contrast, while the initial rates over the hydrophobized MgO@mSiO$_2$-OTS and MgO-OTS catalysts are lower, the activity remains high for 32 hours, reaching significant levels of conversion, eventually higher than that obtained on the non-functionalized catalyst.
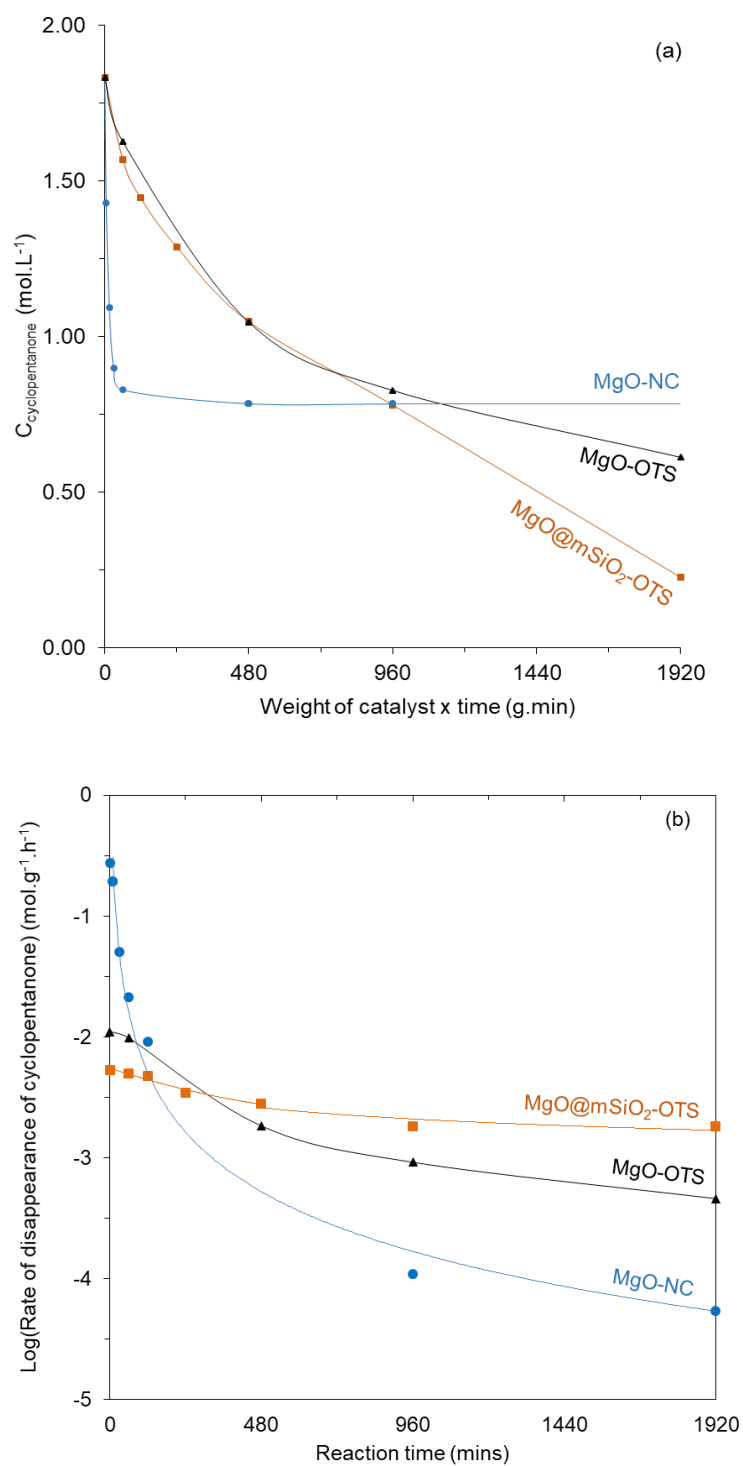
Figure 9. Comparison of (a) reactant concentration profiles, and (b) reaction rates on MgO-NC, MgO-OTS and MgO@mSiO₂-OTS catalysts at 150°C in the batch reactor.

Another important advantage of the functionalized $MgO@mSiO_2$-OTS catalyst is its tolerance to added water. **Figure 10** compares the effect of adding 2 mL of water to the 50-mL reaction mixture over the MgO-NC and $MgO@mSiO_2$-OTS catalysts. To make the comparison at similar conversions (16 - 18%) in the absence of water, the catalyst mass and reaction time were 0.25 g - 1 hour for the former and 0.50 g - 4 hours for the latter. As summarized in **Table 2**, the 2 mL of water added is significantly greater than the amount generated by the self-aldol condensation reaction. The difference in the response to water addition is remarkable. While the MgO-NC sample lost 80% of its activity, the OTS-functionalized sample kept most of its activity in the presence of excess added water. In addition, these two catalysts were recovered after the reaction including external water and analyzed for morphological variation. Although **Figure 11** displays peaks attributed to crystalline $Mg(OH)_2$ from both samples, the XRD pattern of spent $MgO@mSiO_2$-OTS only slightly differs from that of the fresh one. On the other hand, there is a clear phase transition from MgO to $Mg(OH)_2$ with intensively distinct diffraction peaks regarding spent MgO-NC. In other words, the as-described 80% loss of activity of MgO-NC could be ascribed to the irreversible formation of $Mg(OH)_2$ following the exposure of MgO to 2 mL of added water.
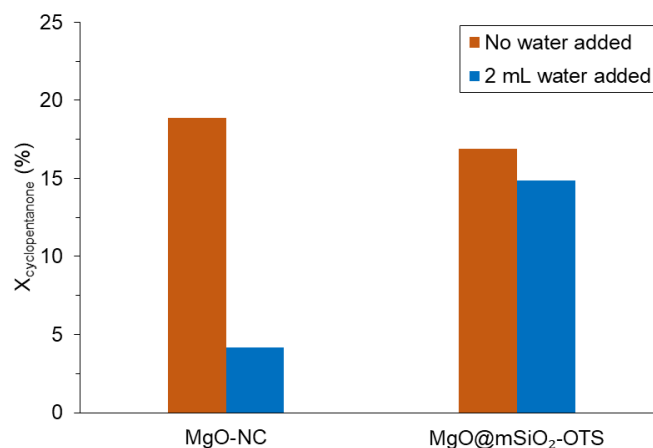
Figure 10. Effect of external water on the catalytic activity of MgO-NC and

MgO@mSiO$_2$-OTS.

Reaction conditions: $C_{cyclopentanone\ 0}$ = 1.8 M, 150°C, 450 psia in N$_2$, 0.25 g – 1 hour for

MgO-NC, 0.50 g – 4 hours for MgO@mSiO$_2$-OTS.
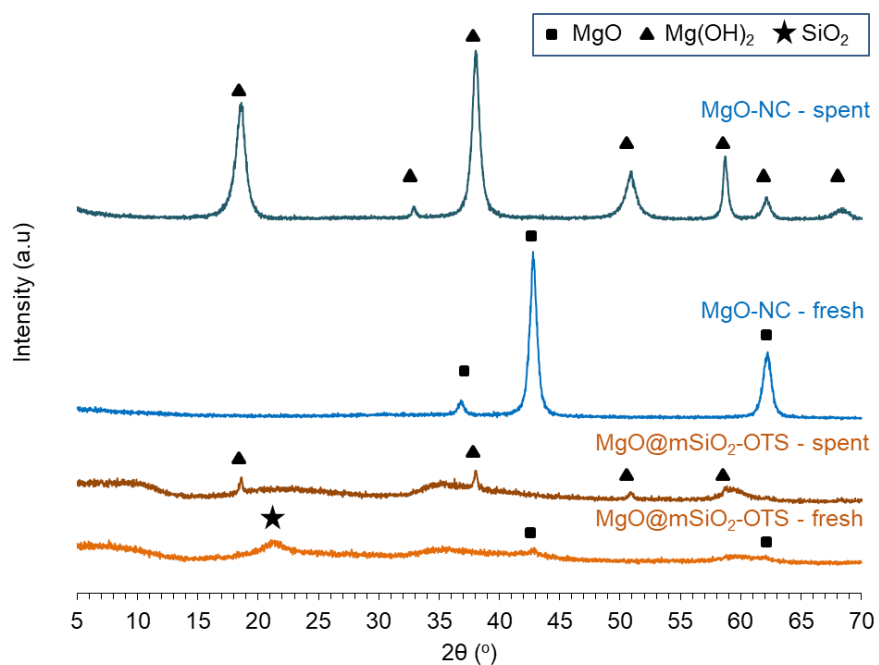
Figure 11. XRD patterns of spent MgO and spent MgO@mSiO$_2$-OTS after exposure to

2 mL of water at 150°C.

Table 2. Different amounts of water involved in cyclopentanone self-aldol condensation.

Reaction conditions: $C_{cyclopentanone\ 0}$ = 1.8 M, 150°C, 450 psia in N_2.

Catalyst	Weight	Time	$V_{H_2O\ added}$	$\Sigma C_{products}$	$V_{H_2O\ formed}$	ΣV_{H_2O}
	g	hr	mL	M	mL	mL
MgO-NC	0.25	1	0	0.16	0.15	0.15
	0.25	1	2	0.04	0.03	2.03
MgO@mSiO$_2$-OTS	0.50	4	0	0.15	0.14	0.14
	0.50	4	2	0.13	0.11	2.11
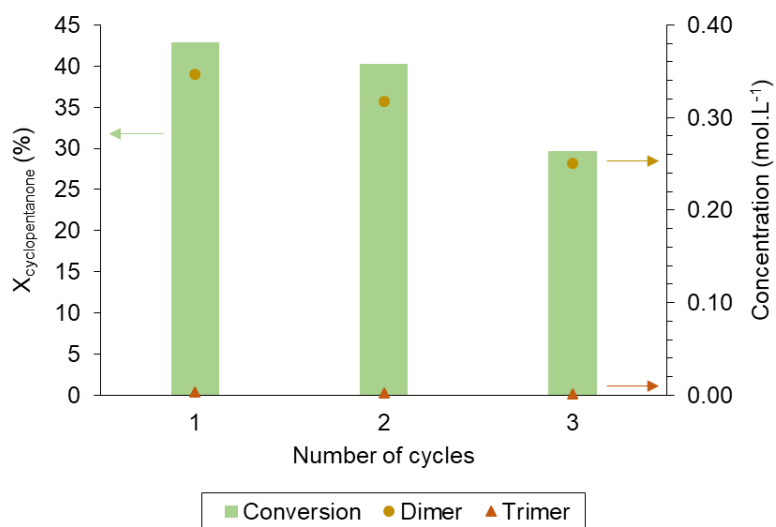
Figure 12. Conversion and product distribution from consecutive uses of the

MgO@mSiO$_2$-OTS sample.

Reaction conditions: 0.50 g of MgO@mSiO$_2$-OTS, $C_{cyclopentanone\ 0}$ = 1.8 M, 200°C, 600

psia in N_2, 2 hours.

The positive effect of hydrophobization is also observed on the reusability of the catalyst after a reaction cycle. **Figure 12** shows the evolution of activity and selectivity of MgO@mSiO$_2$-OTS during consecutive reaction cycles. Contrary to the relatively high reusability of the functionalized catalyst, the non-functionalized one (MgO-NC) loses all its activity after the initial cycle.

To rationalize the dramatic effect of the functionalization on catalyst stability, we have to analyze the differences observed in the surface characterization studies. The two obvious changes upon functionalization are the removal of the more basic sites in MgO and the conversion of a very hydrophilic surface into a hydrophobic one.

First, we can expect that the most active sites towards reaction with the Cl groups in the organosilane are the most basic sites. Therefore, eliminating the most basic sites should lower the initial activity, but prevent deactivation. In fact, it is seen that the sample with higher basicity (MgO-NC) exhibits higher initial activity but deactivates quickly. Also, as shown in **Figure 13**, a significant amount of trimer (2,5-dicyclopentylidenecyclopentanone) begins to appear at higher conversions. It is conceivable that trimer and other larger oligomers can lead to accumulation of heavy carbonaceous compounds and catalyst deactivation. One of the additional effects of OTS functionalization is the inhibition of the formation of trimer. In fact, as shown in **Figure 13**, the increase in the C_{trimer}/C_{dimer} ratio as a function of overall conversion is much greater on the non-functionalized MgO-NC than on any of the OTS-functionalized catalysts. The presence of silica does not seem to have a very significant difference, indicating that the silane functionalization is responsible for this change in selectivity.
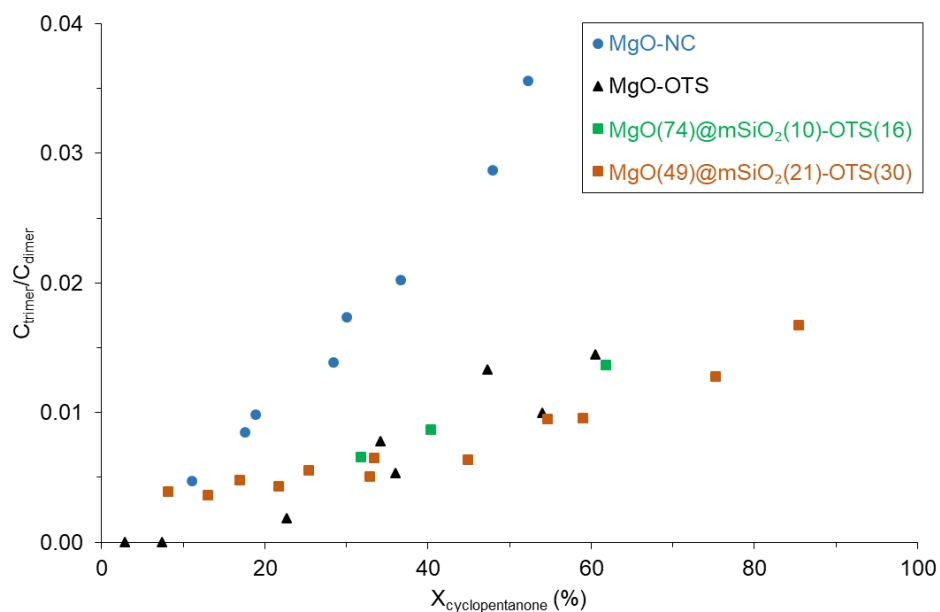
Figure 13. The ratio of molar concentrations of the trimer and the dimer obtained from

the MgO-catalyzed cyclopentanone self-aldol condensation with respect to conversion.

Reaction conditions: $C_{\text{cyclopentanone } 0} = 1.8$ M, 150°C, 450 psia in N_2.
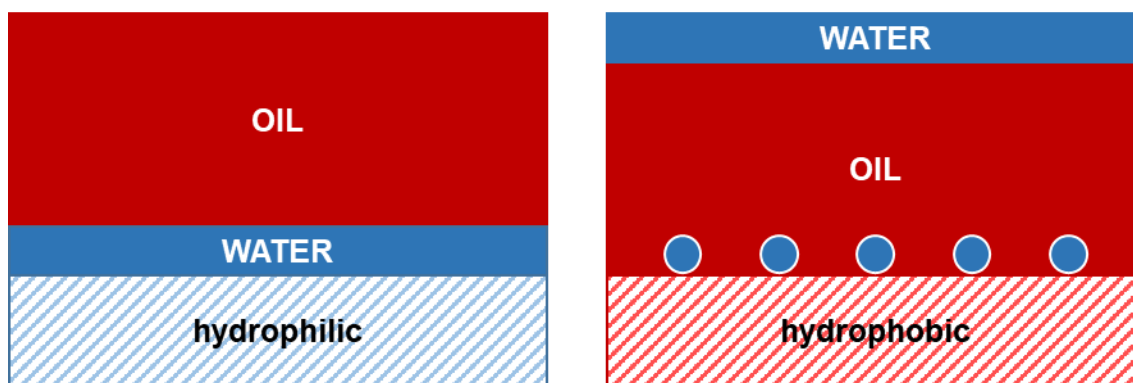
Figure 14. Schematic behaviors of hydrophilic and hydrophobic MgO catalysts

following exposure to *in situ* water.

Second, functionalization with a hydrophobic moiety has the obvious advantage of reducing the nucleation of water on the surface and formation of a liquid film that could block sites, cause mass transfer limitations, and even attack the MgO surface forming inactive $Mg(OH)_2$ [55,56]. One must notice that the aldol condensation reaction generates a water molecule for every α,β-unsaturated ketone. Since the solvent is non-polar cyclohexane, upon formation, water would tend to remain on the hydrophilic MgO surface, which would act as nucleation sites for the formation of a liquid film (**Figure 14**). Conversely, the hydrophobic surface of $MgO@mSiO_2$-OTS would not nucleate the formation of a liquid film, allowing water to phase-separate from the non-polar solvent, in line with the minimal effect on activity observed when large amounts of water were added to this catalyst, as shown in **Figure 10**.

1.4. Summary

The main conclusions of the study are the following:

i. While MgO is an active catalyst for cyclopentanone self-aldol condensation, it exhibits a low catalyst stability in the liquid phase, particularly in the presence of liquid water.

ii. Functionalization with organosilanes increases the hydrophobicity of the surface, which has important effects on activity, selectivity, and stability. Specifically:

- The catalytic activity is maintained for a much longer time than that of the non-functionalized material.

- The resistance to water attack is greatly enhanced.

- The initial rate is significantly reduced, most probably due to the selective titration of the most basic sites on the parent oxide.

iii. Hydrophobization is more effective than other methods previously investigated for preventing deactivation of basic catalysts during aldol condensation. For example, while the addition of a hydrogenation catalyst is an effective method for other systems in the gas phase, such a method is less effective for cyclopentanone on MgO in the liquid phase. That is, at elevated H_2 pressures, ketone feed saturation reduces the overall rate of condensation. At low H_2 pressures, catalyst deactivation is significant.

2. Cross-aldol condensation of cyclopentanone and acetone on MgO. Mechanistic aspects that determine product distribution.

2.1. Introduction

Thermal pyrolysis is an effective form of converting biomass via thermal decomposition at high temperatures followed by condensation, which results in high liquid yields [10]. However, the resulting pyrolysis liquid is of limited utility since it is unstable, corrosive, and challenging to upgrade catalytically. Moreover, this liquid contains a wide range of components with different chemical functionalities, including a large fraction of light ($<C_6$) oxygenates, which are unsuitable for liquid fuels due to their low carbon chain length. Therefore, elimination of oxygen is not the only catalytic upgrading necessary to obtain useful biofuel components, but C-C coupling reactions are also indispensable.

Multistage torrefaction combined with catalytic upgrading of the individual stage products is a promising method for overcoming these challenges [1]. The fractional decomposition of biomass in sequential stages limits the number of species within each fraction, which allows designing the catalytic upgrading after each stage for the specific chemistries of the subset of functionalities present in the given range of compounds [2].

Two of the most abundant products obtained in relatively high concentrations from the individual thermal stages are acetic acid and furfural. The former can be readily converted to acetone via ketonization [21], while the latter can be converted to cyclopentanone via hydrogenation/Piancatelli ring rearrangement [15-18]. Both of these reactions are well established and can be carried out with high efficiency on different

catalysts in terms of yield, selectivity, and catalyst life. Therefore, it is techno-economically conceivable that these intermediate ketones could be obtained from biomass in industrial scale and with reasonable purities.

An effective reaction to obtain fuel-range components from these ketones is aldol condensation, a well-known reaction catalyzed by bases and acids. The self-aldol condensation of acetone has been studied for many years. The products from this reaction are mesityl oxide, mesitylene, phorone and isophorone. Several studies have shown that mesityl oxide is favored in the presence of either an acid catalyst (e.g. anhydrous HCl, concentrated H_2SO_4) or a base catalyst (e.g. ZrO_2, MgO-V_2O_5) [23,24,57,58]. It has been reported that acid-catalyzed condensation tends to form more mesitylene and heavier compounds than the base-catalyzed counterpart [59-61]. While the behaviors and trends displayed by different catalysts have been well documented, the exact mechanism of this well-known reaction is still a matter of investigation. For example, depending on the conditions and specific catalyst used, either the initial deprotonation (α-C-H activation) or the C-C coupling step has been proposed to be rate-limiting [49]. Specifically, the former seems to be kinetically relevant when the catalyst is anatase TiO_2, which exhibits Lewis acid-base pairs of moderate strength. By contrast, the latter governs the overall rate when the reaction is catalyzed by acid zeolites [62].

The self-aldol condensation of cyclopentanone has been much less investigated than that of acetone. However, the potential use of this compound as a building block in biofuel production, as described above, enhances the significance of this C-C bond-forming reaction. Among the few studies involving cyclopentanone, the one by Yang *et al.* [25] is

particularly relevant. They showed that under solvent-free conditions at 150℃, significant yields of 2-cyclopentylidenecyclopentanone were obtained over solid bases, such as hydrotalcites, CaO, and MgO, and pointed out that fuel-range C_{10} - C_{15} hydrocarbons could be obtained after hydrodeoxygenation. Similarly, Liang *et al.* [26] showed that mesoporous MgO-ZrO$_2$ catalysts produced 100% selectivity to the dimer product up to 80% conversion at 130°C and atmospheric pressure. Despite the practical importance of these results, little knowledge has been obtained on the mechanism for this reaction.

In the current study, we have attempted to expand the mechanistic understanding of the competing self- and cross-aldol condensations of cyclopentanone and acetone. These are two potentially abundant intermediate products derived from biomass, which may have importance in practical applications. Since both carbonyls contain an α-H, the self- and cross-aldol condensations can lead to at least four products, with each of the reactants acting either as an enolate or an electrophile.

Both acetone (A) and cyclopentanone (C) can be activated by α-H abstraction to form the enolates [A] and [C], respectively, which in turn can attack either an A or a C, acting as electrophiles. Thus, as illustrated in **Figure 15**, the dimer products include [A]A, [A]C, [C]A, and [C]C. The possible trimers are also included in this schematic figure, but they only appear in small amounts, particularly at a certain level of conversion. One can expect that the product distribution might depend on the relative acidity of the α-H in each carbonyl as well as their relative initial concentrations [50,63,64]. In other words, if α-H abstraction from cyclopentanone is much easier than that from acetone, the two products from the initial activation of cyclopentanone, that is, 2-cyclopentylidenecyclopentanone

[C]C and 2-isopropylidenecyclopentanone [C]A will dominate, as observed in previous works [65-67]. From the practical point of view, the cross-aldol condensation of cyclopentanone and acetone may be a promising route to upgrade biofuels since condensation products could be further refined by hydrodeoxygenation to generate highly branched hydrocarbons in the fuel range (C_8-C_{15}) [28,68], which would either enhance gasoline octane numbers or improve diesel cloud points.
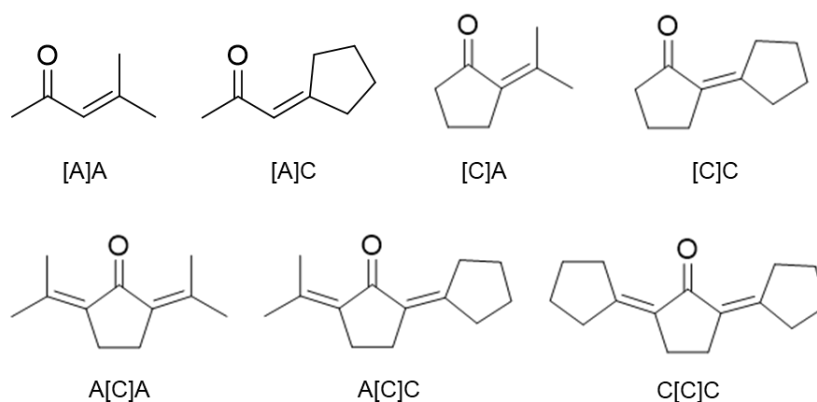
Figure 15. Dimer and trimer products from the self and cross-aldol condensations of acetone (A) and cyclopentanone (C).

Along the same lines, a study of the cross-aldol condensation of cyclopentanone and pentanal at 130°C and a 5:1 molar ratio [34] showed that the activation of cyclopentanone was much more effective, as indicated by the high combined yields of 2-pentylidenecyclopentanone and 2-cyclopentylidenecyclopentanone, which in all cases approximated 90% of the total products. Interestingly, in another study [69], it was

observed that the relative yield of each of the two possible products arising from the initial activation of cyclopentanone depended on the catalyst used. That is, while crystalline MgO preferentially favored the cross-aldol condensation product, a zirconophosphate catalyst (ZrPO) rendered a more even split of the two products. Therefore, there is a potential to tailor the reaction conditions and catalyst to control the product distribution.

2.2. Experimental

2.2.1. Synthesis of catalytic materials

MgO-NC. The catalyst solely used in this study, MgO-NC, was synthesized via nitrate-citrate combustion, a method described elsewhere [70]. Briefly, 0.1 mol of $Mg(NO_3)_2.6H_2O$ (Aldrich, 99.9 %) was dissolved in 30 mL of water and stirred vigorously for 15 mins at 80^oC. Then, a 20-mL water solution containing 0.1 mol of citric acid (Aldrich, 99.5 %) was added to the $Mg(NO_3)_2$ water solution. The whole mixture was continuously stirred until half of the liquid vaporized, leaving a viscous gel being subject to an overnight calcination under static air at 550^oC. This calcination involved the combustion of citric acid to generate a high-surface-area MgO material [41,42]. The obtained MgO is denoted as MgO-NC, where NC stands for nitrate-citrate combustion.

2.2.2. Adsorption measurements

To compare the relative extents of adsorption of cyclopentanone and acetone from the liquid phase, a set of adsorption measurements were conducted. For these measurements, dual feeds with equimolar ratios of acetone/cyclopentanone were prepared

at individual concentrations of 0.5 M, 1.0 M and 2.0 M. In each run, a 100-mL vessel (Parr) was first filled with cyclohexane and 2 g of MgO-NC, then pressurized to 400 psia of N_2 at room temperature. Next, a liquid mixture containing acetone, cyclopentanone and toluene (internal standard) was pressurized to 500 psia of N_2 in a 30-mL feeding cylinder and injected into the 100-mL vessel. The total liquid volume in the vessel was 40 mL for all runs. After the reactants entered the vessel, the suspension was stirred at 750 rpm for 1 hour to achieve adsorption equilibrium, then the filtered liquid was analyzed via GC-FID. The uptake of each ketone Γ (moles per gram of MgO-NC) is given by the following expression:

$$\Gamma = \frac{(C_0 - C_{eq}) \times \Sigma V}{w_{MgO\text{-}NC}}$$

where

C_0 = initial molar concentration [mol.L^{-1}]

C_{eq} = equilibrium molar concentration [mol.L^{-1}]

2.2.3. Catalytic measurements

2.2.3.1. Reactor operating conditions and analysis methods

In each run, MgO-NC and cyclohexane were first added into a 100-mL vessel (Parr). The system was purged and pressurized to 300 psia in N_2, then heated to the reaction temperature. Next, the individual or dual reactant feed (acetone/cyclopentanone), along with toluene (internal standard), were placed in a 30-mL feeding cylinder and pressurized to 450 - 500 psia in N_2. This liquid mixture was injected into the vessel when the desired

temperature was stabilized. Reaction runs were carried out under a stirring speed of 750 rpm. After reaction, the suspension was centrifuged for 5 mins at 4000 rpm to minimize the vaporization of acetone. All liquids were analyzed by GC-MS and GC-FID as previously described [47].

2.2.3.2. *Quantification of active sites under reaction conditions*

The active Mg-O sites were quantified via isothermal titration with propanoic acid, following Wang *et al.* [48], who demonstrated that propanoic acid could strongly block acid–base site pairs on TiO_2 during acetone self-aldol condensation and allow a quantitative estimation of the total number of these sites. In these measurements, we obtained initial rates for cyclopentanone self-aldol condensation at 150°C, with varying amounts of propanoic acid in the feed. The amount of acid irreversibly adsorbed by MgO was calculated from the difference between the concentrations in the feed and after exposure to the catalyst. The measured rate decreased proportionally to the amount of titrant propanoic acid adsorbed. Extrapolation to zero rate would provide an estimate of the density of acid–base site pairs responsible for the condensation activity. This density per unit mass of catalyst is given by the expression:

$$\frac{V_{propanoic\ acid\ adsorbed} \times \rho_{propanoic\ acid}^{150^oC}}{MW_{propanoic\ acid} \times w_{catalyst}}$$

2.2.4. *Density Functional Theory calculations*[*]

The calculations were carried out using periodic plane-wave gradient-corrected density functional theory methods implemented in VASP. The PBE functional was used to calculate the exchange correlation energy within the generalized gradient approximation (GGA). The projector augmented wave method (PAW) was employed to describe the electron-ion interactions. The cutoff energy of 400 eV was applied for the plane-wave basis set to represent valence electrons. The DFT-D3 method was used for the correction of van der Waals interactions (vdW). The electronic energies were converged within 10^{-6} eV limit, and the force on each atom was converged to below 10^{-2} eV.Å^{-1}.

The close-packed 3×3 MgO(100) slab surface with four layers and 15 Å vacuum in the z-direction was used to model the MgO catalyst. The bottom two layers were fixed at their bulk position while the top two layers were allowed to relax in all optimizations. The $4 \times 4 \times 1$ Monkhorst-pack k-point mesh was used to sample the first Brillouin zone. The gas phase calculations were carried out spin-polarized using an 18 Å $\times$ 18 Å $\times$ 18 Å unit cell with the Γ only k-point mesh.

The deprotonation energy (DPE) for the α-H of acetone/cyclopentanone was calculated to describe the acidity of each ketone via equation (*), where E_{AH}, E_{A^-} and E_{H^+} were the total energies of the neutral ketone AH, the negatively charged species A$^-$ after deprotonation, and the proton H$^+$.

$$AH \rightarrow A^- + H^+$$

---
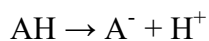
[*] DFT calculations were conducted by Dr. Qiaohua Tan.

$$DPE_{AH} = E_{A^-} + E_{H^+} - E_{AH} \quad (*)$$

For reaction paths, the transition state searches were performed using the dimer method with the initial guesses for the transition state structure and the reaction trajectory obtained through the nudged elastic band method (NEB).

2.3. Results

2.3.1. Adsorption measurements
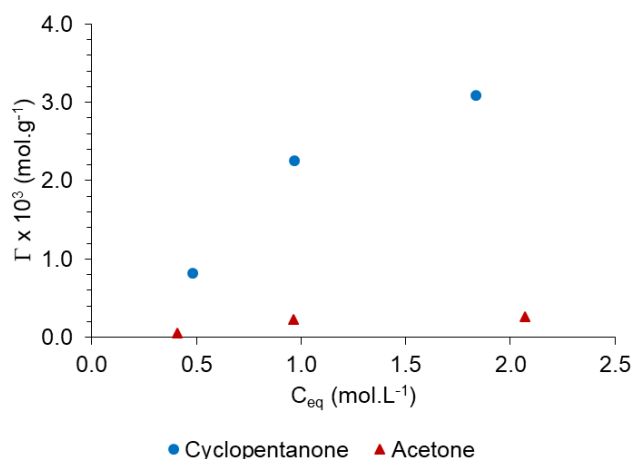
Figure 16. Adsorption measurements of cyclopentanone and acetone on MgO-NC. Conditions: 2.00 g of MgO-NC, $C_{cyclopentanone\ 0} = C_{acetone\ 0}$, 25°C, 450 psia in N_2, 60 mins.

Figure 16 displays the uptakes of cyclopentanone and acetone on the MgO-NC sample as a function of equilibrium molar concentration. It is observed that the adsorbed amount of cyclopentanone at room temperature is, at least, 10 – 15 times greater than that of acetone. That is, one should expect that under reaction conditions the surface coverage of cyclopentanone should be significantly higher than that of acetone; and if the C-C

coupling step in the aldol condensation reaction followed a Langmuir-Hinshelwood model, one would anticipate that the rates of formation of [C]C and [A]C would be respectively much greater than those of [C]A and [A]A. We will discuss why this is not the case in the following sections.

2.3.2. Catalytic measurements

2.3.2.1. Quantification of active sites under reaction conditions
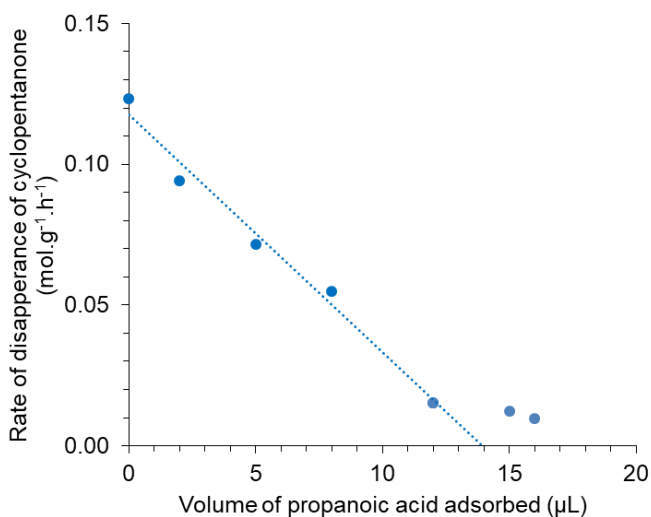
Figure 17. Propanoic acid-controlled cyclopentanone self-aldol condensation initial rates on MgO-NC.

Reaction conditions: 0.50 g of MgO-NC, $C_{cyclopentanone\ 0}$ = 1.8 M, 150°C, 450 psia in N_2, 30 mins.

Since no peaks of propanoic acid were detected from GC-FID profiles, it could be stated that MgO-NC irreversibly adsorbed all introduced amounts of propanoic acid.

According to **Figure 17**, it is only up to 12 µL of propanoic acid that the rate decreases proportionally to the acid uptake. In this range, zero-extrapolation to the x-axis yields 14 µL. When more acid is added, the rate experiences a much less pronounced decline. Such response could be ascribed to the co-existence of acid-base site pairs with different basic strengths, which was confirmed via CO_2-TPD by Pham *et al.* [46]. That is, the first data points reflect the strongest basic sites of MgO-NC. Beyond 14 µL, these sites have been fully titrated, leaving the remaining sites of lower basicity to catalyze cyclopentanone self-aldol condensation. However, as Pham's CO_2-TPD data indicated the dominance of the strongest sites, 14 µL is considered the maximum acid uptake in this study. As a result, the calculated number of active acid-base site pairs is 375 $\mu mol.g^{-1}$.

2.3.2.2. Comparison of specific rates and TOF

Table 3. The inhibition effect of cyclopentanone upon the deprotonation of acetone.

Reaction conditions: 0.20 g of MgO-NC, $C_{cyclopentanone\ 0} = C_{acetone\ 0} = 1.0$ M, 200°C, 450 psia in N_2, 20 mins.

Feed		Rate of formation				TOF			
		$mmol.gcat^{-1}.h^{-1}$				h^{-1}			
		[C]A	[C]C	[A]A	[A]C	[C]A	[C]C	[A]A	[A]C
Single	A + A	-	-	34.92	-	-	-	93.12	-
	C + C	-	84.29	-	-	-	224.77	-	-
Dual	C + A	33.61	46.59	2.06	3.07	89.63	124.24	5.50	8.20

As pK_a values of cyclopentanone and acetone at standard conditions are 18.4 [71] and 19.2 [72] respectively, the deprotonation of the former would be more favorable than that of the latter. This aspect was confirmed through MgO-NC-catalyzed 20-min runs at 200°C where only one ketone was in the feed with an initial molar concentration of 1.0 M. **Table 3** shows that the rate of formation of [C]C (or TOF by assuming an intrinsic basicity of 375 μmol.g^{-1}) is approximately 2.5 times greater than that of [A]A. Such results suggest the dominance of [C]-activated products from an equimolar dual feed, which is in fact verified as the combined selectivity of [A]A and [A]C is only 7%. Moreover, the competitive adsorption of cyclopentanone from the bulk liquid of cyclohexane might have also prevented acetone from its own α-H abstraction. This is because the TOF of [A]-activated products decreases by 7 times with respect to that of [A]A from the self-aldol condensation. By contrast, acetone hardly affects the TOF of [C]-activated products. Clearly, not only the strong chemisorption of cyclopentanone on MgO-NC but its higher acidity and inhibiting interaction to acetone also impact on the product distribution of the cross-aldol condensation.

a. Effect of temperature
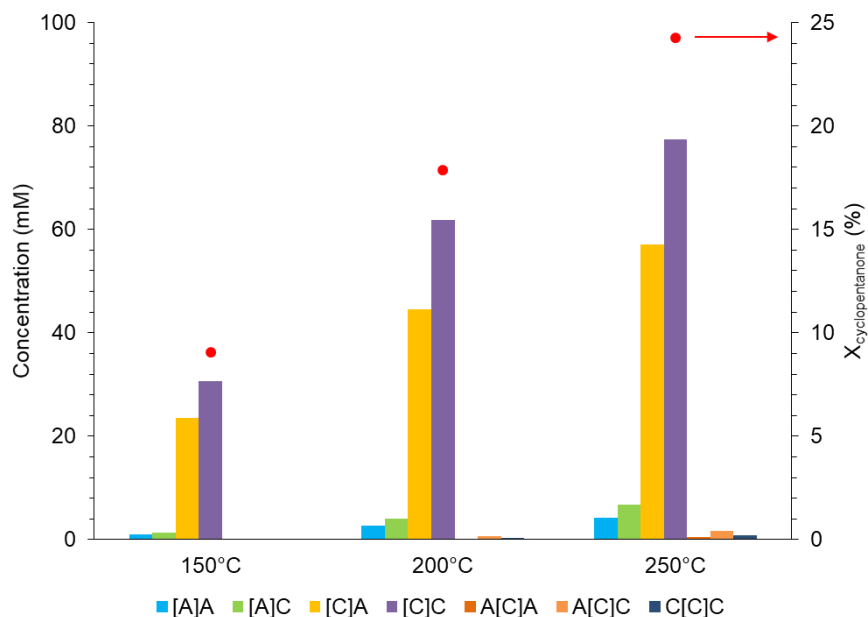
Figure 18. Temperature-based product distribution of cyclopentanone-acetone cross-aldol condensation.

<u>Reaction conditions:</u> 0.20 g of MgO-NC, $C_{cyclopentanone\ 0} = C_{acetone\ 0} = 1.0$ M, 450 psia in N_2, 20 mins.

Figure 18 shows the catalytic performance of MgO-NC at 150ºC, 200ºC and 250ºC. The most noticeable impact of rising the temperature is increased TOFs for all four dimer products. This increase indicates that beyond 200ºC, acetone has a higher chance to form an enolate for [A]A and [A]C, but the α-H abstraction of cyclopentanone is consistently preferable. From the perspective of product distribution, all three reaction temperatures result in more than 90% of [C]-activated products. In particular, selectivities

to [C]C and [C]A hardly vary despite considerable temperature intervals. Interestingly, the amount of cyclopentanone attacked by cyclopentenolate is only 1.4 times of that of acetone, although C has been shown drastically outnumbering A on the MgO-NC surface. Such aspect will be addressed in details following the increase of the acetone-to-cyclopentanone feed ratio. Despite the majority of [C]C and [C]A, 250°C will not be further studied as this temperature associates with indispensable amounts of A[C]A, A[C]C and C[C]C. To optimize catalytic activity and selectivities to dimer products, all remaining experiments in this study were conducted at 200°C.

b. Evolution of products

[C]C and [C]A have been shown contributing more than 90% of liquid products after the first 20 mins of MgO-NC-catalyzed cross-aldol condensation. This section addresses how the catalytic activity of MgO-NC and selectivities to [C]-activated products change along the reaction time.

Since MgO-NC is prone to deactivation by oligomers and *in situ* water [70], we only evaluated the product distribution of equimolar cross-aldol condensation up to 2 hours (**Figure 19**). First, within this time range, the conversion of cyclopentanone increases rapidly from 18% (20 mins) to 37% (1 hour) and finally 60% (2 hours). Second, [C]A and [C]C remain predominant, with the [C]A-to-[C]C ratio experiencing a moderate but noticeably increase from 0.7 to nearly 0.8. To some extent, such aspect means one can attain a [C]A-to-[C]C ratio being close to 1 at longer times. That is, the [C]A-to-[C]C ratio may continue increasing after most cyclopentanone electrophiles have undergone C-C

43

coupling, leaving more acetone electrophiles for the nucleophilic attack of cyclopentenolate. However, this projection is not the case over MgO-NC, as concentrations of [C]-activated trimers become sizeable at high conversions of cyclopentanone (**Appendix D**). In other words, acetone electrophiles are not only limited to interaction with cyclopentenolate but can also be subject to nucleophilic attacks of dimeric enolates. Moreover, at 2 hours, the decreased combined selectivity to [C]C and [C]A suggests that [C]-activated trimers start accumulating on active site pairs of MgO-NC and contribute to catalyst deactivation. To sum up, both **Figure 18** and **Figure 19** indicate that MgO-NC – as an initially active catalyst – consistently favors cyclopentanone self-aldol condensation from an equimolar feed of cyclopentanone-acetone.
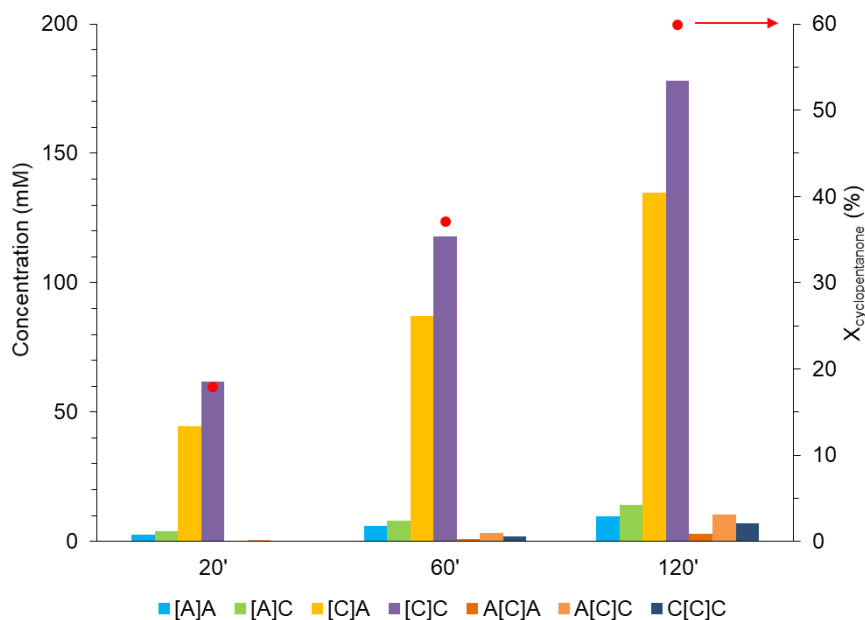
Figure 19. Evolution of cyclopentanone-acetone cross-aldol condensation products.

Reaction conditions: 0.20 g of MgO-NC, $C_{\text{cyclopentanone 0}} = C_{\text{acetone 0}} = 1.0$ M, 200°C, 450 psia in N_2.

44

c.   Effect of acetone-to-cyclopentanone feed ratio

Temperature tests have indicated that the MgO-NC-catalyzed cross-aldol condensation of an equimolar dual feed generates exclusive amounts of [C]C and [C]A. Here, we investigate whether excess acetone dramatically increases the amounts of [A]A and [A]C or simply boosts selectivities to -A condensates.
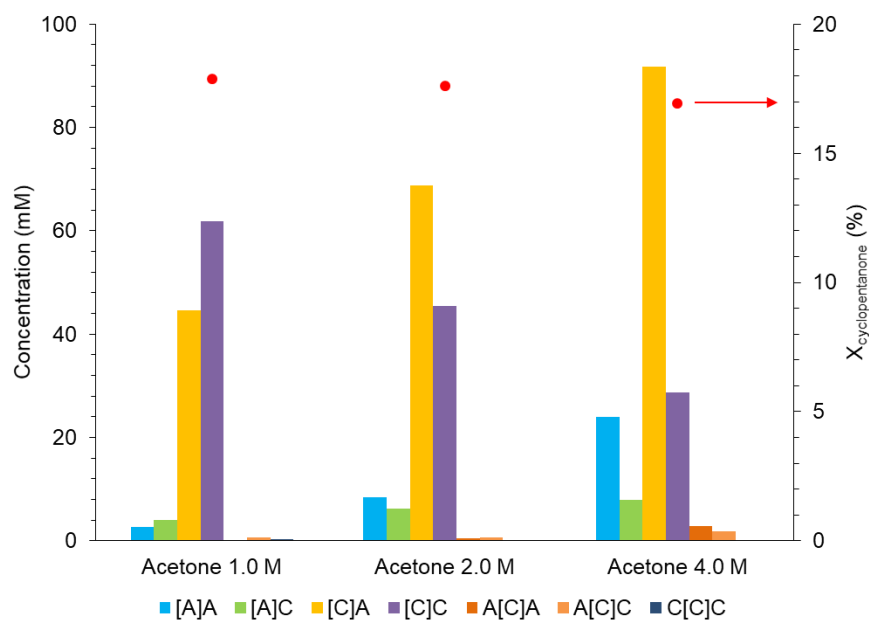
Figure 20. Acetone-to-cyclopentanone feed ratio-based product distribution of cyclopentanone-acetone cross-aldol condensation.

<u>Reaction conditions:</u> 0.20 g of MgO-NC, $C_{\text{cyclopentanone } 0} = 1.0$ M, 200°C, 450 psia in N_2, 20 mins.

In practice, the initial molar concentration of cyclopentanone was maintained at 1.0 M while that of acetone was increased to 2.0 M and 4.0 M. Other reaction conditions

were similar to those applied for the equimolar cross-aldol condensation. A remarkable shift between selectivities to [C]A and [C]C is observed in **Figure 20**. The decreased amount of the latter is almost equal to the concurrent increased amount of the former. In numbers, the [C]A-to-[C]C molar ratio grows proportionally from 0.7 to 1.5 and 3.0, approximating 75% of the initial A-to-C ratio in cyclohexane. Such trend also applies for the [A]A-to-[A]C ratio.

Additionally, it is noteworthy that the nucleophilic attack of propen-2-olate in this study only forms [A]A and [A]C. Neither phorone A[A]A nor mesitylene is detected despite a considerably increased acetone population provided from either the MgO-NC surface (Langmuir-Hinshelwood model) or the bulk cyclohexane (Eley-Rideal model). On the other hand, newly-formed [C]C and [C]A can adapt monomer species of their proximity to generate trimer products A[C]A, A[C]C and C[C]C. However, these trimer products are only detected in trace quantities.

Finally, although more acetone is added to the system, the TOF of [C]-activated products remains considerably greater than that of [A]-activated ones. In other words, the preferential deprotonation of cyclopentanone with respect to acetone continues, being similar to which has been observed under temperature tests. As a result, increasing the A-to-C feed ratio up to 4:1 only renders [C]A and [A]A more abundant since these species are condensates in which acetone is the electrophile.

2.3.3. *Density Functional Theory calculations*[*]

1.22 Å   1.23 Å

2.24 Å   2.25 Å

ΔE_{ads} = -62 kJ.mol^{-1} ΔE_{ads} = -55 kJ.mol^{-1}

● Mg   ● O   ● C   ○ H
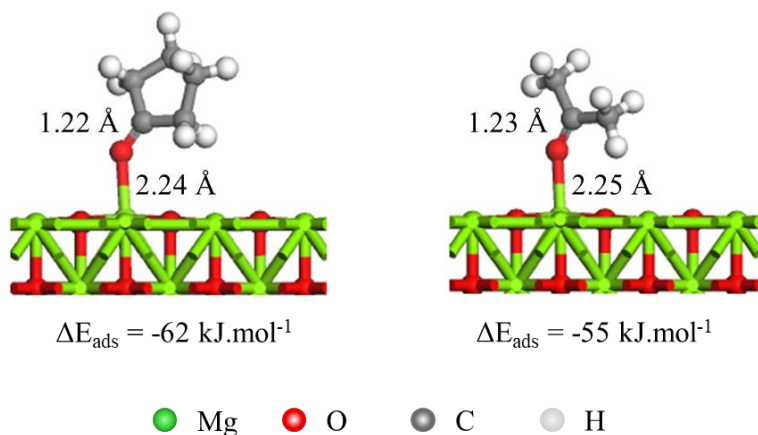
Figure 21. DFT-optimized adsorption structure of cyclopentanone (left) and acetone (right) on MgO(100).

As shown in **Table 3**, [C]A and [C]C are dominant with respect to [A]A and [A]C when co-feeding cyclopentanone and acetone over MgO-NC at 200°C for 20 mins. This suggests the activation of an α-H of cyclopentanone is more favorable than that of acetone. As α-H abstraction occurs at the same basic site of MgO, the reactivity of an α-H depends on the acidity of the corresponding ketone. Deprotonation energies of α-Hs of cyclopentanone and acetone in gas phase were calculated to be 1453 kJ.mol^{-1} and 1461 kJ.mol^{-1} respectively. The lower deprotonation energy of cyclopentanone indicates the stronger acidity and a more reactive α-H. Such calculation is also consistent with the reported pK_a values of cyclopentanone (18.4) [71] and acetone (19.2) [72] at standard conditions.

---

[*] DFT calculations were conducted by Dr. Qiaohua Tan.

For further confirmation, the deprotonation of cyclopentanone and acetone, followed by C-C coupling with a cyclopentanone electrophile were calculated over MgO(100). First, both ketones were adsorbed on MgO(100) at the Mg^{2+} site through a carbonyl O (**Figure 21**). Calculated adsorption energies of cyclopentanone and acetone were -62 $kJ.mol^{-1}$ and -55 $kJ.mol^{-1}$ respectively. The slightly stronger adsorption of cyclopentanone is probably due to its larger molecule, which results in stronger van der Waals interactions. This calculation suggests that cyclopentanone outperforms acetone in the competitive adsorption on MgO(100) and dominates the catalytic surface. After adsorption, Mg^{2+}-bound molecules of cyclopentanone and acetone proceeded with deprotonation to form cyclopentenolate and propen-2-olate respectively. As shown in **Figure 22,** on MgO(100), the calculated energy barrier of deprotonation of cyclopentanone was 60 $kJ.mol^{-1}$, being 9 $kJ.mol^{-1}$ lower than that of deprotonation of acetone. The energy diagram is consistent with aforementioned trends of deprotonation energy and pK_a value.
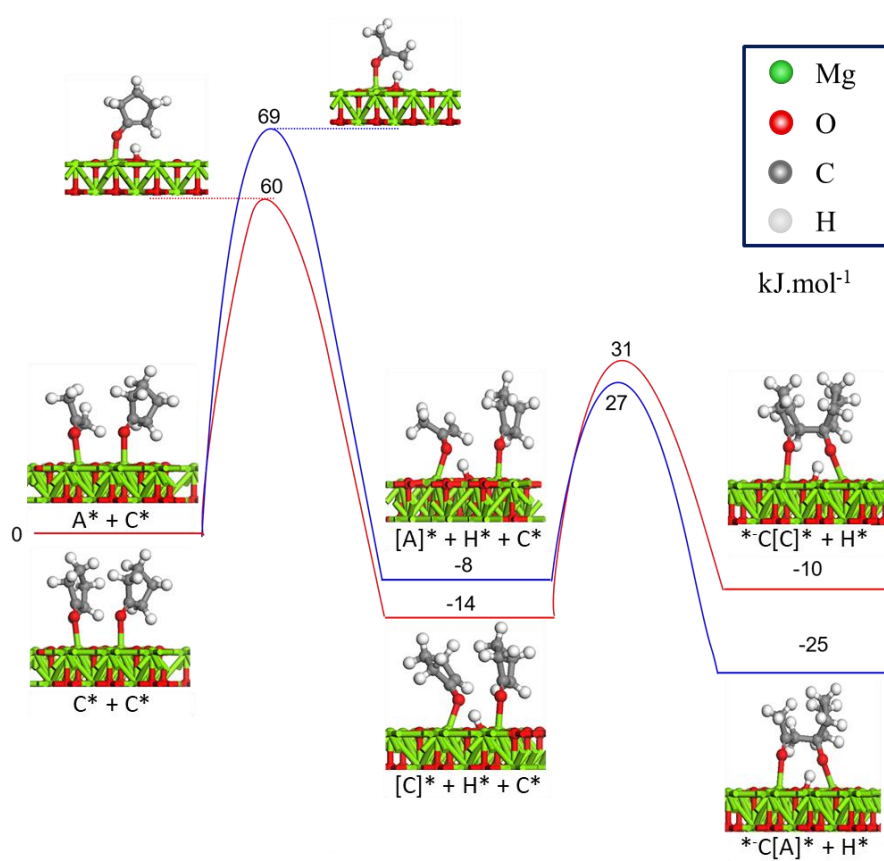
Figure 22. Energy diagram of α-H abstractions of cyclopentanone and acetone, and C-C couplings of cyclopentenolate-cyclopentanone (red) and propen-2-olate-cyclopentanone (blue) on MgO(100).

After deprotonation, each enolate could then target an adjacent electrophile (acetone/cyclopentanone) for C-C coupling, eventually forming the corresponding dimer product. As shown in **Figure 22**, the energy barrier of C-C coupling between cyclopentenolate and cyclopentanone electrophile was 45 kJ.mol^{-1}, considerably lower than that of deprotonation of cyclopentanone (60 kJ.mol^{-1}). This comparison suggests that deprotonation is the rate-limiting step. Similarly, the energy barrier of C-C coupling

between propen-2-olate and cyclopentanone electrophile was 35 $kJ.mol^{-1}$, considerably lower than that of deprotonation of acetone (69 $kJ.mol^{-1}$).

In conclusion, both the stronger adsorption and the lower deprotonation energy of cyclopentanone with respect to those of acetone contribute to the preference of [C]-activated products on MgO-NC. For each ketone, deprotonation is kinetically relevant since this elementary step requires the highest energy barrier.

2.4. Discussion

2.4.1. Possible mechanisms. Rate-limiting step

According to the literature, the mechanism of a heterogeneous base-catalyzed aldol condensation starts with the abstraction of a proton from the α-C with respect to the carbonyl moiety [73]. The resulting enolate – an anionic surface intermediate – subsequently attacks an adjacent carbonyl molecule supplied from either the catalytic surface (Langmuir-Hinshelwood model) or the continuous phase (Eley-Rideal model) (**Figure 23**). This C-C coupling shifts the electron density to the oxygen of the carbonyl molecule, therefore it readily claims the initially abstracted proton to generate a dimeric aldol. Reviewing such mechanism can help rationalize both the rate-limiting step and the product distribution of cyclopentanone-acetone cross-aldol condensation.
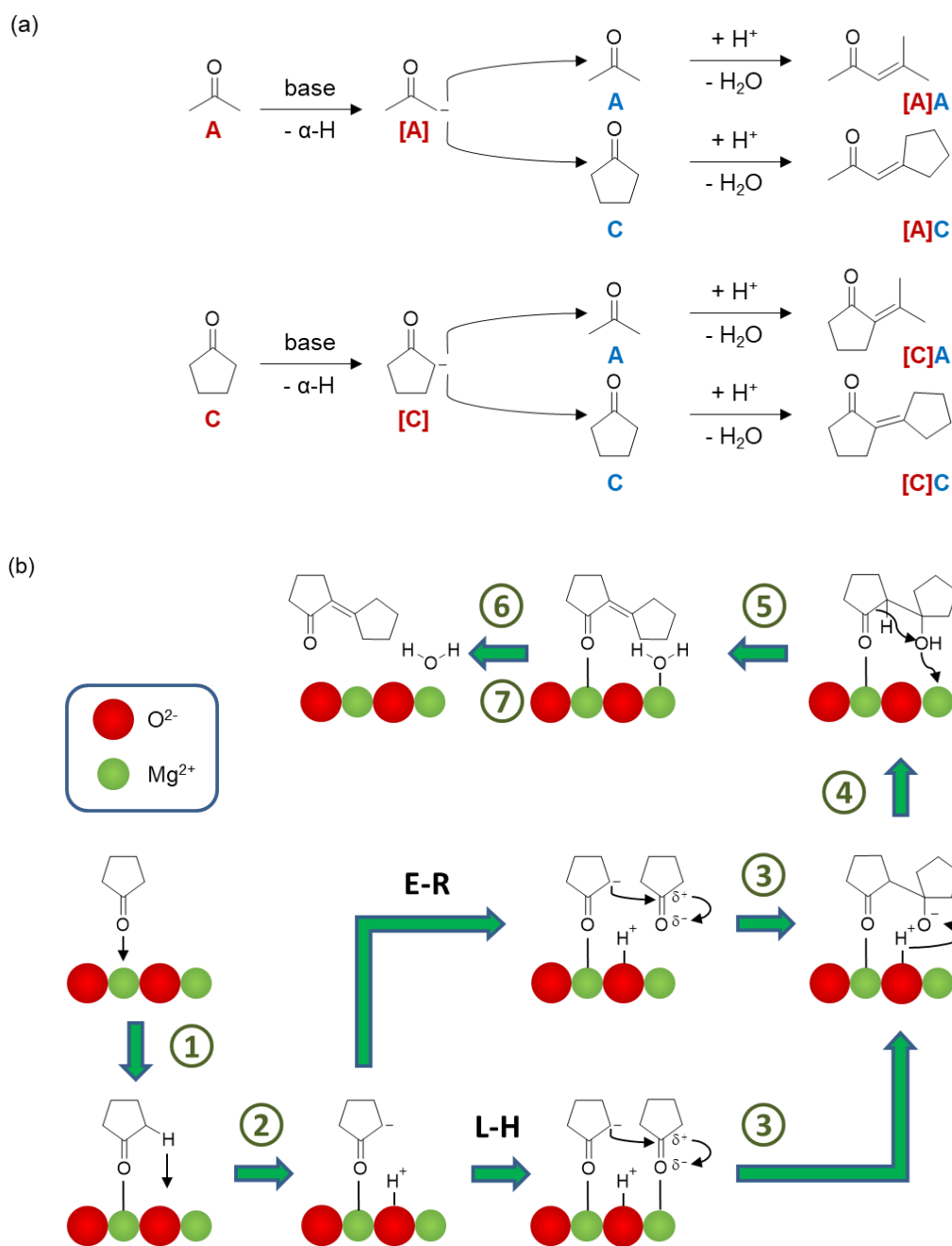
Figure 23. Mechanisms for a base-catalyzed aldol condensation. (a) homogeneous base.

(b) heterogeneous base (e.g. MgO).

51
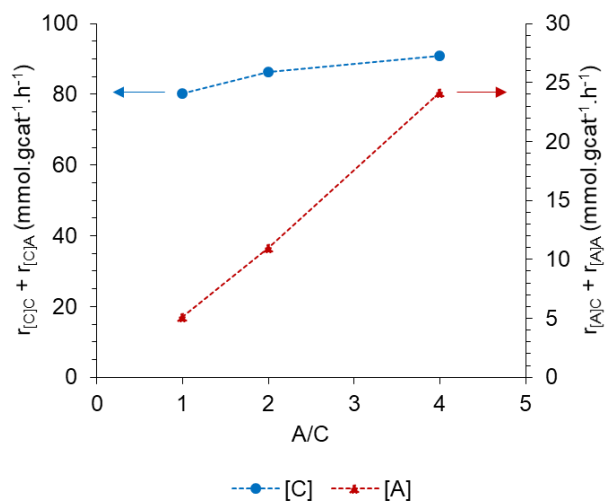
Figure 24. Variation of individual rates with the acetone-to-cyclopentanone feed ratio. <u>Reaction conditions:</u> 0.20 g of MgO-NC, $C_{\text{cyclopentanone 0}}$ = 1.0 M, 200°C, 450 psia in N_2, 20 mins.

According to **Figure 24**, increasing the acetone content while fixing that of cyclopentanone results in a relatively constant rate of formation of [C]-activated products at 80 – 90 mmol.g^{-1}.h^{-1}. Meanwhile, the rate of formation of [A]-activated products increases proportionally with the introduced amount of acetone. The unchanged rate over [C]-activated species is also observed when cyclopentanone undergoes an MgO-NC-catalyzed cross-aldol condensation with benzophenone (B) – a carbonyl without α-Hs – in decalin at 250°C (**Appendix E**). For each 2-hour run, the concentration of cyclopentanone was fixed at 1.0 M while that of benzophenone varied from 0.25 M to 0.75 M. Results show that the total rate of formation of [C]C and [C]B is almost constant at 19 mmol.g^{-1}.h^{-1}. In addition, the [C]B-to-[C]C molar ratio is also proportional to the B-to-C feed ratio as observed in the scenario between C and A. This feature will be later discussed, following

the comprehension of kinetic models. Most importantly, it can be affirmed up to this point that on MgO-NC, the α-H abstraction of cyclopentanone – which dominates the catalytic surface through chemisorption – is kinetically relevant.

2.4.2. Selectivity to self- and cross-aldol condensation products. Compatibility of Langmuir-Hinshelwood- and Eley-Rideal-typed nucleophilic attacks
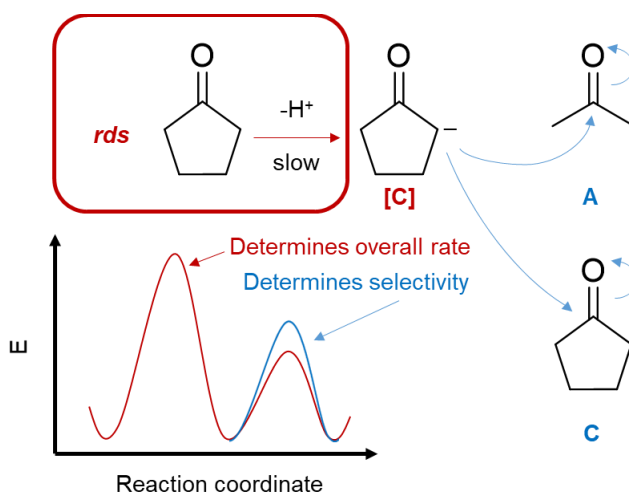
Figure 25. Schematic comparison between energy barriers of deprotonation and C-C coupling for cyclopentanone-acetone cross-aldol condensation.

Despite deprotonation being rate-limiting in the MgO-NC-catalyzed cyclopentanone-acetone cross-aldol condensation, the product distribution can be governed by subsequent C-C coupling steps. In other words, α-H abstraction possesses the highest activation energy, but energy barriers for nucleophilic attacks are probably indispensable (**Figure 25**). In this section, we examine the accordance of the observed [C]A-to-[C]C and [A]A-to-[A]C molar ratios with heterogeneous catalysis reaction models

proposed by Langmuir-Hinshelwood and Eley-Rideal [32,33]. As deprotonation is kinetically relevant at 200°C, this step is assigned a rate constant k_1. Meanwhile, adsorption and C-C coupling are pseudo-equilibrated and associate with equilibrium constants. For sake of simplicity, we only correlate the [C]A-to-[C]C ratio to the A-to-C feed ratio since cyclopentanone deprotonation is evidently more favorable than that of acetone (**Table 3**).
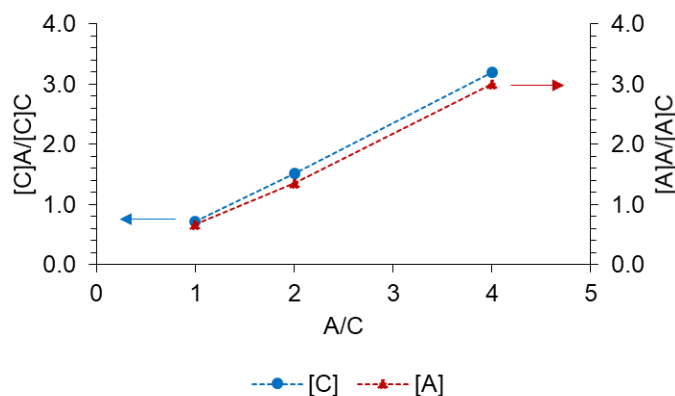
Figure 26. Variation of [C]A-to-[C]C and [A]A-to-[A]C product ratios to the acetone-to-cyclopentanone feed ratio.

Reaction conditions: 0.20 g of MgO-NC, $C_{\text{cyclopentanone 0}} = 1.0$ M, 200°C, 450 psia in N_2, 20 mins.

Both reaction models start with the adsorption of a cyclopentanone molecule from liquid cyclohexane to an Mg^{2+} site * of MgO-NC, followed by α-C-H cleavage to generate cyclopentenolate [C]*. This enolate then attacks an adjacent molecule of C or A provided from either the catalytic surface (Langmuir-Hinshelwood) or liquid cyclohexane (Eley-Rideal). The newly-formed aldolate eventually adapts the initially removed, O^{2-}-bound α-H, undergoes dehydration and diffuses into liquid cyclohexane. Also for sake of simplicity,

all surface intermediates are displayed here without electric charges. The molar concentration ratio between [C]A and [C]C is then derived as the ratio between their corresponding instantaneous rates of formation:

Langmuir-Hinshelwood model

$$C \quad + \quad * \quad \leftrightarrow \quad\quad C* \quad\quad\quad\quad K_C = \frac{C_{C*}}{C_C C_*}$$

$$A \quad + \quad * \quad \leftrightarrow \quad\quad A* \quad\quad\quad\quad K_A = \frac{C_{A*}}{C_A C_*}$$

$$C* \quad\quad\quad \rightarrow \quad\quad [C]* \quad\quad\quad\quad k_1$$

$$[C]* \quad + \quad A* \quad \leftrightarrow \quad\quad *[C]A \quad + \quad * \quad\quad K_{C-A} = \frac{C_{*[C]A} C_*}{C_{[C]*} C_{A*}}$$
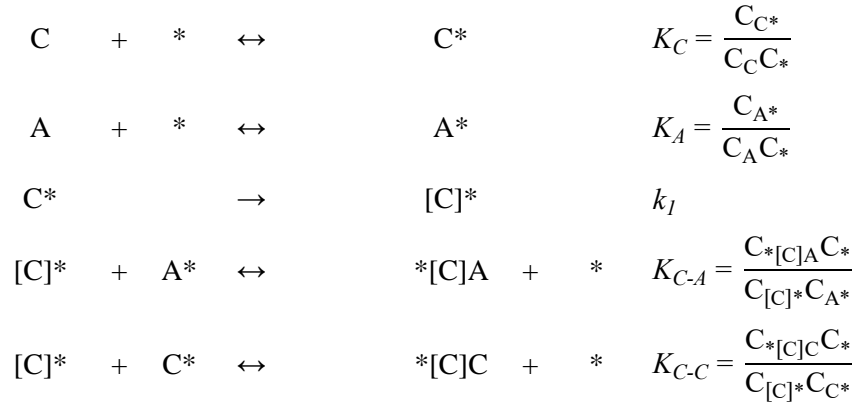
$$[C]* \quad + \quad C* \quad \leftrightarrow \quad\quad *[C]C \quad + \quad * \quad\quad K_{C-C} = \frac{C_{*[C]C} C_*}{C_{[C]*} C_{C*}}$$

$$\frac{C_{[C]A}}{C_{[C]C}} = \frac{r_{[C]A}}{r_{[C]C}} = \frac{C_{*[C]A}}{C_{*[C]C}} = \frac{\dfrac{K_{C-A} C_{[C]*} C_{A*}}{C_*}}{\dfrac{K_{C-C} C_{[C]*} C_{C*}}{C_*}} = \frac{K_{C-A} C_{A*}}{K_{C-C} C_{C*}} = \frac{K_{C-A}(K_A C_A C_*)}{K_{C-C}(K_C C_C C_*)} = \frac{K_{C-A} K_A C_A}{K_{C-C} K_C C_C}$$

Eley-Rideal model

$$C \quad + \quad * \quad \leftrightarrow \quad\quad C* \quad\quad\quad\quad K_C = \frac{C_{C*}}{C_C C_*}$$

$$C* \quad\quad\quad \rightarrow \quad\quad [C]* \quad\quad\quad\quad k_1$$

$$[C]* \quad + \quad A \quad \leftrightarrow \quad\quad *[C]A \quad\quad\quad\quad K'_{C-A} = \frac{C_{*[C]A}}{C_{[C]*} C_A}$$
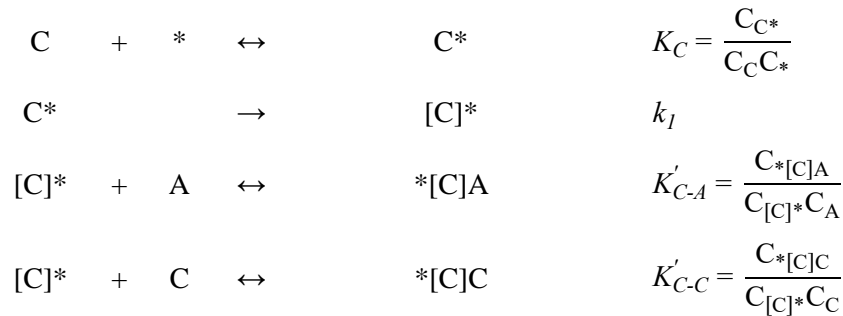
$$[C]* \quad + \quad C \quad \leftrightarrow \quad\quad *[C]C \quad\quad\quad\quad K'_{C-C} = \frac{C_{*[C]C}}{C_{[C]*} C_C}$$

$$\frac{C_{[C]A}}{C_{[C]C}} = \frac{r_{[C]A}}{r_{[C]C}} = \frac{C_{*[C]A}}{C_{*[C]C}} = \frac{K'_{C-A} C_{[C]*} C_A}{K'_{C-C} C_{[C]*} C_C} = \frac{K'_{C-A} C_A}{K'_{C-C} C_C}$$

Clearly, both reaction models suggest that the [C]A-to-[C]C ratio increases proportionally to the A-to-C feed ratio. Such correlation also applies to the [A]A-to-[A]C feed ratio and agrees with the trend shown in **Figure 26**. Additionally, the derived equations indicate that the product distribution also depends on C-C coupling equilibrium constants. Since we are unable to determine K_{C-A}, K_{C-C}, K'_{C-A} and K'_{C-C} explicitly, it is hard to claim which model best reflects the observed [C]A-to-[C]C and [A]A-to-[A]C ratios. The only comparison to be confirmed via experiments and DFT is K_C betters K_A.

In case of an equimolar feed, a [C]A-to-[C]C ratio being less than 1 suggests that the actual equation also has a slope being less than 1. Qualitatively, if the equilibrium constant of a [C]*-cyclopentanone interaction is higher than that of a [C]*-acetone interaction, both reaction models can rationalize the results in **Figure 26**. On the other hand, if the equilibrium constant of a [C]*-acetone interaction is higher, only the Langmuir-Hinshelwood model satisfies the observed product distribution. This is because the included adsorption constant ratio – which is consistently less than 1 – can outweigh the C-C coupling constant ratio to render the overall slope less than 1. At 200°C, such adsorption constant ratio may significantly increase from that at room temperature but remains far from unity.

Alternatively, the Langmuir-Hinshelwood reaction model allows the [C]A-to-[C]C ratio to be expressed in terms of surface coverages:

$$\frac{C_{[C]A}}{C_{[C]C}} = \frac{r_{[C]A}}{r_{[C]C}} = \frac{K_{C-A}K_A C_A}{K_{C-C}K_C C_C} = \frac{K_{C-A}\theta_A}{K_{C-C}\theta_C}$$

From this equation, we ascribe different concentrations of [C]A and [C]C to different amounts of A and C as surface intermediates. Since K_C is greater than K_A, an equimolar feed means θ_C is also greater than θ_A. That is, cyclopentenolate is probably surrounded by a larger population of adsorbed molecules of cyclopentanone. Meanwhile, each C-C coupling equilibrium constant correlates to an activation free energy barrier, which consists of enthalpic and entropic terms, according to Wang *et al.* [74]:

$$\ln\left(\frac{K_{C\text{-}A}}{K_{C\text{-}C}}\right) = -\frac{\Delta G^{TS}_{[C]A}\text{-}\Delta G^{TS}_{[C]C}}{R\text{T}} = -\frac{\left(\Delta H^{TS}_{[C]A}\text{-}T\Delta S^{TS}_{[C]A}\right)\text{-}\left(\Delta H^{TS}_{[C]C}\text{-}T\Delta S^{TS}_{[C]C}\right)}{R\text{T}}$$

$$= \frac{\Delta H^{TS}_{[C]C}\text{-}\Delta H^{TS}_{[C]A}}{R\text{T}} + \frac{\Delta S^{TS}_{[C]A}\text{-}\Delta S^{TS}_{[C]C}}{R}$$

The authors studied aldol condensations of C_2-C_4 enolates with formaldehyde over TiO_2, finding that each cross-aldol condensation product dramatically outnumbered the corresponding self-aldol condensation product. Such result was ascribed to a lower activation free energy barrier for the $[C_i]$-formaldehyde coupling step, due to less negative entropy loss with respect to gaseous formaldehyde. However, in our case, we instead compare activation free energy barriers for [C]-C and [C]-A coupling steps with respect to adsorbed species. Analogous to the Ru/TiO_2-catalyzed ketonization of carboxylic acids [75], both ΔH^{TS} and ΔS^{TS} are positive values. Due to the larger size of cyclopentanone compared to acetone, a [cyclopentenolate…cyclopentanone#] has a higher number of conformations than a [cyclopentenolate…acetone#] does. In other words, $\Delta S^{TS}_{[C]C} > \Delta S^{TS}_{[C]A}$. Nevertheless, the former transition state involves a less electrophilic carbonyl

carbon and experiences additional enolate-carbonyl steric repulsion, therefore more energy is required for stabilization, or $\Delta H_{[C]C}^{TS} > \Delta H_{[C]A}^{TS}$. A possible activation enthalpy – activation entropy compensation effect will provide relatively identical values of K_{C-A} and K_{C-C}. Under this circumstance, the remarkably higher cyclopentanone uptake on the MgO-NC surface becomes the decisive factor contributing to the preference of [C]C over [C]A.

The analysis above technically requires justification through an energy diagram comparing [C]C and [C]A, analogous to **Figure 22**. DFT calculations for such diagram remain in progress. Depending on DFT results, we know which factor decides the observed [C]A-to-[C]C ratio (less than 1, provided equimolar feed). If [C]A formation has a lower activation free energy, the enthalpic effect is more important. In this case, [C]A is less abundant than [C]C because the lower activation free energy is outweighed by the superior surface coverage of C. Conversely, if [C]C formation has a lower activation free energy, the entropic effect is more important. In this case, both the stability of [cyclopentenolate…cyclopentanone[#]] and the superior surface coverage of C contribute to the preference of self-aldol condensation.

2.5. Summary

The main conclusions of the study are the following:

i. Under the catalysis of basic MgO-NC, the cross-aldol condensation of cyclopentanone (C) and acetone (A) provides a predominant combined selectivity to [C]-activated dimer products. This suggests that cyclopentanone is not only more acidic than acetone, but the α-H abstraction of the former on MgO-NC also significantly inhibits that of the latter.

ii. MgO-NC renders the α-H abstraction of each ketone reactant rate-limiting. For cyclopentanone, the total rate of formation of [C]-activated dimer products is unchanged when excess amounts of acetone are mixed with a fixed cyclopentanone content. Meanwhile, for acetone, the total rate of formation of [A]-activated dimer products increases proportionally to such excess amounts.

iii. The product distribution, particularly the ratio of molar concentrations of [C]A and [C]C, is however governed by the C-C coupling step. Although cyclopentanone betters acetone in both chemisorption and deprotonation on MgO-NC, the cross-to-self coupling ratio depends on both the feed composition and the extent of each cyclopentenolate-electrophile interaction. So far, for an equimolar feed, both Langmuir-Hinshelwood and Eley-Rideal reaction models can fit experimental results which show the preference of [C]C over [C]A. The only confirmed factor contributing to such preference is the higher population of cyclopentanone electrophiles in proximity to a cyclopentenolate.

3. Mechanistic insights of water-induced cyclopentanone self-aldol condensation on OTS-functionalized MgO catalysts

3.1. Introduction

Thermal pyrolysis is one of the most promising approaches to decompose biomass into separate stages, all of which can be starting materials for biofuel syntheses [1-10]. Due to a carbon range compatible to that of gasoline-kerosene (5 – 15 atoms per molecule), medium-staged furanic compounds have been subject to several upgrading reactions, including C-C couplings [2]. Since furfural – a representative of this stage – is unstable and may initiate catalyst coking, it is a good strategy to convert it to the more stable cyclopentanone through a two-step metal-catalyzed aqueous hydrogenation known as the Piancatelli ring rearrangement [15,16, 76]. Among potential transformation routes, cyclopentanone can readily undergo aldol condensations to generate α,β-unsaturated dimeric ketones, followed by hydrodeoxygenation into consumable biofuels [27,34,69,77]. Recent works have shown that these aldol condensations are specifically favored in water-free conditions and under the catalysis of a solid base (e.g. MgO) [25,26,35,78]. Despite a high basic density, MgO prepared via nitrate-citrate combustion deactivated rapidly at 150 – 200°C after short reaction times due to surface accumulation of *in situ* water and over-condensates [70]. Such drawback was overcome by organosilane functionalization (e.g. OTS) on either bare MgO or an MgO-SiO₂ solid mixture. The catalytic stability of a much less basic hybrid MgO was tremendously increased up to hours along with respectable conversions. As hydrophobic OTS molecules mitigated the formation of an *in*

situ water layer on MgO surface, a sizeable amount of active sites remained accessible for cyclopentanone to generate enolates. Silane groups also facilitated the removal of newly-formed 2-cyclopentylidenecyclopentanone so that sequential aldol condensations leading to oligomerization were minimized. MgO-OTS and MgO@mSiO$_2$-OTS were initially less active than unmodified MgO but eventually outperformed it provided sufficient tolerance to poisons. In addition, OTS-functionalized MgO remarkably resisted the attack of external water. Starting from identical water-free cyclopentanone conversions, MgO and MgO@mSiO$_2$-OTS behaved vastly differently following the addition of 2 mL of water to the reaction mixture at 150°C. While unmodified MgO lost about 80% of its original activity, MgO@mSiO$_2$-OTS almost retained the water-free performance. A much smaller *in situ* water volume compared to the added one also highlighted economic benefits of OTS functionalization in protecting MgO active sites.

The influence of water, however, can be more complicated than what has been reported. In general, water can participate in organic syntheses as a reactant, a product, a medium or an additive which promotes or inhibits catalytic activity [39,79-102]. The Fischer-Tropsch synthesis (FTS) is among reactions in which water exhibits a rate-enhancing effect [103-109]. Introducing water to the oil phase has been found to lower the energy for CO dissociation over certain supported metal catalysts [110-126]. By this manner, water helps propagate the hydrocarbon chain, increase the desirable C$_{5+}$ selectivity and alleviate methanation [113,127-140]. Particularly, Shi *et al.* [141] showed that both a condensed aqueous phase and a water-in-decalin emulsion improved the FTS catalytic activity and the C$_5$-C$_{20}$ fraction over Ru/CNT-Al$_2$O$_3$-MgO. In this case, water functioned

as a H-shuttling mediator [142-144] by capturing a surface H to protonate a surface CO and thus facilitating the rate-limiting H-assisted CO cleavage [116, 145]. Through competing with H_2 for active sites, water also minimized the secondary hydrogenation of newly-formed alkenes and enhanced the chain growth rate [146]. From another study, Iglesia [128] suggested that a permanent liquid water content increased the FTS catalytic activity by allowing syngas to access sites in narrow porous regions. Such promotional effect was more evident on catalyst supports with a small pore size [147-149]. Iglesia [113] later stated that on Co/SiO_2, water could hinder chain termination via H abstraction at internal positions of alkyl chains, followed by secondary olefin isomerization reactions. The ability of water to modify kinetics and product distribution was further addressed when Zhao [150] studied furfural hydrogenation over $Pd/\alpha-Al_2O_3$. The author discovered that the aqueous phase not only enhanced conversion with respect to that in cyclohexane but also shifted the favored primary product from tetrahydrofurfural to furfuryl alcohol. These results were ascribed to a greatly reduced activation energy when a surface water molecule shuttled the first H to a carbonyl O. Such reduction even changed the rate-limiting step into the subsequent hydrogenation.

Apart from biomass upgrading processes, other reactions of high industrial importance were investigated and analyzed for the rate-enhancing effect of water [151-160]. In such reactions, the mechanism for water assistance was not only limited to H-shuttling but also expanded to solvation [161,162] or selective oxidation of surface species [163-166]. That is, water stabilized chemisorbed species (reactants, intermediates and

transition states) through hydrogen-bonding networks and effectively accelerated rate-limiting steps [167-169].

On the other hand, water is inarguably responsible for several rate-inhibiting effects on heterogeneous catalysis [170-177]. The competitive adsorption of water is mostly associated with detrimental site blockage [178-180]. FTS studies [181-197] simultaneously demonstrate that water can condense in pores of a catalyst support, re-oxidizing metal crystallites (e.g. Co, Fe) and depopulating active sites. Such damage becomes more evident at high CO conversions as water itself is an FTS by-product. According to Holmen *et al.* [198], some water-induced re-oxidation can contribute to both catalyst and support sintering processes [199-202]. Regarding oxidation-resistant catalysts [203], high concentrations of water may still facilitate the water-gas-shift side reaction to generate undesirable CO_2. In fact, Shi [141] highlighted that a water-in-decalin emulsion bettered an aqueous phase in stabilizing $Ru/CNT-Al_2O_3-MgO$ since the former medium properly balanced between forming and desorbing C_5-C_{20} products. For base-catalyzed reactions, the negative impacts of water have been so far more apparent. In our previously studied MgO-catalyzed cyclopentanone self-aldol condensation [70], neither rate enhancement was observed following exposures of two MgO catalysts to 2 mL of external water. Pure MgO even lost most site pairs due to the formation of inactive layers of $Mg(OH)_2$. The only noteworthy feature was that water clusters [204,205] did less harm to the OTS-functionalized MgO. That is, water in such case formed droplets rather than a layer, therefore deactivation occurred much more slowly. In other words, functionalization with organosilanes did not eliminate water susceptibility but instead alleviated this issue to

prolong material stability. However, the fact in which water hardly promoted catalytic activity of MgO-based solids can be partially ascribed to its excess amount. Only a limited water content may improve catalytic performance, as shown by other recent studies [206-210]. Moreover, to our knowledge, no work has been reported on the supportive role of water over organic phase aldol condensations. Therefore, we will address such aspect by exposing both MgO and its OTS-modified versions to considerably low water volumes. This task also supplements our initial work and helps fully comprehend how water alters catalytic behaviors.

In addition, the current topic will correlate the water-exposed catalytic activity to the hydrophobic-hydrophilic nature of an MgO surface. Previous studies proposed that in a non-polar organic phase, water molecules would tend to find the closest polar domain to settle down [55,56]. For hydrophilic MgO, water strongly competes for Mg^{2+}-O^{2-} site pairs and form a diffusion-limiting film. Meanwhile, hydrophobic MgO-OTS partially inhibits such competitive chemisorption, leaving a sizeable amount of external water molecules in the oil phase. For complete evaluation, we have adjusted the OTS loading on MgO samples and found that the density of these moieties significantly affects the chemisorption of both cyclopentanone and water under reaction conditions. Therefore, it is possible to modify the hydrophobicity of MgO for appropriately tuning its stability and catalytic activity in the presence of water.

3.2. Experimental

3.2.1. Synthesis of catalytic materials

3.2.1.1. MgO-NC

MgO-NC was synthesized via nitrate-citrate combustion, the method described elsewhere [70]. Briefly, 25.6 g of $Mg(NO_3)_2.6H_2O$ (Aldrich, 99.9%, 0.1 mol) was mixed with 30 mL of water and stirred vigorously for 15 mins at 80°C. Then, a 20-mL water solution containing 19.2 g of citric acid (Aldrich, 99.5%, 0.1 mol) was added into the mixture. The resulting solution was continuously heated and stirred until half of the liquid vaporized, leaving a viscous gel. This gel was calcined overnight under static air at 550°C to obtain a high-surface-area MgO solid named MgO-NC (for nitrate-citrate combustion).

3.2.1.2. Octadecyltrichlorosilane-functionalized MgO

The as-prepared MgO-NC was then hydrophobized, starting with the dropwise addition of 0.45 mL of water onto 1 g of MgO-NC. The wetted material was suspended in a 1:50 v/v OTS-toluene solution [70,211]. The suspension was shaken vigorously for 10 mins, stirred overnight at room temperature, centrifuged and washed thrice with ethanol. The separated solid was dried overnight at 110°C to yield the OTS-functionalized MgO, in which OTS molecules displaced silanol groups to generate a hydrophobic surface. Materials synthesized from this method were generalized as MgO(x)-OTS(y). Such denotation means a catalyst nominally containing x wt.% of MgO and y wt.% of OTS.

3.2.1.3. Removal of the alkyl chains of MgO-OTS by oxidation

The as-prepared MgO(70)-OTS(30) was calcined under a temperature program for complete combustion of octadecyl groups. In details, a calculated amount of MgO(70)-OTS(30) was placed in the middle of a glass tube. Both ends of the tube were packed with glass wool. The tube was then horizontally connected to a furnace and applied with a 40-sccm air flow at room temperature. MgO(70)-OTS(30) was first heated to 300°C under a ramp rate of 1°C.min^{-1}. The temperature was stabilized at 300°C for 1 hour before increased to 450°C under the same ramp rate. The sample was maintained at 450°C for 4 hours, then cooled down overnight and finally collected. The obtained solid was denoted as MgO(70)-OTS(30) PC. PC here stands for post-calcination, as this solid was prepared through thermal removal of the alkyl chains of MgO(70)-OTS(30).

3.2.2. Characterization

3.2.2.1. TGA

The final content of OTS in the MgO(70)-OTS(30) sample was determined by thermogravimetric analysis (TGA). Analogously to **Section 1.2.2**, 46.91 mg of MgO(70)-OTS(30) was analyzed by heating with a linear ramp under flow of an Ar-air mixture, starting from 40°C and increased by 2°C.min^{-1}.

3.2.2.2. BET

The specific surface area of MgO(70)-OTS(30) PC was obtained on a Micromeritics 2010 instrument. The values of MgO-NC and MgO(70)-OTS(30) [70] were

also used as references. The former value was combined with mass spectra obtained during the TGA of MgO(70)-OTS(30) to quantify the distribution of OTS functionalities on the catalyst. For sake of simplicity, we assume complete hydrolysis of the chloro-groups in OTS and monodentate anchoring. Accordingly,

$$x = \frac{n_{OTS} \times N_A}{A_{MgO-NC}} = \frac{\dfrac{m_{C_{18}H_{37}Si(OH)_2O-}}{MW_{C_{18}H_{37}Si(OH)_2O-}} \times N_A}{m_{MgO-NC} \times S_{BET\ MgO-NC}}$$

or

$$x = \frac{\dfrac{m_{C_{18}H_{37}Si(OH)_2O-}}{MW_{C_{18}H_{37}Si(OH)_2O-}} \times N_A}{\left[1 - m_{C_{18}H_{37}Si(OH)_2O-}\right] \times S_{BET\ MgO-NC}}$$

where

x	=	molecules of OTS, or $C_{18}H_{37}Si(OH)_2O-$, anchored per unit area of MgO-NC in MgO(70)-OTS(30)
$m_{C_{18}H_{37}Si(OH)_2O-}$	=	TGA-based content of OTS in MgO(70)-OTS(30) [g.g catalyst^{-1}]
m_{MgO-NC}	=	TGA-based content of MgO-NC in MgO(70)-OTS(30) [g.g catalyst^{-1}]

3.2.2.3. CO_2-TPD

The basic densities of MgO(70)-OTS(30), MgO(70)-OTS(30) PC and MgO(85)-OTS(15) were characterized via temperature-programmed desorption (TPD) of adsorbed CO_2 following the method described elsewhere [46]. The CO_2-TPD result of MgO-NC

[70] was also used as a reference. Analogously to **Section 1.2.2**, 100 mg of catalyst was heated to 200°C in the TPD system with a ramp rate of 10°C.min⁻¹, under a He flow rate of 30 mL.min⁻¹ and then cooled down to room temperature. A CO_2 flow rate of 30 mL.min⁻¹ was then passed through the sample for 30 mins, followed by a 2-hour purge with He to remove any physisorbed CO_2. The TPD was performed under the same He flow rate by heating to 600°C with a ramp rate of 10°C.min⁻¹.

3.2.3. Estimation of the added water volume

For each MgO catalyst, a series of reactions were conducted at 200°C with increasing added water volumes. Despite being liquid in the feeding cylinder, water could exist in both vapor and condensed states after entering the reactor, resulting in different rate trends. The mole of added water was calculated based on the saturated vapor pressure of water at 200°C (15.3 atm). Using the ideal gas question (**Appendix F**), with the empty volume of the reactor being 50 mL, the highest water vapor volume under given reaction conditions was 355 μL. Different external water amounts – 200 μL, 355 μL, 700 μL, 1000 μL and 1500 μL – therefore were injected to study the water-induced catalytic activity. The first two volumes reflected water vapor, while the remaining three indicated a newly-formed liquid water phase with respect to the bulk cyclohexane.

3.2.4. Catalytic measurements

3.2.4.1. Reactor operating conditions and analysis methods

Cyclopentanone self-aldol condensation was conducted in N_2 atmosphere as described elsewhere [70]. For each run, a cyclohexane-catalyst mixture was introduced into a 100-mL Parr reactor. The system was then purged with N_2, compressed to 300 psia and heated to 200°C. The feed – consisting of cyclopentanone, toluene (internal standard) and a designated water volume – was injected to a 30-mL feeding cylinder, pressurized to 800 psia and entered the reactor when the set temperature was stabilized. The stirring speed remained 750 rpm, but the reaction time varied among catalysts and was intentionally chosen to measure initial rates with conversions below 20%. These conversions guaranteed that external water significantly outnumbered *in situ* water. The post-reaction suspension was cooled down in an ice bath and centrifuged for 10 mins. The separated liquid was analyzed by GC-FID.

3.2.4.2. Quantification of active sites under reaction conditions

Apart from CO_2-TPD, active sites of MgO catalysts were quantified via titration with propanoic acid. Titration experiments resembled Wang *et al.*'s work [48], where propanoic acid was added to irreversibly block TiO_2 acid-base site pairs during acetone self-aldol condensation. This controlled site blockage helped determine the amount of active sites of TiO_2. Analogously, active sites of MgO-NC, MgO(70)-OTS(30) and dealkylated MgO(70)-OTS(30) PC were subject to isothermal titration with propanoic acid during cyclopentanone self-aldol condensation. The operating temperature and initial

cyclopentanone concentration were respectively fixed at 150°C and 1.8 M, while the mass of each catalyst and reaction time were adjusted for initial rates. Propanoic acid was again assumed to block acid-base site pairs via a monodentate mode; that is, one mole of acid was irreversibly adsorbed by one mole of Mg^{2+}-O^{2-}. The acid uptake was the concentration difference between time zero – when the acid entered the catalyst-filled reactor – and the final time. If all acid molecules were captured by active sites and no side reactions occurred, such difference would be the assigned initial acid concentration, or equivalently, the introduced acid volume. Based on Wang *et al.*'s work [48], the amount of propanoic acid in the feed was increased until it suppressed the self-aldol condensation. In other words, the initial rate was manipulated to decrease continuously from the acid-free value to zero as more propanoic acid entered the system. If the decline was consistently linear to the acid uptake, the forecast x-intercept would come directly into the equation in **Section 2.2.3.2** to determine the basic density. Conversely, if the decline included an initial steep drop followed by a more gradual one, zero extrapolation to the x-axis would instead apply to the early acid uptakes. Under this circumstance, isothermal titration with propanoic acid would deviate to estimation of the strongest basic sites.

3.3. Results and Discussion

3.3.1. Characterization

3.3.1.1. TGA
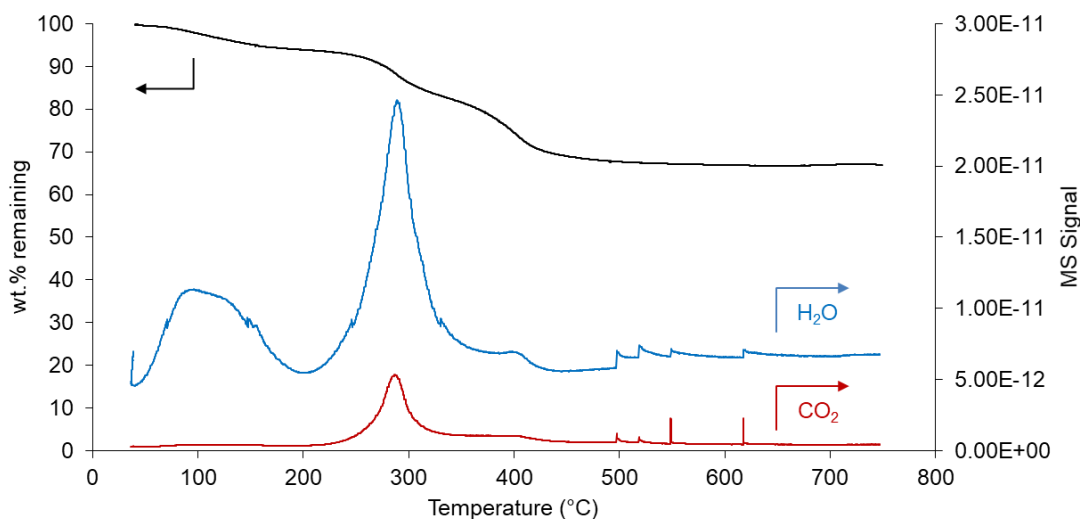
Figure 27. TGA analysis and mass spectra of CO_2 and water evolved from MgO(70)-

OTS(30).

Figure 27 shows two distinct mass losses from the TGA of MgO(70)-OTS(30).

The first loss, from 40°C to 200°C, is ascribed to the removal of physisorbed water. The

second one, from 250°C to around 400°C, results from the combustion of OTS octadecyl

groups in air. By quantifying the evolution of CO_2 and H_2O in this region, provided Cls

are hydroxyl-substituted and Si is retained during TGA, one can determine the original

OTS loading in MgO(70)-OTS(30). The calculated value – approximately 12 wt.%

(**Appendix G**) – is lower than the nominal 30 wt.% added during preparation. Such value

indicates that a fraction of OTS initially added to MgO-NC is not effectively anchored and

is lost during post-synthesis washes in ethanol and centrifugation. The greater difference between actual and nominal OTS contents – with respect to those of MgO@mSiO$_2$-OTS [70] – correlates to the absence of mSiO$_2$, which improves chemically displaceable surface OHs for OTS. Nevertheless, the remaining organosilane molecules are firmly anchored, thus being able to tolerate high temperatures before decomposition.

3.3.1.2. BET

Table 4. Surface area, pore size and pore volume of MgO-OTS PC.

Catalyst	S$_{BET}$	Pore size	Pore volume
	m^2.g^{-1}	nm	cm^3.g^{-1}
MgO-NC	97	9.5	0.22
MgO(70)-OTS(30)	51	3.8	0.04
MgO(70)-OTS(30) PC	61	13.1	0.19

Table 4 compares BET properties of MgO-NC, MgO(70)-OTS(30) and MgO(70)-OTS(30) PC. From MgO-NC to MgO(70)-OTS(30), the ratio of surface areas (1.9) is relatively close to the ratio of pore diameters (2.5). The difference in pore radius (2.85 nm) is interestingly compatible with the mean thickness of an OTS monolayer (2.6 ± 0.2 nm) [212]. Substituting the TGA-based content of MgO(70)-OTS(30) and the BET surface area of MgO-NC into the equation in **Section 3.2.2.2** yields approximately 3 molecules of OTS attached to a nm^2 of MgO-NC, or as defined above x = 3 nm^{-2}. This

areal density is much higher than that of MgO@mSiO$_2$-OTS and considerably limits active site pairs to accommodate N$_2$ and cyclopentanone molecules.

For MgO(70)-OTS(30) PC, temperature-programmed calcination slightly increases the surface area with respect to its precursor, MgO(70)-OTS(30). This is because only octadecyl groups are removed as gaseous CO$_2$ and H$_2$O at 450°C. The inorganic parts of OTS, on the other hand, are thermostable and remain chemically bonded to MgO-NC. In other words, each C$_{18}$H$_{37}$Si(OH)$_2$O- is technically decomposed into CO$_2$, H$_2$O and surface-bound SiO$_2$. Such SiO$_2$ fragments do not redisperse MgO domains as mesoporous silica does [70] but exist as anchors with a density resembling that of OTS. As a result, the surface area of MgO(70)-OTS(30) PC is close to that of MgO(70)-OTS(30) rather than to that of MgO-NC, despite noticeably reduced mass transfer limitation.

3.3.1.3. CO_2-TPD
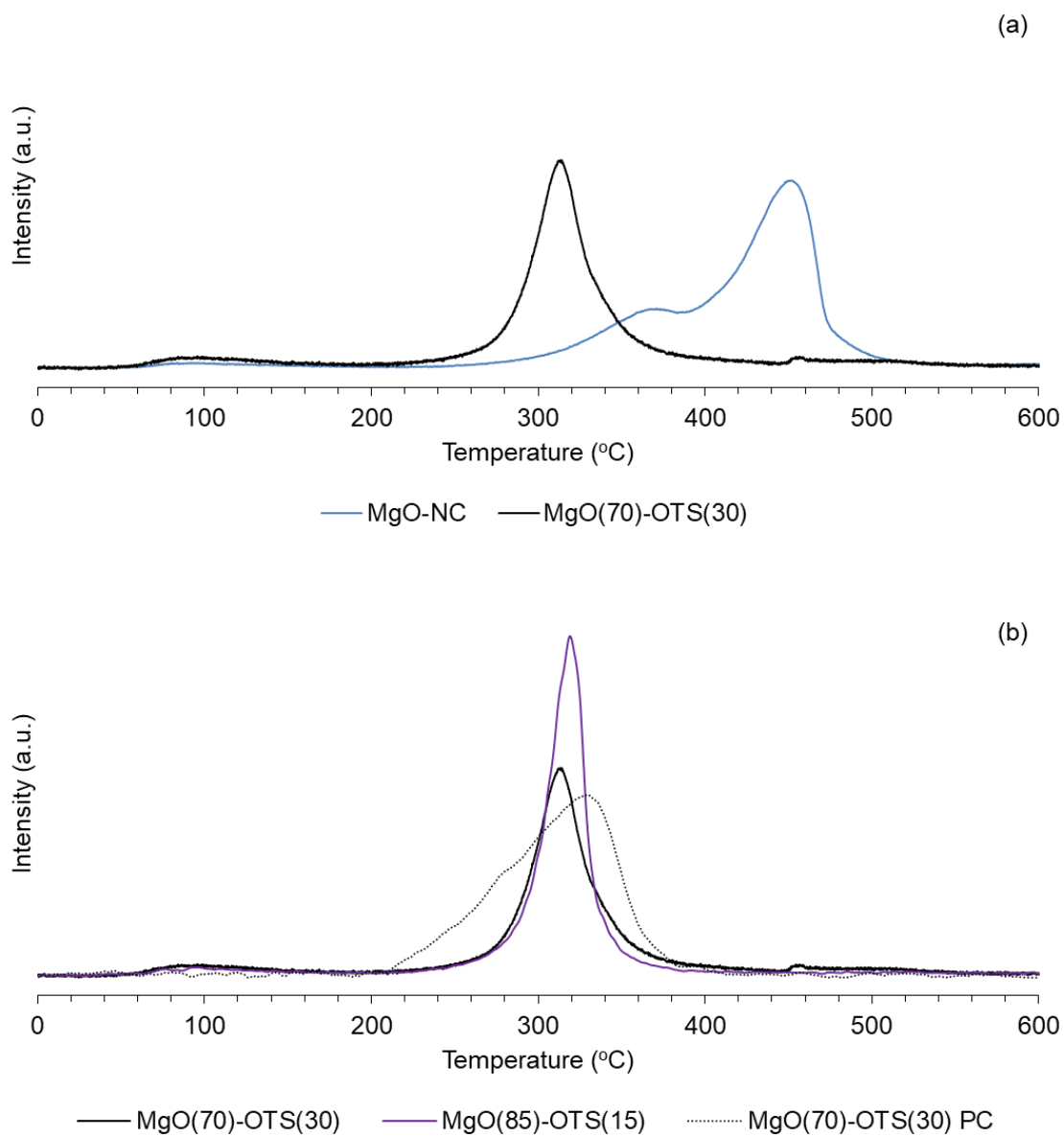
Figure 28. CO_2-TPD on directly OTS-functionalized MgO catalysts.

To quantify basic sites of the as-prepared MgO catalysts, we first used the conventional TPD of adsorbed CO_2. Calculated basic densities are shown in **Table 6**, with certain values also compared to those obtained from titration with propanoic acid.

In **Figure 28a**, while MgO-NC exhibits peaks of both strong and medium basicity, MgO(70)-OTS(30) shows much more uniform sites indicated by a single peak centered at 320°C. According to **Section 1.3.1**, this peak is attributed to medium basic strength. Analogously to MgO@mSiO$_2$-OTS [70], all of the strongest basic sites are eliminated following the deposition of OTS on MgO-NC. The active sites of MgO(70)-OTS(30) are of slightly lower medium basic strength with respect to those of MgO@mSiO$_2$-OTS, despite MgO(70)-OTS(30) having a greater basic density. For MgO(85)-OTS(15), **Figure 28b** shows that this catalyst also has uniform sites with the medium basic strength similar to that of MgO(70)-OTS(30). As less OTS molecules are deposited on the bare MgO-NC substrate, it is obvious that the amount of active site pairs on MgO(85)-OTS(15) increases.

For MgO(70)-OTS(30) PC – where MgO(70)-OTS(30) has been dealkylated at 450°C, **Figure 28b** still shows a peak centered close to 320°C. This peak confirms the unchanged medium basic strength since post-calcined SiO_2 fragments remain chemisorbed by the strongest basic sites. Nevertheless, there is a noticeable increase in the basic density. This is because the removal of octadecyl groups might have gained a sizeable amount of accessible sites for CO_2. Despite having respectable medium basic strength, such additional active sites would not readily chemisorb CO_2 while being sterically hindered by surface octadecyl groups.

3.3.2. Quantification of active sites under reaction conditions

Table 5. Intrinsic initial activities on various MgO catalysts at 150°C.

Catalyst	Intrinsic initial activity
	mol.g^{-1}.h^{-1}
MgO-NC	0.123
MgO(70)-OTS(30) PC	0.013
MgO(70)-OTS(30)	0.005

Table 5 displays intrinsic activities of as-prepared MgO catalysts at 150°C. These activities are measured under propanoic acid-free conditions. The displayed values reflect corresponding basic densities obtained from CO_2-TPD. That is, MgO-NC is the strongest basic catalyst while MgO(70)-OTS(30) is the weakest one. Dealkylation of MgO(70)-OTS(30) through temperature-programmed calcination at 450°C recovers some intrinsic activity for the hybrid material.
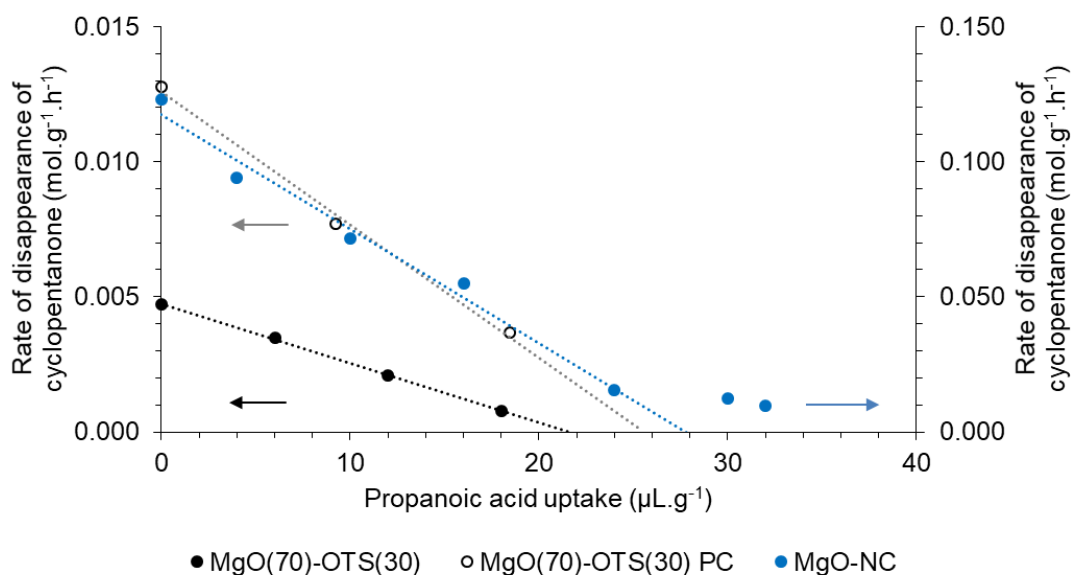
Figure 29. Propanoic acid-controlled cyclopentanone self-aldol condensation initial rates

on various MgO catalysts.

<u>Reaction conditions:</u> $C_{cyclopentanone\ 0}$ = 1.8 M, 150°C; 0.50 g of MgO-NC – 30 mins; 0.50 g

of MgO(70)-OTS(30) – 4 hours; 0.325 g of MgO(70)-OTS(30) PC – 2 hours.

Table 6. Basic densities of MgO-based catalysts.

Catalyst	CO$_2$-TPD		Propanoic acid titration	
	Strong sites	Medium sites	Strong sites	Medium sites
	$\mu mol.g^{-1}$	$\mu mol.g^{-1}$	$\mu mol.g^{-1}$	$\mu mol.g^{-1}$
MgO-NC	317	102	375	107
MgO(70)-OTS(30)	-	305	-	295
MgO(85)-OTS(15)	-	375	-	-
MgO(70)-OTS(30) PC	-	354	-	330

Propanoic acid titration curves of MgO-NC, MgO(70)-OTS(30) and MgO(70)-OTS(30) PC are shown in **Figure 29**. As no single propanoic acid peak was detected from GC-FID, MgO-NC, MgO(70)-OTS(30) and MgO(70)-OTS(30) PC irreversibly adsorbed all injected acid molecules. Data points corresponding to MgO(70)-OTS(30) and MgO(70)-OTS(30) PC both form linear decreasing trends, confirming that these catalysts have uniformly medium-strength basic sites. Corresponding zero extrapolations to the x-axis yield acid uptakes of 22 $\mu L.g^{-1}$ and 25 $\mu L.g^{-1}$. Using the equation in **Section 2.2.3.2**, the basic densities of MgO(70)-OTS(30) and MgO(70)-OTS(30) PC are 295 and 330 $\mu mol.g^{-1}$ respectively. These values agree well with CO_2-TPD results (**Table 6**).

On the other hand, the titration curve of MgO-NC shows two decreasing trends. The first linear drop is observed from the acid-free rate to the rate at 24 $\mu L.g^{-1}$, while the second one appears at higher acid uptakes. This non-linearity can be ascribed to diverse basic strengths of active sites, which is congruent to the CO_2-TPD curve of MgO-NC. Under such circumstance, the strongest basic sites of MgO-NC preferably attract and adsorb propanoic acid molecules. Only when most of these strongest sites are neutralized should the remaining sites – of lower basic strengths – be subject to titration. There could also exist some sites being inaccessible for propanoic acid so that even higher acid volumes may not suppress the rate. In other words, the rate may remain positive up to an acid uptake of 40 $\mu L.g^{-1}$ (536 $\mu mol.g^{-1}$) rather than zero-extrapolated at 28 $\mu L.g^{-1}$ (375 $\mu mol.g^{-1}$). As a result, it is considerable to quantify the strongest basic sites of each MgO catalyst by using the slope from the first data points. By applying this rule, the acid uptakes to titrate the strongest basic sites of MgO(70)-OTS(30) and MgO(70)-OTS(30) PC remain respective

78

x-intercepts in **Figure 29**. Conversely, only the first five points of MgO-NC are used to obtain an x-intercept at 28 μL.g^{-1} (375 μmol.g^{-1}), approximating 90% of the overall basic density measured from CO_2-TPD [46].

3.3.3. *Effect of water addition on specific reaction rates*
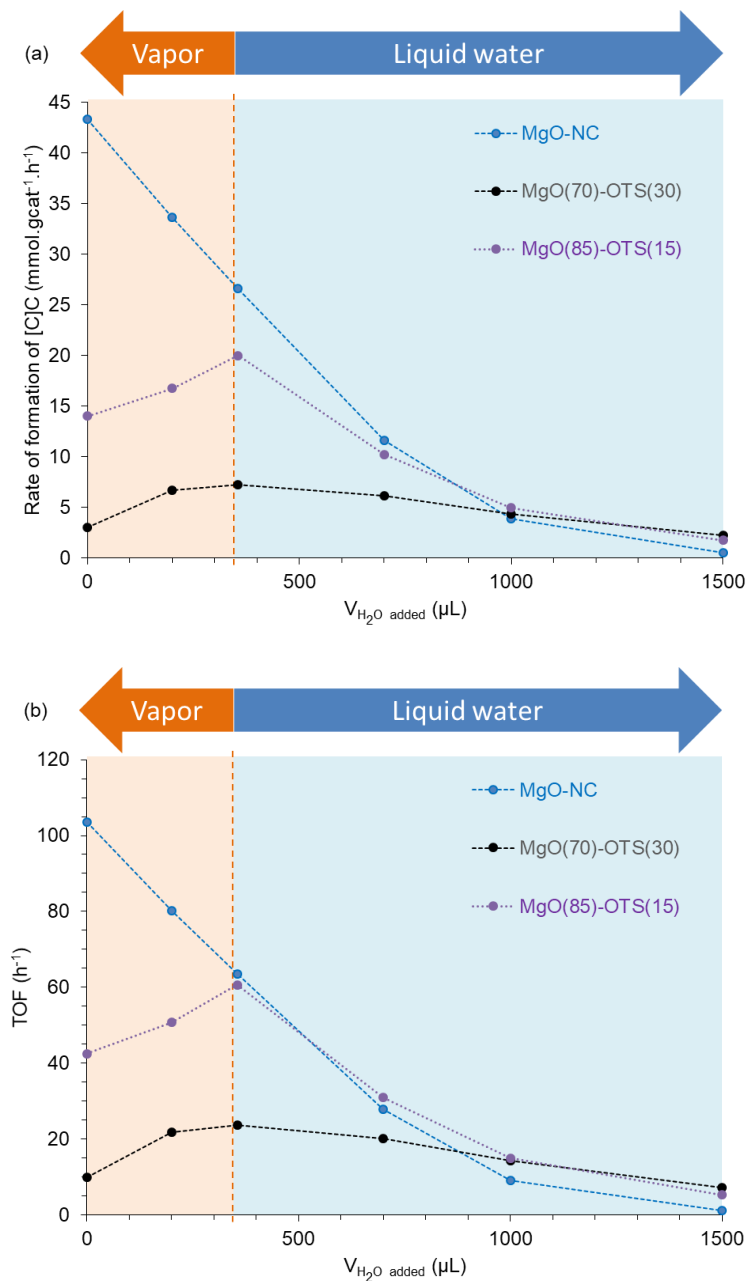
Figure 30. Effect of water addition on the catalytic performance of various MgO

catalysts: (a) Reaction rate, (b) TOF.

<u>Reaction conditions:</u> $C_{cyclopentanone\ 0} = 1.8$ M, 200°C.

Figure 30 indicates vastly different catalytic behaviors among MgO-NC, MgO(85)-OTS(15) and MgO(70)-OTS(30) when the amount of water added to the reactor increases. For MgO-NC, the rate drops sharply and consistently with increasing water contents, regardless of the state of water. Under this circumstance, water only displays negative effects. These include nucleating a diffusion-limiting film covering the surface, blocking active sites as inactive $Mg(OH)_2$ species and strongly inhibiting cyclopentanone chemisorption. Although MgO-NC is more active than MgO(85)-OTS(15) and MgO(70)-OTS(30) by 2.5 times and 10 times respectively, it has already lost 40% of activity at 355 μL of water. In excess water amounts, the rate per gram of MgO-NC drops into the range of those of MgO-OTS catalysts and is almost zero at 1500 μL of water.

For MgO(85)-OTS(15), the rate trend interestingly consists of two separate stages with a turning point at 355 μL of water vapor. From no water to 355 μL, the rate is enhanced by 42%. Beyond 355 μL, liquid water is formed in the bulk cyclohexane and the rate decreases rapidly as previously observed over MgO-NC. From 700 μL of water, the rate over MgO(85)-OTS(15) becomes lower than the water-free value, reflecting considerable site blockage.

For MgO(70)-OTS(30), the rate trend also resembles a volcano plot. Despite a water-free value of 4 times less than that over MgO(85)-OTS(15), the rate over MgO(70)-OTS(30) is analogously maximized at 355 μL of water vapor. Moreover, the rate enhancement is 140%, indicating a more pronounced positive effect of water addition. It is noteworthy that even at 700 μL and 1000 μL of water, the rate remains considerably higher than the water-free value. It is only lower when 1500 μL of water is added to the

reaction system; however, the value respectably approximates 70% of the water-free rate.

Such result, in contrast to the negligible rate over MgO-NC at 1500 μL of water, confirms

the significantly improved water resistance attained via OTS functionalization. This

finding is congruent to one of the claims from our previous study [70]. The then stability

of MgO-OTS and MgO@mSiO$_2$-OTS was displayed on a mass of catalyst x reaction time

basis, and now it is supplemented on an external water content basis.

Catalytic behaviors of MgO-OTS materials confirm that higher OTS loadings

consume more site pairs of MgO-NC, leaving less sites to chemisorb cyclopentanone and

thus reducing activity. Considerably active catalysts with moderate OTS loadings such as

MgO(85)-OTS(15), however, may not be sufficiently hydrophobic and only tolerate

limited water amounts. Once liquid water accumulates, sparsely distributed OTS

molecules hardly prevent site blockage, therefore such catalysts become as susceptible to

water as MgO-NC. From **Figure 30**, it can be stated that functionalizing MgO with little

OTS initially displays remarkable water-induced rate enhancement but eventually

sacrifices the catalytic stability. The water response of MgO(85)-OTS(15) apparently

makes it a transition between MgO(70)-OTS(30) and MgO-NC.

3.3.4. *Effect of the alkyl chain*

The fact in which added water selectively enhances reaction rates over MgO-OTS

catalysts suggests an essential role of the organosilane agent. Such aspect was verified

through the water response of dealkylated MgO(70)-OTS(30) PC. **Figure 31** shows that

MgO(70)-OTS(30) PC behaves similarly to MgO-NC; that is, the catalytic activity drops

rapidly even in water vapor. Such response indicates that MgO(70)-OTS(30) PC is structurally identical to non-functionalized MgO-NC after octadecyl groups are removed during calcination in air at $450^{\circ}C$. One exception is that the surface of MgO(70)-OTS(30) PC remains anchoring SiO_2 fragments, which are originally attached to the strongest basic sites following functionalization. Unlike Si^{4+} cations which are intentionally introduced to basic metal oxides to mitigate catalyst poisoning [213-216], these SiO_2 fragments hardly protect the MgO surface from water and oligomers. Since cyclopentanone molecules still experience diffusion limitation – though much reduced – through such fragments, MgO(70)-OTS(30) PC is less catalytically active than MgO-NC. Should diffusion limitation be negligible, the post-calcined catalyst would display a respectably higher turnover frequency. Meanwhile, the higher activity of MgO(70)-OTS(30) PC with respect to that of MgO(70)-OTS(30) is ascribed to an increase of accessible sites rather than of basic strength. As mentioned in **Section 3.3.1.3**, certain unoccupied medium-strength basic sites – initially hindered by adjacent octadecyl groups – become available for cyclopentanone activation once hydrophobic alkyl chains disappear.
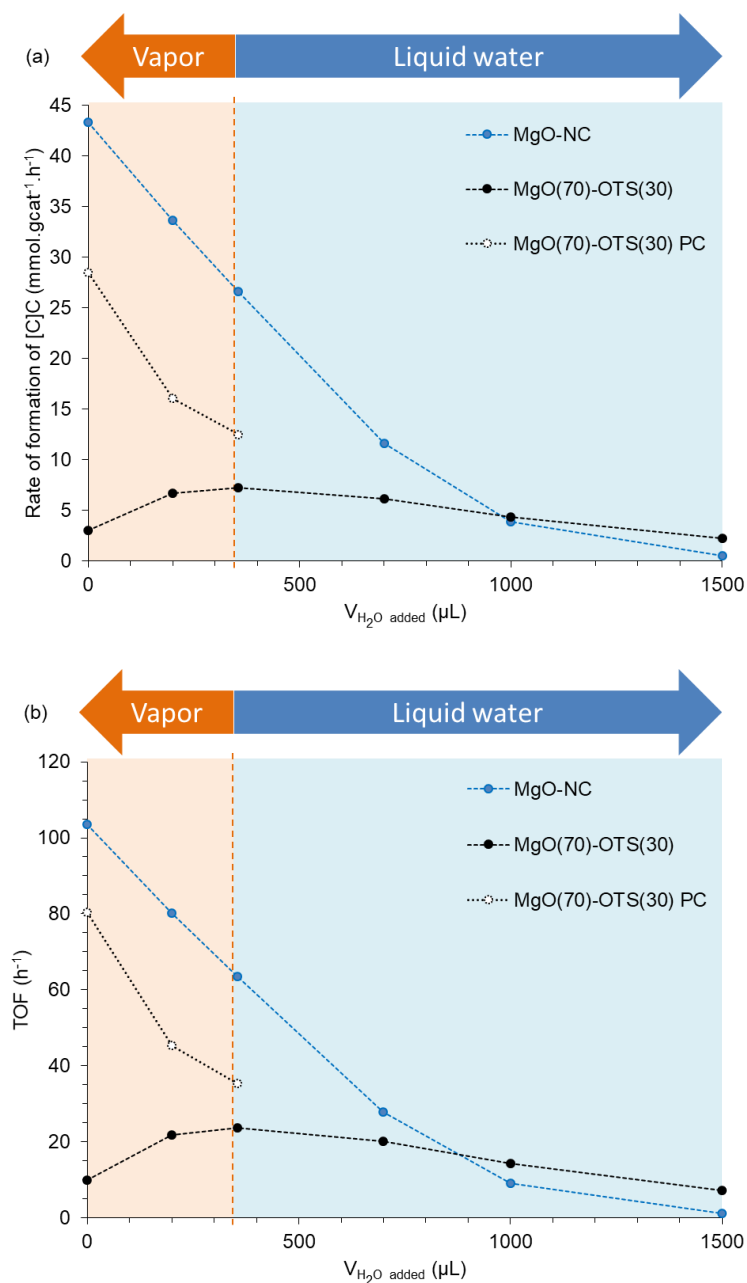
Figure 31. Water response of dealkylated MgO(70)-OTS(30) PC following temperature-programmed calcination at 450°C: (a) Reaction rate, (b) TOF.

Reaction conditions: $C_{cyclopentanone\ 0}$ = 1.8 M, 200°C.

3.3.5. The water-induced catalytic activity of MgO-OTS

3.3.5.1. Reaction order

Analogously to our previous work [70], it is essential to decouple reaction kinetics from catalyst deactivation, particularly through measuring initial rates. First, such measurement helps determine how functionalization with OTS influences the reaction order and the rate-limiting step on an MgO surface. Second, it provides clues on the manner by which external water molecules facilitate cyclopentanone self-aldol condensation.

In practice, initial rates over MgO(70)-OTS(30) and MgO(70)-OTS(30) PC were measured via 1-hour runs at 200ºC, with various initial concentrations of cyclopentanone. Initial rates over MgO-NC, meanwhile, were referred from our previous work [70]. Although MgO-NC was originally tested at 150ºC, its superior intrinsic basicity still resulted in rates comparable to those of MgO(70)-OTS(30) and MgO(70)-OTS(30) PC.

Figure 32a and **Figure 32b** display the initial rate over an MgO-based catalyst as a function of the initial concentration. Apparently, MgO-NC and MgO(70)-OTS(30) PC experience linear rate increases while MgO(70)-OTS(30) exhibits a parabolic rate increase throughout concentrations below 1.0 M. From 1.8 M and beyond, all rate vs. concentration curves start plateauing. Such behaviors suggest that at low concentrations, cyclopentanone self-aldol condensation is first-order on MgO-NC, second-order on MgO(70)-OTS(30) and back to first-order on MgO(70)-OTS(30) PC. At high concentrations, plateaus observed over all three catalysts indicate evident deviations to zeroth-order. One can state up to this

point that functionalizing MgO with OTS not only improves material stability but also changes reaction kinetics.

Among elementary steps of a heterogeneous base-catalyzed nucleophilic addition mechanism, both α-H abstraction [48] and C-C coupling [53] can be rate-limiting. The former step is also referred as deprotonation, enolate formation or α-H activation. The latter step can be either a Langmuir-Hinshelwood-typed bimolecular surface reaction or an Eley-Rideal-typed reaction between an adsorbed enolate and a liquid cyclopentanone molecule [70]. **Appendix H** shows 3 initial rate equations assuming Langmuir-Hinshelwood deprotonation, Langmuir Hinshelwood C-C coupling and Eley-Rideal C-C coupling as rate-limiting steps. At low initial concentrations of cyclopentanone, corresponding reaction orders from such equations are first, second and second. At high initial concentrations of cyclopentanone, these reaction orders deviate to zeroth, zeroth and first respectively. Clearly, **Figure 32b** demonstrates that all data series fit one of the Langmuir-Hinshelwood reaction models rather than the Eley-Rideal one. The latter is only considerable when a rate vs. concentration curve continues increasing linearly at high initial concentrations of cyclopentanone, which is not observed here.
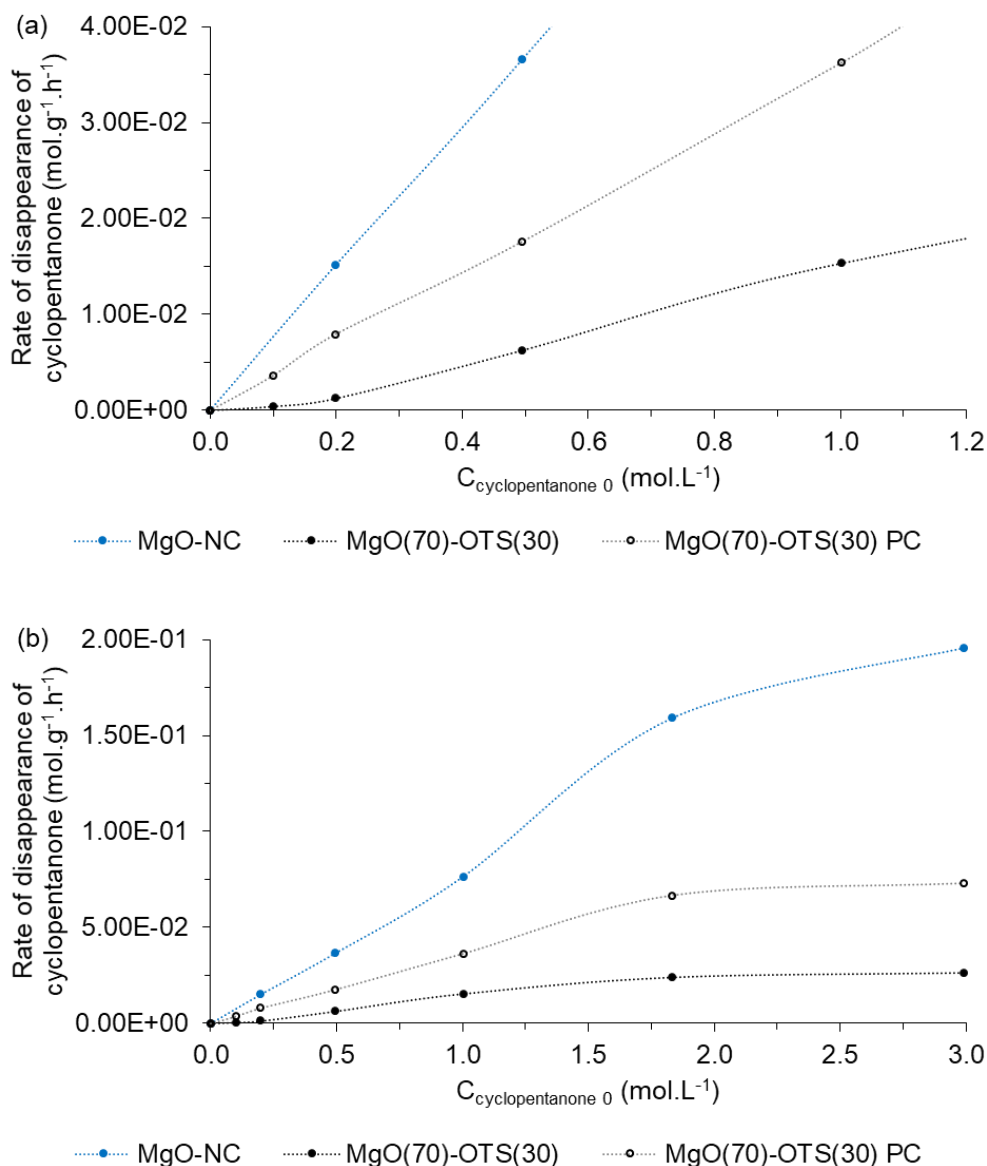
Figure 32. Apparent reaction order for cyclopentanone self-aldol condensation over various MgO-based catalysts from initial rate measurements: (a) $C_{cyclopentanone\ 0}$ from 0.1 M to 1.0 M – shown for clarity, (b) $C_{cyclopentanone\ 0}$ from 0.1 M to 3.0 M.

<u>Reaction conditions:</u> 50 mL of feed; MgO-NC: 0.25 g – 150°C – 20 mins; MgO(70)-OTS(30): 0.50 g – 200°C – 1 hour; MgO(70)-OTS(30) PC: 0.325 g – 200°C – 1 hour.

The rate-limiting step over each MgO-based catalyst was specified by linearizing initial rate equations (**Appendix I**). The model whose linearized function provides the highest coefficient of determination is the most appropriate reaction mechanism. Based on **Figure 32b**, linearization helps distinguish Langmuir-Hinshelwood-typed initial rate equations which assume deprotonation and C-C coupling as rate-limiting steps. Despite being technically ruled out, the Eley-Rideal-typed initial rate equation was also linearized and plotted to compare to Langmuir-Hinshelwood-typed counterparts.

Figure I-1, Figure I-2 and **Figure I-3** (**Appendix I**) show the compatibility of linearized initial rate equations with MgO-NC, MgO(70)-OTS(30) and MgO(70)-OTS(30) PC respectively. For MgO-NC, Langmuir-Hinshelwood deprotonation is the rate-limiting step. MgO(70)-OTS(30) renders Langmuir-Hinshelwood C-C coupling kinetically relevant instead. When alkyl chains of OTS molecules are removed, MgO(70)-OTS(30) PC behaves similarly to MgO-NC; that is, the rate-limiting step is again Langmuir-Hinshelwood deprotonation. Based on changes in reaction order and reaction model, the water effect on MgO-OTS catalysts can be interpreted as a process in which external water molecules facilitate C-C coupling. Such process is addressed in details in **Section 3.3.5.3**.

3.3.5.2. Density Functional Theory simulation of cyclopentanone chemisorption on OTS-

*functionalized MgO**
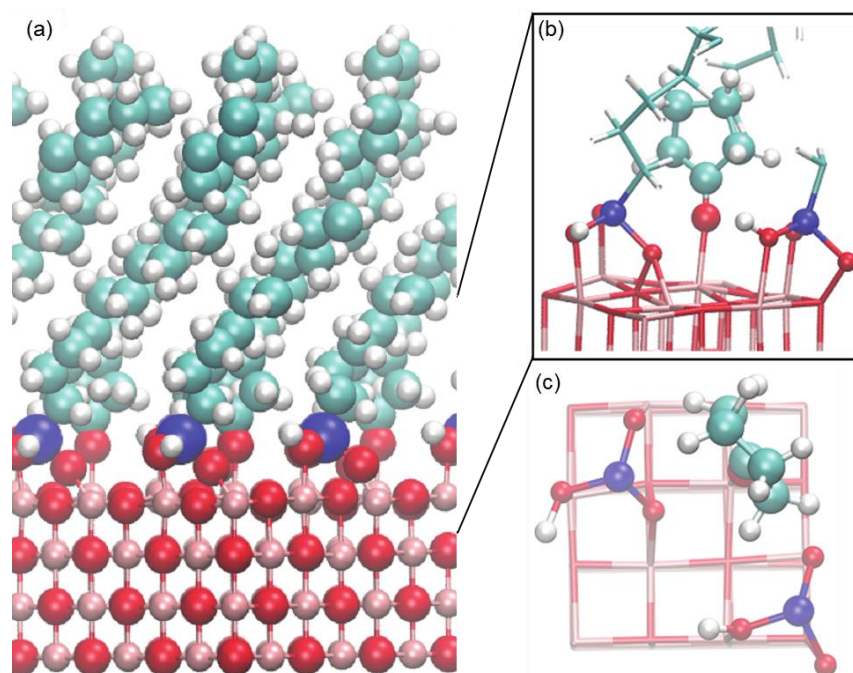
Figure 33. DFT calculation of adsorption of cyclopentanone on OTS-functionalized

MgO.

(a) Atomic structure of the hybrid interface, with Mg, O, Si, C, and H colored pink, red,

blue, cyan, and white, respectively. OTS density is about 3 per nm^2. (b) Side view of the

unit cell to show the adsorption configuration of cyclopentanone at the interface. (c) Top

view of the unit cell. The carbon chain in the OTS has been omitted to show the densely

packed interface.

---

* DFT calculations were conducted by Dr. Bin Wang.

Figure 33 shows the atomic structure of cyclopentanone adsorption at the OTS/MgO interface. *Ab initio* molecular dynamics simulations were performed first to equilibrate the structures of the OTS/MgO over 30 ps at 200 °C, and then a cyclopentanone molecule was introduced using one of the snapshots taken from the AIMD simulations. The OTS was anchored to the MgO surface through Si-O-Mg covalent bonds. In this case, we assumed one silanol still remained per OTS at the interface. **Figure 33c** depicts an adsorbed cyclopentanone molecule along with 2 OTS anchors over an 8 Å x 8 Å unit cell, being equivalent to 3 OTS anchors per nm^2. Because of this high density of OTS on the MgO surface, adsorption of two cyclopentanone molecules in proximity becomes rare. This change of cyclopentanone coverage may have a predominant effect in determining the reaction kinetics.

3.3.5.3. Mechanistic aspects of water-assisted C-C coupling
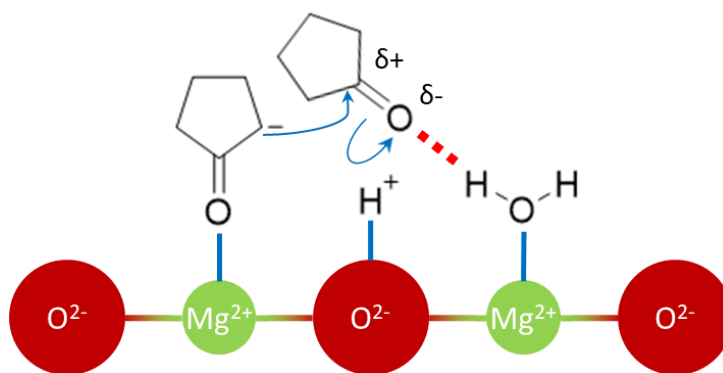
Figure 34. Schematic water-assisted C-C coupling as an elementary step of the nucleophilic addition mechanism of cyclopentanone self-aldol condensation.

To rationalize vastly different water responses of the as-prepared MgO-based catalysts, we first correlate the surface property of each catalyst and the corresponding rate-limiting step. If α-C-H cleavage is kinetically relevant, the overall rate is technically enhanced by the presence of basic sites. The subsequent step – C-C coupling – is very fast due to the availability of Lewis acid – Bronsted base site pairs. That is, C-C coupling is almost pseudo-equilibrated as several surface-bound electrophilic cyclopentanone molecules readily surround a newly-formed enolate. For MgO-NC, the catalyst with the highest basic density and without spatial constraints, it strongly chemisorbs both water and cyclopentanone from the bulk cyclohexane. The absence of hydrophobic alkyl chains allows adsorbed water molecules to extensively occupy Lewis acid sites and form a stable film. Such film becomes a separate phase between Mg^{2+}-O^{2-} and cyclohexane, preventing a sizeable amount of cyclopentanone molecules from being chemisorbed and deprotonated. In other words, the competitive adsorption of water on the MgO-NC surface only inhibits catalytic activity. As shown in **Figure 31**, this negative effect also occurs on dealkylated MgO(70)-OTS(30) PC, whose structure is mostly identical to that of bare MgO-NC.

On the other hand, OTS functionalization on MgO-NC inhibits the C-C coupling step by blocking access of a newly-formed deprotonated cyclopentanone to a neutral cyclopentanone molecule. Although the cyclic ketone can still be chemisorbed and deprotonated on MgO(70)-OTS(30), it is increasingly difficult for the resulting enolate to find adjacent surface-bound cyclopentanone molecules for nucleophilic attack. OTS functionalization also blocks the access of a neutral cyclopentanone molecule to an Mg^{2+} Lewis acid site, a potential enhancer of catalytic activity via polarization of the C=O bond.

As a consequence, C-C coupling replaces deprotonation as the rate-limiting step on MgO(70)-OTS(30). Removal of bulky octadecyl groups essentially eliminates spatial constraints for cyclopentanone chemisorption, therefore cyclopentenolate regains the chance to target adjacent surface-bound electrophiles. The energy barrier for C-C coupling over dealkylated MgO(70)-OTS(30) PC will be again lower than that of deprotonation.

Next, we analyze how water addition influences the rate-limiting C-C coupling on MgO(70)-OTS(30). Particularly, the anionic α-C of a deprotonated cyclopentanone targets the carbonyl C of a neutral cyclopentanone molecule to form a new C-C bond. The more polar the neutral cyclopentanone C=O bond is, the more electropositive the carbonyl C becomes to accelerate the nucleophilic attack of the α-C. In Langmuir-Hinshelwood model, the extent of C=O polarization depends on the bond strength between the carbonyl O and a lattice Mg^{2+}. This Mg^{2+} is technically one of the sites adjacent to the cyclopentenolate-occupied Mg^{2+}. As earlier mentioned, MgO(70)-OTS(30) renders C-C coupling kinetically relevant due to the high density of long alkyl chains which tremendously reduces accessible Mg^{2+} sites for neutral cyclopentanone molecules. In other words, the steric hindrance of OTS prevents a sizeable amount of cyclopentanone from associative chemisorption. Under this circumstance, the electrophilic carbonyl C mainly interacts with an adsorbed cyclopentenolate while staying in the organic solvent. Such interaction resembles the Eley-Rideal model; however, C-C coupling is slowed down since the neutral cyclopentanone C=O bond is not sufficiently polar. This issue can be alleviated by surface-bound water species adjacent to a cyclopentenolate. At low contents, a single water molecule is attached to an Mg^{2+} Lewis acid site and functions as a nucleating seed.

92

As more water enters the system, the next molecules hydrogen-bond such seeds and generate a water cluster rather than a surface-covering film. As illustrated in **Figure 34**, external water can provide one of its H atoms to hydrogen-bond the carbonyl O of the liquid cyclopentanone. Such bonding mode polarizes the C=O bond by shifting the electron density to the carbonyl O, rendering the carbonyl C sufficiently electropositive to interact with the anionic α-C. From this perspective, water apparently shuttles liquid cyclopentanone molecules to accelerate the rate-limiting C-C coupling. In other words, liquid cyclopentanone is not required to accommodate Lewis acid sites, which have already been depopulated and hindered by the high OTS loading. Instead, it is indirectly chemisorbed by Mg^{2+} through the water cluster bridge. As seen in **Figure 35** and **Figure I-4** (**Appendix I**), C-C coupling remains rate-limiting following water addition but its energy barrier has been considerably reduced (around 7 kJ.mol^{-1} downhill). The as-described water-induced rate enhancement holds until water clusters are over-expanded. At this point, polarization of the C=O bond is again negligible, therefore excess water no longer promotes the catalytic activity.
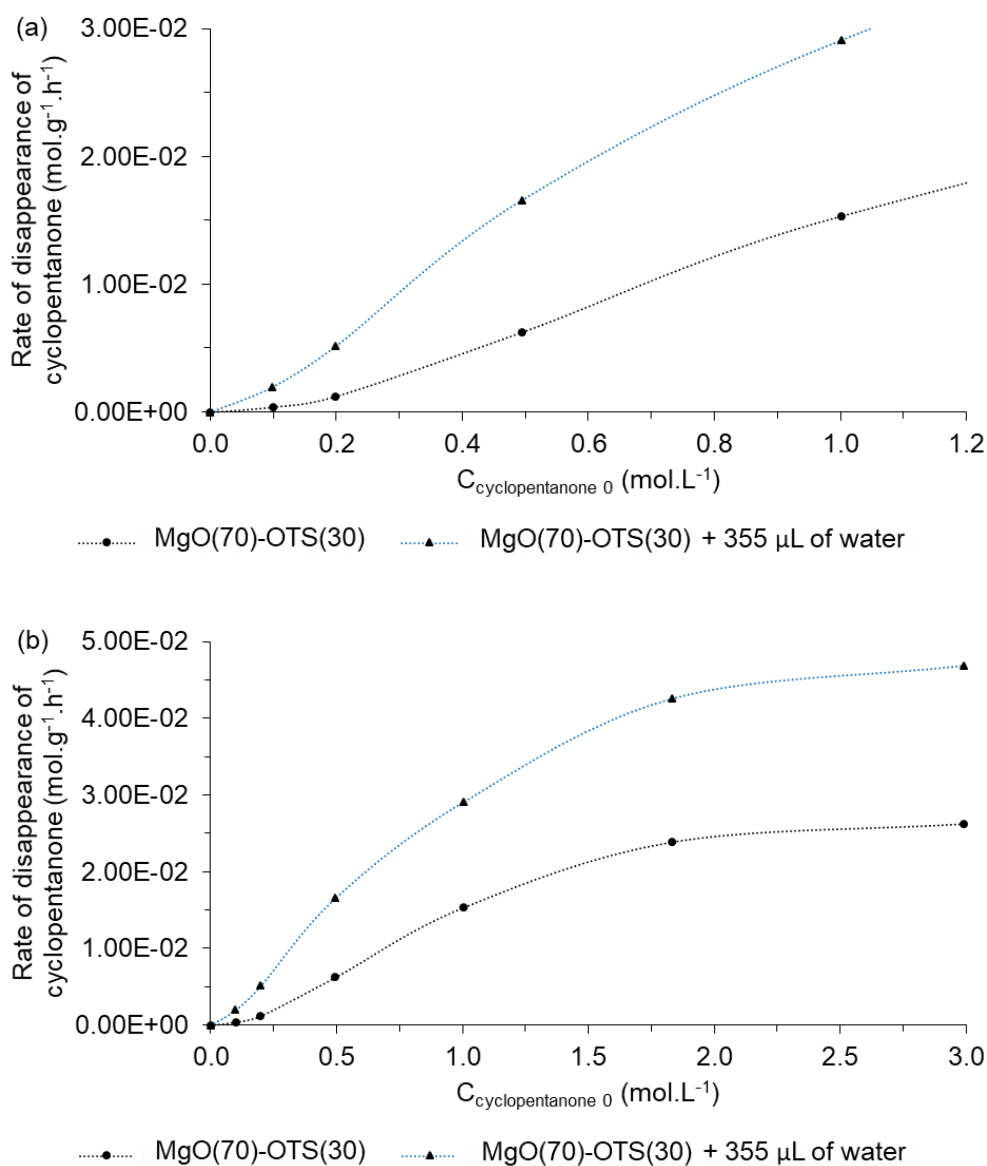
Figure 35. Apparent reaction order for water-induced cyclopentanone self-aldol condensation over MgO(70)-OTS(30) from initial rate measurements: (a) $C_{cyclopentanone\ 0}$ from 0.1 M to 1.0 M – shown for clarity, (b) $C_{cyclopentanone\ 0}$ from 0.1 M to 3.0 M. Reaction conditions: 50 mL of feed; MgO-NC: 0.25 g – 150°C – 20 mins; MgO(70)-OTS(30): 0.50 g – 200°C – 1 hour; MgO(70)-OTS(30) PC: 0.325 g – 200°C – 1 hour.

3.3.6. Kinetic isotope effect
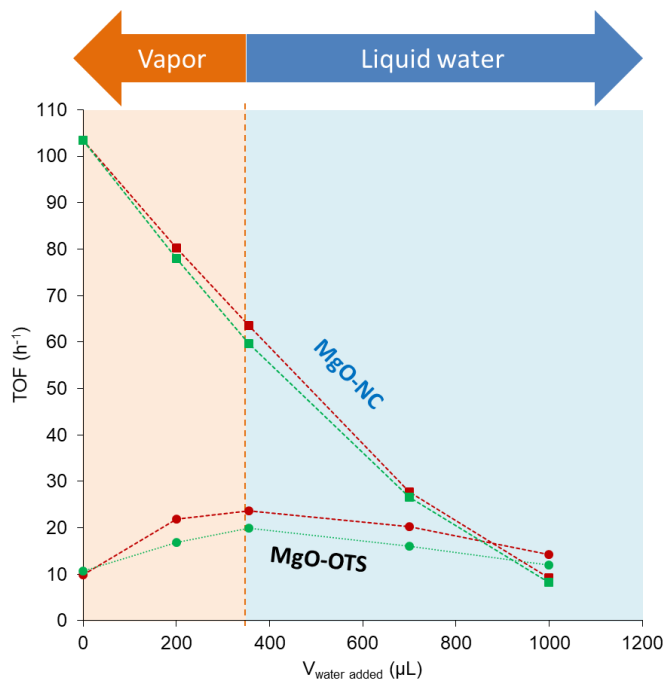
Figure 36. D_2O/H_2O kinetic isotope effect on cyclopentanone self-aldol condensation.

Red symbols – H_2O addition. Green symbols – D_2O addition.

Reaction conditions: $C_{cyclopentanone\ 0}$ = 1.8 M, 200°C.

Figure 36 displays changes in reaction rates when D_2O is added to the system instead of H_2O. A small, but consistent, kinetic isotope effect is observed on OTS-functionalized MgO but not on bare MgO-NC. As mentioned in **Section 3.3.5.3**, the rate-limiting step on the former is C-C coupling, which can be positively affected by water. As H_2O molecules are more mobile than D_2O counterparts, a surface-bound H_2O cluster may interact with a liquid cyclopentanone molecule more readily. The hydrogen bond between

these species therefore can be strengthened, resulting in a more stable cyclopentanone…H_2O intermediate and a more electropositive carbonyl C. Meanwhile, on MgO-NC, the rate-limiting step is deprotonation, which has been shown negatively affected by water. The only role of water here is blocking sites, in that sense H_2O and D_2O are comparable inhibitors.

3.4. Summary

The main conclusions of the study are the following:

i.   Functionalizing MgO with octadecyltrichlorosilane (OTS) changes the rate-limiting step of cyclopentanone self-aldol condensation from first-ordered α-H abstraction to second-ordered C-C coupling. This is because high areal densities of OTS not only depopulate accessible Mg^{2+} sites for cyclopentanone but also render its chemisorption path more tortuous. Such scenario significantly increases the energy barrier of the bimolecular surface reaction between a cyclopentenolate and a cyclopentanone electrophile.

ii.   The dramatically decreased catalytic activity of MgO-OTS with respect to that of MgO-NC can be partially recovered by adding moderate amounts of water to the reaction system. The promotional effect of external water only applies when octadecyl groups are attached to the MgO surface via Si-O-Mg covalent bonds.

iii.   For MgO-OTS catalysts, external water assists the rate-limiting C-C coupling by polarizing the C=O bond of a liquid cyclopentanone molecule through hydrogen-bonding. A surface-bound water cluster is proposed to bridge the liquid cyclopentanone molecule to an Mg^{2+} acid site in proximity to the cyclopentenolate. In other words, cyclopentanone from the bulk organic solvent is indirectly attached to Mg^{2+} and thus exempted from the tortuous chemisorption path caused by surface silanization. Hydrogen-bonding with a water cluster improves the electrophilicity of a liquid cyclopentanone molecule, thus mitigating the energy barrier of aldolate formation.

4. Conclusions and Future directions

Cyclopentanone, obtained from the aqueous-phase selective hydrogenation of furfural, is an important building block in biomass upgrading processes. It undergoes various aldol condensations to produce α,β-unsaturated ketones which are potentially hydrodeoxygenated into biofuels. MgO-based solids are among basic catalysts commonly used to catalyze these aldol condensations. MgO-NC, prepared through nitrate-citrate combustion, has a dramatically improved surface area with respect to that of commercial MgO. Despite a noticeably high activity over cyclopentanone self-aldol condensation, hydrophilic MgO-NC is rapidly deactivated due to site blockage of water and oligomeric products. This issue has been solved by surface hydrophobization with octadecyltrichlorosilane (OTS), on either an MgO-NC substrate (MgO-OTS) or an MgO-mesoporous silica fusion (MgO@mSiO$_2$-OTS). The inevitable decrease in catalytic activity following such modification is well compensated by the tremendously enhanced tolerance to poisoning agents. The hydrophobic carbon chains of OTS molecules prevent water from agglomerating on the MgO surface, forming a layer which reduces accessible active sites for cyclopentanone. These carbon chains also help desorb *in situ* water and C$_{10+}$ species, therefore a hybrid MgO retains the activity for considerably long times and can be reused for multiple cycles. Such advantages not only highlight silanization as a feasible approach to enhance the stability of MgO but also pave ways for additional research to benefit from industrial scales.

Analogous to cyclopentanone self-aldol condensation, cyclopentanone-acetone cross-aldol condensation is also a promising route to obtain biofuels. Under the catalysis of MgO-NC, calculations on an equimolar reactant mixture show that cyclopentanone is not only more strongly chemisorbed but also more acidic than acetone. It has been found that the products are predominantly cyclopentanone-activated dimers, particularly 2-cyclopentylidenecyclopentanone and 2-isopropylidenecyclopentanone. As more acetone is introduced with respect to a fixed amount of cyclopentanone, the total rate of formation of acetone-activated dimers increases proportionally but that of cyclopentanone-activated dimers holds. This feature along with DFT suggest that the cross-aldol condensation is limited by the α-H abstraction of a ketone reactant. Nevertheless, the product distribution is alternatively controlled by the C-C coupling between an adsorbed cyclopentenolate and an electrophilic acetone/cyclopentanone. It is shown that the cross-to-self product ratio depends on liquid concentrations of the reactants, their populations in proximity to cyclopentenolate species and enolate-electrophile interactions.

Unlike oligomeric residues, water can promote some catalytic activity on cyclopentanone self-aldol condensation. For MgO-OTS catalysts, increasing amounts of water shape the rate trend to a volcano plot rather than a straight decline as seen on MgO-NC. It is found that OTS molecules play an important role on such catalytic behavior. Depositing OTS on MgO greatly reduces accessible active sites for cyclopentanone and associates with steric hindrance, therefore the nucleophilic attack of cyclopentenolate to an adjacent electrophile becomes increasingly difficult. In this scenario, C-C coupling replaces α-H abstraction as the rate-limiting step. On MgO-OTS catalysts, external water

molecules tend to form clusters rather than a permanent diffusion-limiting film. Through hydrogen-bonding, each cluster connects a cyclopentanone molecule from the bulk organic solvent to a lattice Mg^{2+}, resembling a Langmuir-Hinshelwood-typed reaction model. The hydrogen bond helps polarize the C=O bond of the liquid cyclopentanone, rendering its carbonyl C sufficiently electrophilic for the rate-limiting C-C coupling. By this manner, water partially recovers the catalytic activity of MgO-OTS, which has been limited with respect to that of MgO-NC following surface silanization. This finding along with the appreciable material stability bolster the ambition of OTS functionalization to optimize catalytic performances of MgO in other relevant organic syntheses.

For better insights on both cyclopentanone aldol condensation and MgO-based catalysts, the following works are recommended:

- MgO@mSiO$_2$-OTS is combined with a metal catalyst (e.g. 3%Pd/α-Al$_2$O$_3$) in a biphasic system for a direct transformation of water-soluble furfural into oil-soluble 2-cyclopentylidenecyclopentanone.

- MgO-OTS catalysts are also studied for water responses in cyclopentanone-acetone cross-aldol condensation. Apart from reaction rates with possible maxima, it is also important to learn how external water alters the product distribution, particularly trimer-to-dimer molar ratios and yields of cyclopentanone-activated dimers.

5. References

[1]   T. N. Pham, D. Shi, D. E. Resasco, Appl. Catal., B 145 (2014), 10-23.

[2]   J. A. Herron, T. S. Vann, N. N. Duong, D. E. Resasco, S. P. Crossley, L. L. Lobban, C. T. Maravelias, Energy Technology 5(1) (2017), 130-150.

[3]   D. E. Resasco, S. P. Crossley, Catal. Today 257 (2015), 185-199.

[4]   N. N. Duong, B. Wang, T. Sooknoi, S. P. Crossley, D. E. Resasco, ChemSusChem 10(13) (2017), 2823-2832.

[5]   N. N. Duong, Q. Tan, D. E. Resasco, Comptes Rendus Chimie 21(3-4) (2018), 155-163.

[6]   L. Ivanhoe, World Oil 216(10) (1995), 77-88.

[7]   A. Bartlett, Math. Geosci. 32 (1) (2000), 1-17.

[8]   H. Gluskoter, Increase in fossil fuel utilization in the twenty-first century: Environmental impact and lower carbon alternatives: Division of Fuel Chemistry of the American Chemical Society, Preprints, 44(1) (1999), 36-41.

[9]   G. Herbert, A. Krishnan, Renew. & Sustainable Energy Rev. 59 (2016), 292-308.

[10]   S. Czernik, A. V. Bridgwater, Energy Fuels 18 (2004), 590-598.

[11]   D. Mohan, C. U. Pittman, Jr., P. H. Steele, Energy Fuels 20 (2006), 848-889.

[12]   P. A. Zapata, J. Faria, M. Pilar Ruiz, D. E. Resasco, Top. Catal. 55 (2012), 38-52.

[13]   G. Huber, S. Iborra, A. Corma, Chem. Rev. 106 (2006), 4044-4098.

[14]   D. Alonso, J. Bond, J. Dumesic, Green Chem. 12 (2010), 1493-1513.

[15] M. Hronec, K. Fulajtarova, Catal. Commun. 24 (2012), 100-104.

[16] M. Hronec, K. Fulajtarova, T. Liptaj, M. Stolcova, N. Pronayova, T. Sotak, Biomass and Bioenergy 63 (2014), 291-299.

[17] C. Cai, T. Zhang, R. Kumar, C. Wyman, J. Chem. Technol. Biotechnol. 89(1) (2014), 2-10.

[18] Y. Yang, Z. Du, Y. Huang, F. Lu, F. Wang, J. Gao, J. Xu, Green Chem. 15 (2013), 1932-1940.

[19] J. Guo, G. Xu, Z. Han, Y. Zhang, Y. Fu, Q. Guo, ACS Sustainable Chem. Eng. 2(10) (2014), 2259-2266.

[20] M. Demirbas, Energy Sources, Part A 28 (2006), 1181-1188.

[21] T. N. Pham, T. Sooknoi, S. P. Crossley, D. E. Resasco, ACS Catal. 3(11) (2013), 2456-2473.

[22] M. H. Gollis, L. I. Belenyessy, B. J. Gudzinowicz, S. D. Koch, J. O. Smith, R. J. Wineman, J. Chem. Eng. Data 7 (1962), 311-316.

[23] G. Macala, T. Matson, C. Johnson, R. Lewis, A. Iretskii, P. Ford, ChemSusChem 2 (2009), 215-217.

[24] W. Shen, G. A. Tompsett, K. D. Hammond, R. Xing, F. Dogan, C. P. Grey, W. C. Conner, S. M. Auerbach, G. W. Huber, Appl. Catal., A 392 (2011), 57-68.

[25] J. Yang, N. Li, G. Li, W. Wang, A. Wang, X. Wang, Y. Cong, T. Zhang, Chem. Commun. 50 (2014), 2572-2574.

[26] D. Liang, G. Li, Y. Liu, J. Wu, X. Zhang, Catal. Commun. 81 (2016), 33-36.

[27] J. Cueto, L. Faba, E. Diaz, S. Ordonez, ChemCatChem 9 (2017), 1765-1770.

[28] J. Yang, S. Li, N. Li, W. Wang, A. Wang, T. Zhang, Y. Cong, X. Wang, G. W. Huber, Ind. Eng. Chem. Res. 54 (2015), 11825-11837.

[29] R. Y. Levina, V. R. Skvarchenko, O. Y. Okhlobystin, Zh. Obshch. Khim. 25 (1955), 1466-1469.

[30] M. B. Turovapolyak, I. E. Sosnina, E. G. Treshchova, Zh. Obshch. Khim. 23 (1953), 1111-1116.

[31] H. Kurokawa, T. Kato, T. Kuwabara, W. Ueda, Y. Morikawa, Y. Moro-oka, T. Ikawa, J. Catal. 126 (1990), 208-218.

[32] R. West, Z. Liu, M. Peter, C. Gartner, J. Dumesic, J. Mol. Catal. A: Chem. 296 (2008), 18-27.

[33] G. Solomons, C. Fryhle, in: Organic Chemistry, 7th Edition, Wiley, New York City, 1999, p. 1264.

[34] M. Hasni, G. Prado, J. Rouchaud, P. Grange, M. Devillers, S. Delsarte, J. Mol. Catal. A: Chem. 247 (2006), 116-123.

[35] J. I. Di Cosimo, V. K. Diez, C. Ferretti, C. R. Apesteguia, RSC Catal. 26 (2014), 1-28.

[36] V. Chesnokov, A. Bedilo, D. Heroux, I. Mishakov, K. Klabunde, J. Catal. 218 (2003), 438-446.

[37] C. Perego, P. Villa, Catal. Today 34 (1997), 281-305.

[38] A. Saberi, F. Golestani-Fard, H. Sarpoolaky, M. Willert-Porada, T. Gerdes, R. Simon, J. Alloys Compd. 462 (1-2) (2008), 142-146.

[39] P. A. Zapata, J. Faria, M. Pilar Ruiz, R. E. Jentoft, D. E. Resasco, J. Am. Chem. Soc. 134 (2012), 8570-8578.

[40] M. Hronec, K. Fulajtarova, T. Liptaj, Appl. Catal., A 437-438 (2012), 104-111.

[41] A. Merzhanov, I. Borovinskaya, V. Yukhvid, V. Ratnikov, in: Scientific Principles of Material Science, Nauka, Moscow, 1981, p. 193.

[42] A. Varma, A. Rogachev, A. Mukasyan, S. Hwang, Adv. Chem. Eng. 24 (1998), 79-226.

[43] H. Pan, X. Wang, S. Xiao, L. Yu, Zh. Zhang, Indian J. Eng. Mater. Sci. 20 (2013), 561-567.

[44] T. Jesionowski, Pigm. Resin Technol. 30 (2001), 287-295.

[45] Z. Bo, T. R. Eaton, J. R. Gallagher, C. P. Canlas, J. T. Miller, J. M. Notestein, Chem. Mater. 27(4) (2015), 1269-1277.

[46] T. N. Pham, L. Zhang, D. Shi, M. R. Komarneni, M. P. Ruiz, D. E. Resasco, J. Faria, ChemCatChem 8 (2016), 3611-3620.

[47] S. Sitthisa, T. Sooknoi, Y. Ma, P. Balbuena, D. E. Resasco, J. Catal. 277 (2011), 1-13.

[48] S. Wang, K. Goulas, E. Iglesia, J. Catal. 340 (2016), 302-320.

[49] S. Herrmann, E. Iglesia, J. Catal. 346 (2017), 134-153.

[50] V. K. Diez, C. R. Apesteguia, J. I. Di Cosimo, J. Catal. 240 (2006), 235-244.

[51] J. Zelin, A. F. Trasarti, C. R. Apesteguia, Catal. Commun. 42 (2013), 84-88.

[52] Z. Young, S. Hanspal, R. Davis, ACS Catal. 6 (2016), 3193-3202.

[53]   S. Shylesh, D. Kim, A. Gokhale, C. Canlas, J. Struppe, C. Ho, D. Jadhav, A. Yeh, A. Bell, Ind. Eng. Chem. Res. 55 (2016), 10635-10644.

[54]   K. Goulas, G. Gunbas, P. Dietrich, S. Sreekumar, A. Grippo, J. Chen, A. Gokhale, F. Toste, ChemCatChem 9 (2017), 677-684.

[55]   S. P. Crossley, J. Faria, M. Shen, D. E. Resasco, Science 327 (2010), 68-72.

[56]   T. Dossin, F. Reyniers, G. Marin, Appl. Catal., B 61 (2006), 35-45.

[57]   G. Salvapati, K. Ramanamurty, M. Janardanarao, J. Mol. Catal. 54 (1989), 9-30.

[58]   P. Kustrowski, D. Sulkowska, R. Pytlowany, R. Dziembaj, React. Kinet. Catal. Lett. 81(1) (2004), 3-11.

[59]   S. Lippert, W. Baumann, K. Thomke, J. Mol. Catal. 69 (1991), 199-214.

[60]   J. Di Cosimo, V. Diez, C. Apesteguia, Appl. Catal. A 137 (1996), 149-166.

[61]   G. G. Podrebarac, F. T. T. Ng, G. L. Rempel, Chem. Eng. Sci. 52(17) (1997), 2991-3002.

[62]   S. Wang, E. Iglesia, J. Phys. Chem. C 120 (2016), 21589-21616.

[63]   V. Diez, J. Di Cosimo, C. Apesteguia, Appl. Catal. A 345 (2008), 143-151.

[64]   J. Guthrie, X. Wang, Can. J. Chem. 70 (1992), 1055-1068.

[65]   S. Abello, S. Dhir, G. Colet, J. Perez-Ramirez, Appl. Catal. A 325 (2007), 121-129.

[66]   C. Noda Perez, C. Henriques, O. Antunes, J. Monteiro, J. Mol. Catal. A: Chem. 233 (2005), 83-90.

[67]   E. Jablonski, I. Vilella, S. Maina, S. de Miguel, O. Scelza, Catal. Commun. 7 (2006), 18-23.

[68]   E. Sacia, M. Balakrishnan, M. Deaner, K. Goulas, F. Toste, A. Bell, ChemSusChem 8 (2015), 1726-1736.

[69]   J. Xu, Y. Cao, Q. Ma, X. Peng, Asian J. Chem. 25(7) (2013), 3847-3849.

[70]   D. T. Ngo, T. Sooknoi, D. E. Resasco, Appl. Catal., B 237 (2018), 835-843.

[71]   R. W. Nagorski, ACS Petroleum Research Fund: 52nd Annual Report on Research, 41360-B4 (2007), 7951.

[72]   G. Naray-Szabo, A. Warshel, in: Computational Approaches to Biochemical Reactivity, Springer Science & Business Media, New York City, 2006, p. 346.

[73]   H. Fan, Y. Yang, J. Song, G. Ding, C. Wu, G. Yang, B. Han, Green Chem. 16 (2014), 600-604.

[74]   S. Wang, E. Iglesia, J. Am. Chem. Soc. 140 (2018), 775-782.

[75]   T. N. Pham, D. Shi, D. E. Resasco, J. Catal. 314 (2014), 149-158.

[76]   M. Hronec, K. Fulajtarova, I. Vavra, T. Sotak, E. Dobrocka, M. Micusik, Appl. Catal., B 181 (2016), 210-219.

[77]   W. Wang, X. Ji, H. Ge, Z. Li, G. Tian, X. Shao, Q. Zhang, RSC Adv. 7 (2017), 16901-16907.

[78]   D. Fan, X. Dong, Y. Yu, M. Zhang, Phys. Chem. Chem. Phys. 19 (2017), 25671-25682.

[79]   R. J. Buszek, J. S. Francisco, J. M. Anglada, Int. Rev. Phys. Chem. 30 (2011), 335-369.

[80]   G. M. Mullen, J. Gong, T. Yan, M. Pan, C. B. Mullins, Top. Catal. 56 (2013), 1499-1511.

[81]   N. Akiya, P. E. Savage, Chem. Rev. 102 (2002), 2725-2750.

[82]   C. Chang, Y. Zhao, B. Long, Z. Huang, J. Li, Sci. Sin. Chim. 46 (2016), 1-11.

[83]   R. N. Butler, A. G. Coyne, Chem. Rev. 110 (2010), 6302-6337.

[84]   M. Date, M. Haruta, J. Catal. 201 (2001), 221-224.

[85]   J. Huang, T. Akita, J. Faye, T. Fujitani, T. Takei, M. Haruta, Angew. Chem. Int. Ed. 48 (2009), 7862-7866.

[86]   J. Staszak-Jirkovsky, R. Subbaraman, D. Strmcnik, K. L. Harrison, C. E. Diesendruck, R. Assary, O. Frank, L. Kobr, G. K. H. Wiberg, B. Genorio, ACS Catal. 5 (2015), 6600-6607.

[87]   Y. Yang, C. A. Mims, R. S. Disselkamp, J. H. Kwak, C. H. F. Peden, C. T. Campbell, J. Phys. Chem. C 114 (2010), 17205-17211.

[88]   E. Voehringer-Martinez, B. Hansmann, H. Hernandez, J. S. Francisco, J. Troe, B. Abel, Science 315 (2007), 497-501.

[89]   B. Long, W. Zhang, X. Tan, Z. Long, Y. Wang, D. Ren, J. Phys. Chem. A 115 (2011), 1350-1357.

[90]   J. Gonzalez, J. M. Anglada, J. Phys. Chem. A 114 (2010), 9151-9162.

[91]   Y. Wang, H. Chen, M. Makino, Y. Shiro, S. Nagano, S. Asamizu, H. Onaka, S. Shaik, J. Am. Chem. Soc. 131 (2009), 6748-6762.

[92]   N. Akiya, P. E. Savage, AIChE J. 44(1998), 405-415.

[93]   V. V. Ordomsky, A. Y. Khodakov, B. Legras, C. Lancelot, Catal. Sci. Technol. 4 (2014), 2896-2899.

[94]   M. Faheem, A. Heyden, J. Chem. Theory Comput. 10 (2014), 3354-3368.

[95]   Q. Wang, H. Fan, S. Wu, Z. Zhang, P. Zhang, B. Han, Green Chem. 14 (2012), 1152-1158.

[96]   J. Jae, G. A. Tompsett, A. J. Foster, K. D. Hammond, S. M. Auerbach, R. F. Lobo, G. W. Huber, J. Catal. 279 (2011), 257-268.

[97]   S. Caratzoulas, M. E. Davis, R. J. Gorte, R. Gounder, R. F. Lobo, V. Nikolakis, S. I. Sandler, M. A. Snyder, M. Tsapatsis, D. G. Vlachos, J. Phys. Chem. C 118 (2014), 22815-22833.

[98]   B. Valle, A. Gayubo, A. Aguayo, M. Olazar, J. Bilbao, Energy Fuels 24 (2010), 2060-2070.

[99]   Y. Cheng, J. Jae, J. Shi, W. Fan, G. W. Huber, Angew. Chem. Int. Ed. 51 (2012), 1387-1390.

[100]   A. Ausavasukhi, Y. Huang, A. T. To, T. Sooknoi, D. E. Resasco, J. Catal. 290 (2012), 90-100.

[101]   C. Chang, Z. Huang, J. Li, WIREs Comput. Mol. Sci. 6 (2016), 679-693.

[102]   Z. Zhao, S. Xu, M. Hu, X. Bao, C. H. F. Peden, J. Hu, J. Phys. Chem. C 119 (2015), 1410-1417.

[103]   F. Fischer, H. Tropsch, Brennst. Chem. 4 (1923), 276-285.

[104]   S. D. Summerford, U.S. Patent 2,497,964 (1950).

[105]   A. K. Dalai, B. H. Davis, Appl. Catal., A 348 (1) (2008), 1-15.

[106]   S. Storsaeter, O. Borg, E. A. Blekkan, A. Holmen, J. Catal. 231 (2005), 405-419.

[107]   A. M. Hilmen, D. Schanke, K. F. Hanssen, A. Holmen, Appl. Catal., A 186 (1999), 169-188.

[108] A. Y. Khodakov, W. Chu, P. Fongarland, Chem. Rev. 107 (2007), 1692-1744.

[109] E. van Steen, H. Schulz, Appl. Catal., A 186 (1999), 309-320.

[110] E. A. Blekkan, O. Borg, V. Froseth, A. Holmen, Catal., Royal Soc. Chem. 20 (2007), 13-32.

[111] A. M. Hilmen, O. A. Lindvag, E. Bergene, D. Schanke, S. Eri, A. Holmen, Stud. Surf. Sci. Catal. 136 (2001), 295-300.

[112] E. Rytter, N. E. Tsakoumis, A. Holmen, Catal. Today 261 (2016), 3-16.

[113] S. Krishnamoorthy, M. Tu, M. P. Ojeda, D. Pinna, E. Iglesia, J. Catal. 211 (2002), 422-423.

[114] C. J. Bertole, C. A. Mims, G. Kiss, J. Catal. 221 (2004), 191-203.

[115] N. Fischer, B. Clapham, T. Feltes, M. Claeys, ACS Catal. 5 (2015), 113-121.

[116] D. D. Hibbitts, B. T. Loveless, M. Neurock, E. Iglesia, Angew. Chem. Int. Ed. 52 (2013), 12273-12278.

[117] C. Aaserud, A. M. Hilmen, E. Bergene, S. Eri, D. Schanke, A. Holmen, Catal. Lett. 94 (2004), 171-176.

[118] B. C. Enger, A. L. Fossan, O. Borg, E. Rytter, A. Holmen, J. Catal. 284 (2011), 9-22.

[119] E. Rytter, T. H. Skagseth, S. Eri, A. O. Sjastad, Ind. Eng. Chem. Res. 49 (2010), 4140-4148.

[120] C. J. Bertole, G. Kiss, C. A. Mims, J. Catal. 223 (2004), 309-318.

[121] M. Ojeda, R. Nabar, A. U. Nilekar, A. Ishikawa, M. Mavrikakis, E. Iglesia, J. Catal. 272 (2) (2010), 287-297.

[122] C. Huo, J. Ren, Y. Li, J. Wang, H. Jiao, J. Catal. 249 (2) (2007), 174-184.

[123] C. Huo, Y. Li, J. Wang, H. Jiao, J. Phys. Chem. C 112 (2008), 14108-14116.

[124] S. Chin, C. T. Williams, M. D. Amiridis, J. Phys. Chem. B 110 (2006), 871-882.

[125] C. J. Kim, Eur. Pat. Appls. 339,923 (1988) and 355,218 (1990), assigned to Exxon.

[126] H. Schulz, E. van Steen, M. Claeys, in: H. E. Curry-Hyde, R. E. Howe (Eds.), Natural Gas Conversion II, Elsevier, Amsterdam, 1994, p. 455.

[127] C. J. Kim, U.S. Patent 5,227,407 (1993), assigned to Exxon. Res. Eng. Co.

[128] E. Iglesia, Appl. Catal., A 161 (1997), 59-78.

[129] H. Schulz, E. van Steen, M. Claeys, Stud. Surf. Sci. Catal. 81 (1994), 455-460.

[130] H. Schulz, M. Claeys, S. Harms, Stud. Surf. Sci. Catal. 107 (1997), 193-200.

[131] Eur. Patent Appls. 201,557 (1983), assigned to Shell.

[132] M. Rothaemel, K. F. Hanssen, E. A. Blekkan, D. Schanke, A. Holmen, Catal. Today 38 (1997), 79-84.

[133] M. Claeys, E. van Steen, Catal. Today 71 (2002), 419-427.

[134] C. J. Bertole, C. A. Mims, G. Kiss, J. Catal. 210 (2002), 84-96.

[135] C. J. Kim, U.S. Patent 0,355,216 (1993).

[136] T. K. Das, W. A. Conner, G. Jacobs, J. Li, K. Chaudhari, B. H. Davis, Proceedings of the 7th Natural Gas Conference, Dalian, China (2004), Elsevier, Amsterdam, p. 331.

[137] N. Kizhakevariam, X. Jiang, M. Weaver, J. Chem. Phys. 100 (1994), 6750-6764.

[138] T. Yuzawa, T. Higashi, J. Kubota, J. N. Kondo, K. Domen, C. Hirose, Surf. Sci. 325 (1995), 223-229.

[139] M. Nakamura, M. Ito, Chem. Phys. Lett. 335 (2001), 170-175.

[140] E. Iglesia, S. L. Soled, R. A. Fiato, J. Catal. 137 (1992), 212-224.

[141] D. Shi, J. Faria, T. N. Pham, D. E. Resasco, ACS Catal. 4 (2014), 1944-1952.

[142] L. R. Merte, G. Peng, R. Bechstein, F. Rieboldt, C. A. Farberow, L. C. Grabow, W. Kudernatsch, S. Wendt, E. Laegsgaard, M. Mavrikakis, Science 336 (2012), 889-893.

[143] M. B. Boucher, M. D. Marcinkowski, M. L. Liriano, C. J. Murphy, E. A. Lewis, A. D. Jewell, M. F. G. Mattera, G. Kyriakou, M. Flytzani-Stephanopoulos, E. C. H. Sykes, ACS Nano 7 (2013), 6181-6187.

[144] Y. Zhao, Y. Yang, C. Mims, C. H. F. Peden, J. Li, D. Mei, J. Catal. 281 (2011), 199-211.

[145] C. Xiao, Z. Cai, T. Wang, Y. Kou, N. Yan, Angew. Chem., Int. Ed. 47 (2008), 746-749.

[146] E. Iglesia, S. C. Reyes, R. J. Madon, S. L. Soled, Adv. Catal. 39 (1993), 221-302.

[147] R. C. Reid, J. M. Prausnitz, T. K. Sherwood, in: The Properties of Gases and Liquids, McGraw-Hill, New York, 1977.

[148] R. S. Albal, Y. T. Shah, N. L. Carr, A. T. Bell, Chem. Eng. Sci. 39 (1984), 905-907.

[149] M. A. Matthews, A. Akgerman, AICHE J. 33 (1987), 881-885.

[150] Z. Zhao, D. E. Resasco (unpublished).

[151] M. Haruta, T. Kobayashi, H. Sano, N. Yamada, Chem. Lett. 16 (1987), 405-408.

[152] M. Date, M. Okumura, S. Tsubota, M. Haruta, Angew. Chem. Int. Ed. 43 (2004), 2129-2132.

[153] C. J. Karwacki, P. Ganesh, P. R. C. Kent, W. O. Gordon, G. W. Peterson, J. Niu, Y. Gogotsi, J. Mater. Chem. A 1 (2013), 6051-6062.

[154] J. Saavedra, T. Whittaker, Z. Chen, C. J. Pursell, R. M. Rioux, B. D. Chandler, Nat. Chem. 8 (2016), 584-589.

[155] M. Ojeda, E. Iglesia, Chem. Commun. 0 (2009), 352-354.

[156] S. Lee, L. M. Molina, M. J. Lopez, J. A. Alonso, B. Hammer, B. Lee, S. Seifert, R. E. Winans, J. W. Elam, M. J. Pellin, Angew. Chem. Int. Ed. 48 (2009), 1467-1471.

[157] D. M. Perez Ferrandez, I. Herguedas Fernandez, M. P. G. Teley, M. H. J. M. de Croon, J. C. Schouten, T. A. Nijhuis, J. Catal. 330 (2015), 396-405.

[158] X. Nie, W. Luo, M. J. Janik, A. Asthagiri, J. Catal. 312 (2014), 108-122.

[159] K. L. Miller, C. W. Lee, J. L. Falconer, J. W. Medlin, J. Catal. 275 (2010), 294-299.

[160] L. Yang, Y. Choi, W. Qin, H. Chen, K. Blinn, M. Liu, P. Liu, J. Bai, T. A. Tyson, M. Liu, Nat. Commun. 2 (2011), 357-365.

[161] R. Ren, Y. Zhang, S. Liu, Z. Zuo, Y. Lu, Int. J. Hydrogen Energy 41 (2016), 2411-2423.

[162] R. Zhang, H. Liu, B. Wang, L. Ling, J. Phys. Chem. C 116 (2012), 22266-22280.

[163] T. Jekewitz, N. Blickhan, S. Endres, A. Drochner, H. Vogel, Catal. Commun. 20 (2012), 25-28.

[164] M. Ai, Catal. Today 42 (1998), 297-301.

[165] E. K. Novakova, E. G. Rounder, J. C. Vedrine, Catal. Lett. 83 (2002), 177-182.

[166] T. Petzold, N. Blickhan, A. Drochner, H. Vogel, ChemCatChem 6 (2014), 2053-2058.

[167] H. Su, M. Yang, X. Bao, W. Li, J. Phys. Chem. C 112 (2008), 17303-17310.

[168] K. de Wispelaere, K. Hemelsoet, M. Waroquier, V. van Speybroeck, J. Catal. 305 (2013), 76-80.

[169] C. Michel, J. Zaffran, A. M. Ruppert, J. Matras-Michalska, M. Jedrzejczyk, J. Grams, P. Sautet, Chem. Commun. 50 (2014), 12450-12453.

[170] E. du Toit, W. Nicol, Appl. Catal., A 277 (2004), 219-225.

[171] P. H. Bolt, F. H. P. M. Habraken, J. W. Geus, J. Solid State Chem. 135 (1998), 59-69.

[172] J. Chen, X. Wang, H. Xiang, Y. Sun, Stud. Surf. Sci. Catal. 136 (2001), 525-529.

[173] J. Chen, H. Xiang, H. Gao, Y. Sun, React. Kinet. Catal. Lett. 73 (2001), 169-177.

[174] E. van Steen, M. Claeys, M. E. Dry, J. van de Loosdrecht, E. L. Viljoen, J. L. Visagie, J. Phys. Chem. B 109 (2005), 3575-3577.

[175] L. Zhang, K. Chen, B. Chen, J. L. White, D. E. Resasco, J. Am. Chem. Soc. 137 (2015), 11810-11819.

[176] T. J. Donnelly, C. N. Satterfield, Appl. Catal., A 52 (1989), 93-114.

[177] D. B. Bukur, S. A. Patel, X. Lang, Appl. Catal., A 61 (1990), 329-349.

[178] Y. Wang, X. Zhu, M. Crocker, B. Chen, C. Shi, Appl. Catal., B 160-161 (2014), 542-551.

[179] Y. A. Saleh-Alhamed, R. R. Hudgins, P. L. Silveston, J. Catal. 161 (1996), 430-440.

[180] W. Bu, L. Zhao, Z. Zhang, X. Zhang, J. Gao, C. Xu, Appl. Surf. Sci. 289 (2014), 6-13.

[181] B. G. Johnson, C. H. Bartholomew, D. W. Goodman, J. Catal. 128 (1991), 231-247.

[182] A. Tavasoli, R. M. Malek Abbaslou, A. K. Dalai, Appl. Catal., A 346 (2008), 58-64.

[183] A. Tavasoli, M. Irani, R. M. Malek Abbaslou, M. Trepanier, A. K. Dalai, Can. J. Chem. Eng. 86 (2008), 1070-1080.

[184] D. Schanke, A. M. Hilmen, E. Bergene, K. Kinnari, E. Rytter, E. Adnanes, A. Holmen, Catal. Lett. 34 (1995), 269-284.

[185] D. Schanke, A. M. Hilmen, E. Bergene, K. Kinnari, E. Rytter, E. Adnanes, A. Holmen, Energy Fuels 10 (1996), 867-872.

[186] A. M. Hilmen, D. Schanke, A. Holmen, Stud. Surf. Sci. Catal. 107 (1997), 237-242.

[187] A. K. Dalai, T. K. Das, K. V. Chaudhari, G. Jacobs, B. H. Davis, Appl. Catal., A 289 (2005), 135-142.

[188] T. K. Das, X. Zhan, J. Li, G. Jacobs, M. E. Dry, B. H. Davis, Stud. Surf. Sci. Catal. 163 (2007), 289-312.

[189] T. K. Das, W. A. Conner, G. Jacobs, J. Li, K. Chaudhari, B. H. Davis, Stud. Surf. Sci. Catal. 147 (2004), 331-336.

[190] T. K. Das, W. A. Conner, J. Li, G. Jacobs, M. E. Dry, B. H. Davis, Energy Fuels 19 (2005), 1430-1439.

[191] G. Jacobs, T. K. Das, J. Li, M. Luo, P. M. Patterson, B. H. Davis, Stud. Surf. Sci. Catal. 163 (2007), 217-253.

[192] G. Kiss, C. E. Kliewer, G. J. DeMartin, C. C. Culross, J. E. Baumgartner, J. Catal. 217 (2003), 127-140.

[193] P. J. van Berge, J. van de Loosdrecht, S. Barradas, A. M. van der Kraan, Catal. Today 58 (2000), 321-334.

[194] F. M. Gottschalk, R. G. Copperthwaite, M. van der Riet, G. J. Hutchings, Appl. Catal., A 38 (1988), 103-108.

[195] W. H. Zimmerman, D. B. Bukur, Can. J. Chem. Eng. 68 (1990), 292-301.

[196] G. P. van der Laan, A. A. C. M. Beenackers, Appl. Catal., A 193 (2000), 39-53.

[197] R. A. van Santen, I. M. Ciobica, E. van Steen, M. M. Ghouri, Adv. Catal. 54 (2011), 127-187.

[198] N. E. Tsakoumis, M. Ronning, O. Borg, E. Rytter, A. Holmen, Catal. Today 154 (2010), 162-182.

[199] C. H. Bartholomew, Appl. Catal., A 212 (2001), 17-60.

[200] W. Zhou, J. Chen, K. Fang, Y. Sun, Fuel Process. Technol. 87 (2006), 609-616.

[201] L. Shi, J. Chen, K. Fang, Y. Sun, Stud. Surf. Sci. Catal. 167 (2007), 97-102.

[202] G. W. Huber, C. G. Guymon, T. L. Conrad, B. C. Stephenson, C. H. Bartholomew, Stud. Surf. Sci. Catal. 139 (2001), 423-430.

[203] L. Liu, G. Sun, C. Wang, J. Yang, C. Xiao, H. Wang, D. Ma, Y. Kou, Catal. Today 183 (2012), 136-142.

[204] K. Chen, J. Kelsey, J. L. White, L. Zhang, D. E. Resasco, ACS Catal. 5 (2015), 7480-7487.

[205] M. A. Henderson, Surf. Sci. Rep. 46 (2002), 1-308.

[206] K. Chen, J. Damron, C. Pearson, D. E. Resasco, L. Zhang, J. L. White, ACS Catal. 4 (2014), 3039-3044.

[207] E. Rytter, A. Holmen, Catal. Today 275 (2016), 11-19.

[208] E. Rytter, A. Holmen, ACS Catal. 7 (2017), 5321-5328.

[209] J. Li, G. Jacobs, T. K. Das, B. H. Davis, Appl. Catal., A 233 (2002), 255-262.

[210] E. Jimenez-Barrera, P. Bazin, C. Lopez-Cartes, F. Romero-Sarria, M. Daturi, J. A. Odriozola, Appl. Catal., B 237 (2018), 986-995.

[211] P. A. Zapata, Y. Huang, M. A. Gonzalez-Borja, D. E. Resasco, J. Catal. 308 (2013), 82-97.

[212] Y. Wang, M. Lieberman, Langmuir 19 (2003), 1159-1167.

[213] X. Huang, Y. Men, J. Wang, W. An, Y. Wang, Catal. Sci. Technol. 7 (2017), 168-180.

[214] C. Angelici, M. E. Z. Velthoen, B. M. Weckhuysen, P. C. A. Bruijnincx, Catal. Sci. Technol. 5 (2015), 2869-2879.

[215] R. He, Y. Men, X. Huang, J. Wang, S. Li, X. Wang, Chem. Lett. 47 (2018), 1097-1100.

[216] Q. Zhu, B. Wang, T. Tan, ACS Sustainable Chem. Eng. 5 (2017), 722-733.

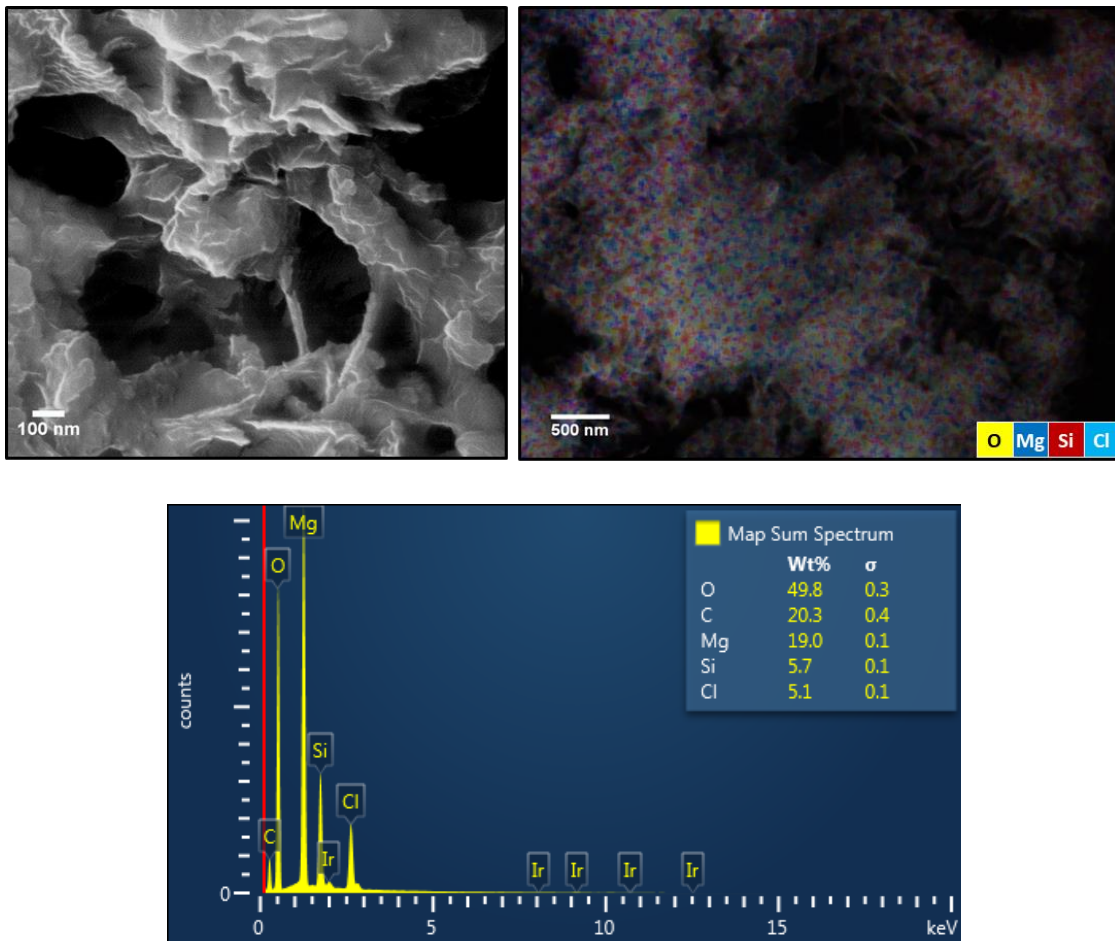# Appendix A. Electron microscopy images
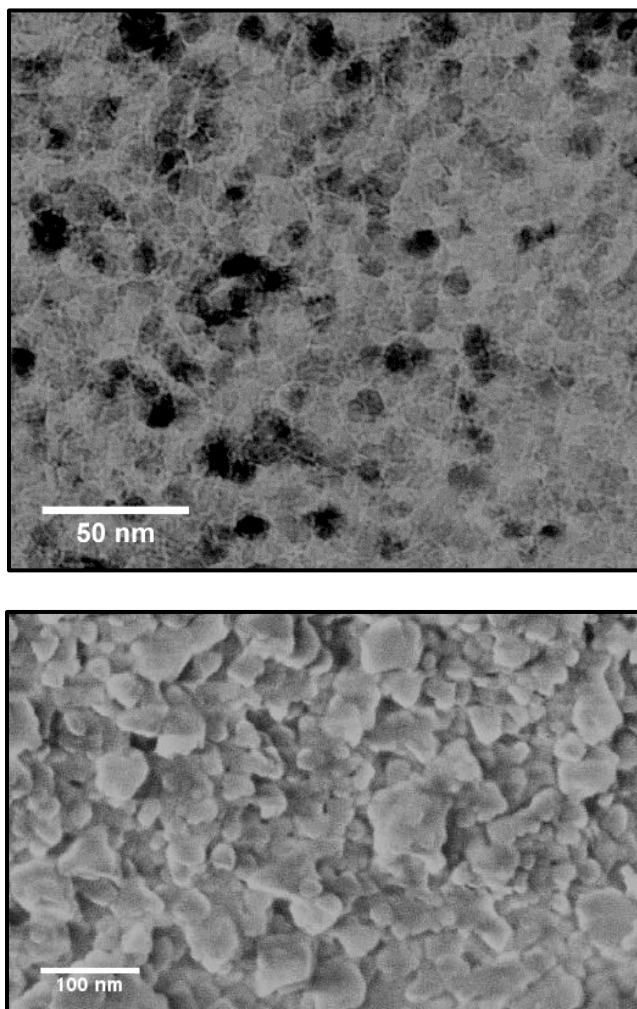
Figure A-1. TEM and SEM images of MgO-NC.
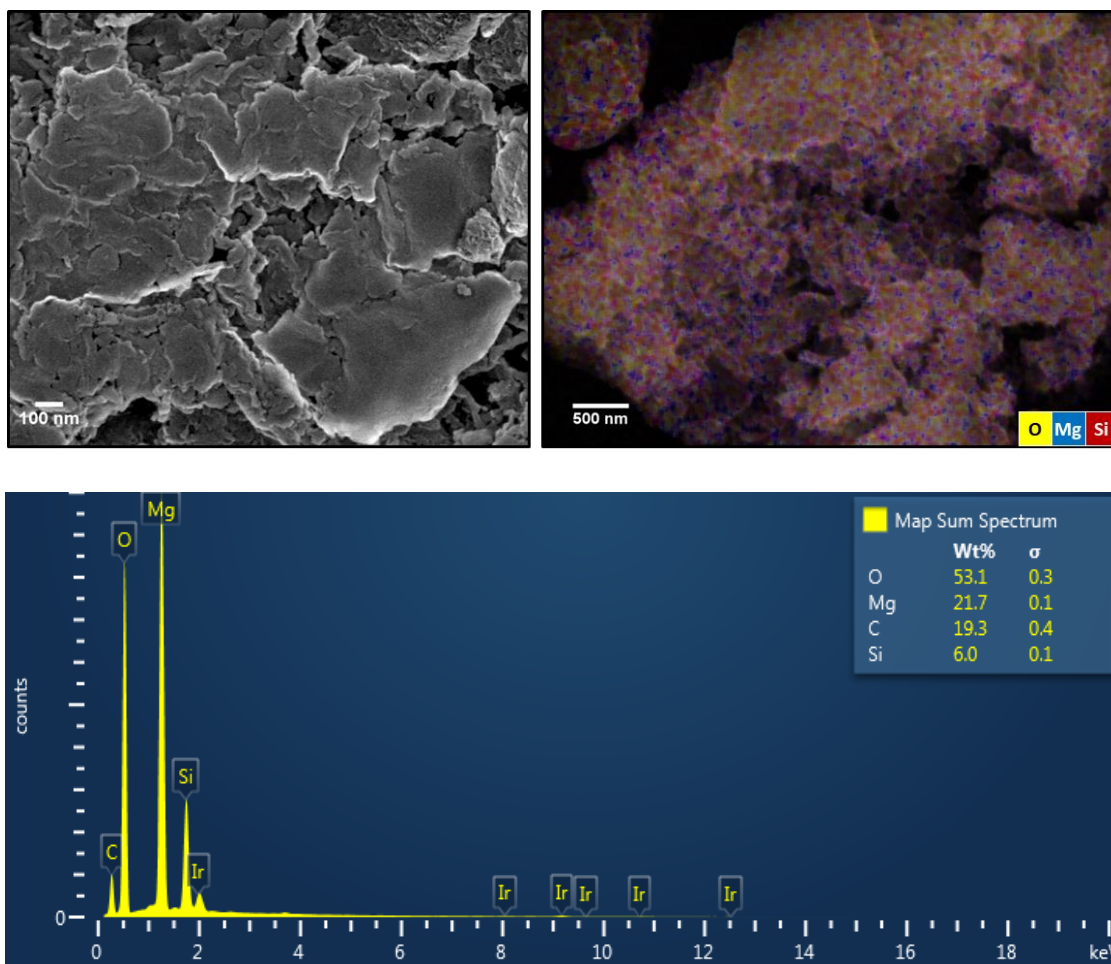
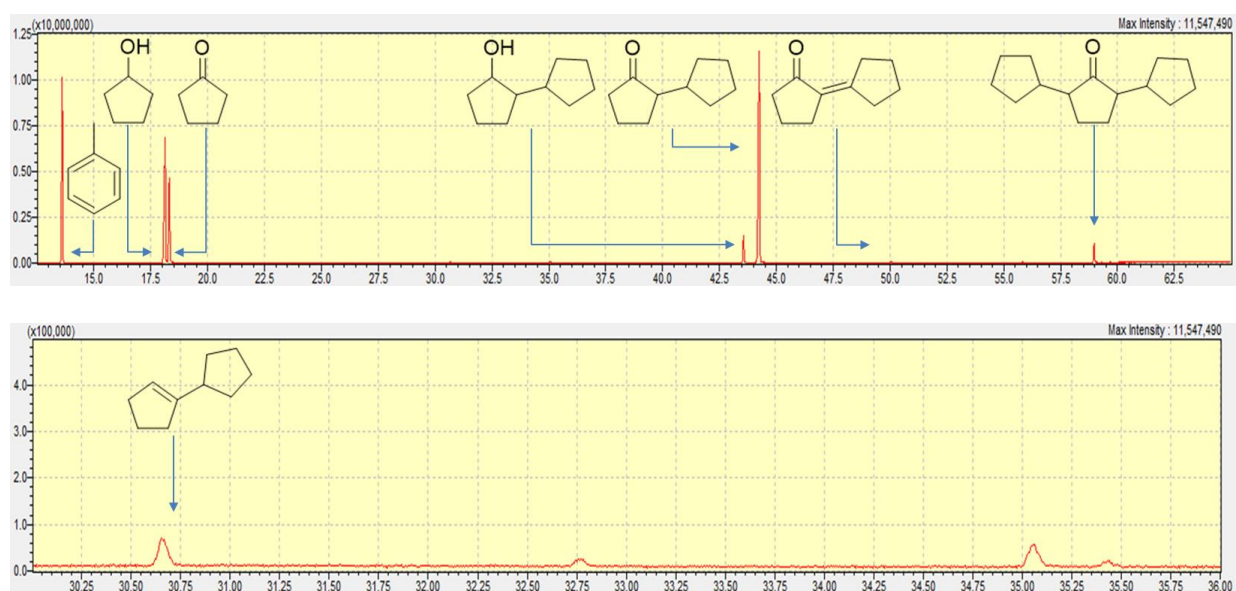**Figure A-2.** SEM image, elemental map and EDS spectrum of MgO@mSiO$_2$.

Figure A-3. SEM image, elemental map and EDS spectrum of MgO@mSiO$_2$-OTS.

Appendix B. Identification of cyclopentanone self-aldol condensation products at high hydrogen pressures

Reaction conditions: 0.25 g of MgO-NC + 0.25 g of 10 wt.% Cu/SiO_2, $C_{cyclopentanone\ 0} = 1.8$ M, 150°C, 400 psia in H_2, 8 hours.

Appendix C. Identification of cyclopentanone self-aldol condensation products at low hydrogen pressures

Reaction conditions: 0.25 g of MgO-NC + 0.25 g of 10 wt.% Cu/SiO_2, $C_{cyclopentanone\ 0}$ = 1.8 M, 150°C, 20 psia in H_2, 8 hours.
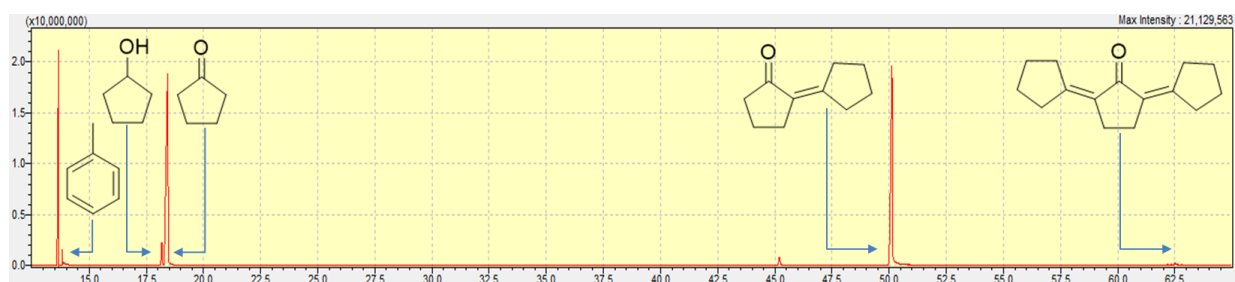
Appendix D. Identification of cyclopentanone-acetone cross-aldol condensation products

Reaction conditions: 0.20 g of MgO-NC, $C_{cyclopentanone\ 0} = C_{acetone\ 0} = 1.0$ M, 200°C, 450 psia in N_2, 2 hours.
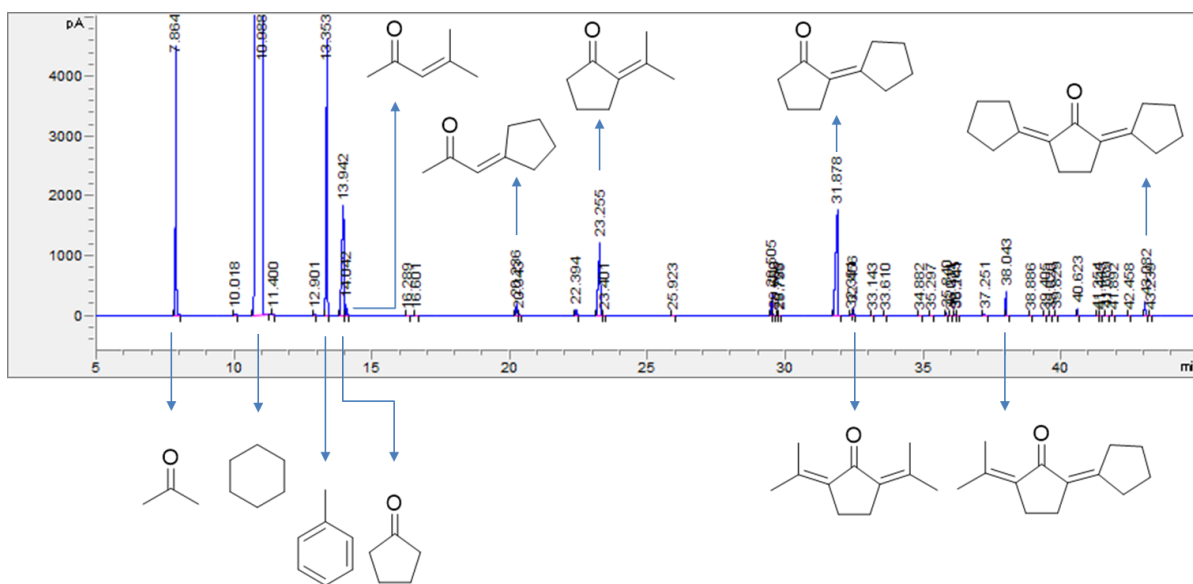
Appendix E. **The cross-aldol condensation of cyclopentanone (C) and benzophenone (B) in decalin: rate of formation of [C]-activated products and product distribution as functions of the feed ratio**

Reaction conditions: 0.25 g of MgO-NC, $C_{cyclopentanone\ 0} = 1.0$ M, 250°C, 400 psia in N_2, 2 hours.
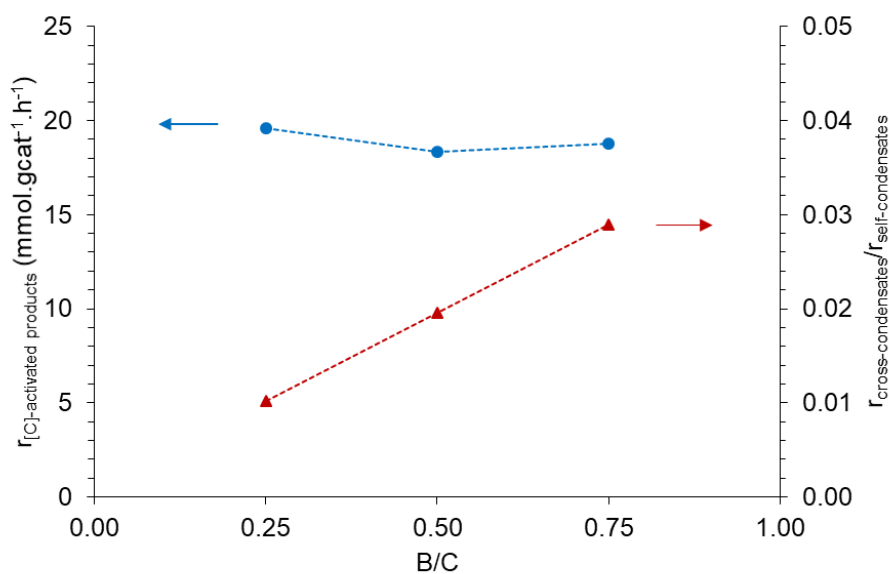
(*)   [C]C, C[C]C and tridane are detectable self-condensates.

(**)   [C]B is the only detectable cross-condensate.

Appendix F. Estimation of the maximum water vapor volume added to a cyclopentanone self-aldol condensation reaction system

First, the maximum mole of water vapor was calculated from the ideal gas equation:

$$pV = nRT$$

where

p   =   saturated vapor pressure of water at 473K = 15.3 atm

V   =   empty space of the Parr reactor = 0.050 L

R =   ideal gas constant = 0.082 L.atm.mol^{-1}.K^{-1}

T   =   reaction temperature = 473K

n   =   maximum mole of water vapor in the Parr reactor at 473K

$$n = \frac{pV}{RT} = \frac{15.3 \text{ atm} \times 0.050 \text{ L}}{0.082 \frac{\text{L.atm}}{\text{mol.K}} \times 473\text{K}} = 0.0197 \text{ mol}$$
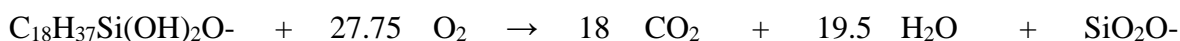
Then, the maximum volume of water vapor added to the reaction system was determined from molecular weight and density:

$$V_{\text{water vapor max}} = \frac{m}{\rho} = \frac{nM}{\rho} = \frac{0.0197 \text{ mol} \times 18 \frac{\text{g}}{\text{mol}}}{1 \frac{\text{g}}{\text{mL}}} = 0.355 \text{ mL} = 355 \text{ }\mu\text{L}$$

Appendix G. TGA-based OTS content of OTS-functionalized MgO

The OTS content of an OTS-functionalized MgO was determined from two peaks of the water mass spectrum. Beyond 250°C, a T^1 OTS anchor – monodentate-bonded to the catalytic surface – undergoes combustion as follows:

$$C_{18}H_{37}Si(OH)_2O\text{-} \quad + \quad 27.75 \quad O_2 \quad \rightarrow \quad 18 \quad CO_2 \quad + \quad 19.5 \quad H_2O \quad + \quad SiO_2O\text{-}$$

- MgO@mSiO$_2$-OTS (**Figure 2**)

$m_{H_2O \text{ physisorption}} = 47.48 \text{ mg} \times 5.22\% = 2.48 \text{ mg}$

$m_{H_2O \text{ OTS-combustion}} = \dfrac{A_{\text{OTS-combustion}}}{A_{\text{physisorption}}} \times m_{H_2O \text{ physisorption}} = 3.34 \times 2.48 \text{ mg} = 8.28 \text{ mg}$

$m_{C_{18}H_{37}Si(OH)_2O\text{-}} = \dfrac{1}{19.5} \times \dfrac{m_{H_2O \text{ OTS-combustion}}}{MW_{H_2O}} \times MW_{C_{18}H_{37}Si(OH)_2O\text{-}}$

$$= \dfrac{1}{19.5} \times \dfrac{8.28 \text{ mg}}{18 \frac{g}{mol}} \times 331 \frac{g}{mol} = 7.80 \text{ mg}$$

$\%wt_{C_{18}H_{37}Si(OH)_2O\text{-}} = \dfrac{m_{C_{18}H_{37}Si(OH)_2O\text{-}}}{m_{\text{sample}} - m_{H_2O \text{ physisorption}}} = \dfrac{7.80 \text{ mg}}{47.48 \text{ mg} - 2.48 \text{ mg}} \times 100\% = 17.34\%$

- MgO-OTS (**Figure 27**)

$$m_{H_2O \text{ physisorption}} = 46.91 \text{ mg} \times 6\% = 2.81 \text{ mg}$$
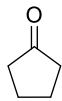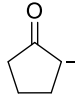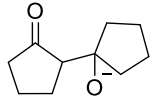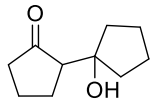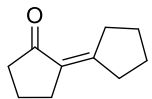
$$m_{H_2O \text{ OTS-combustion}} = \frac{A_{OTS\text{-combustion}}}{A_{physisorption}} \times m_{H_2O \text{ physisorption}} = 2.01 \times 2.81 \text{ mg} = 5.65 \text{ mg}$$

$$m_{C_{18}H_{37}Si(OH)_2O\text{-}} = \frac{1}{19.5} \times \frac{m_{H_2O \text{ OTS-combustion}}}{MW_{H_2O}} \times MW_{C_{18}H_{37}Si(OH)_2O\text{-}}$$

$$= \frac{1}{19.5} \times \frac{5.65 \text{ mg}}{18 \frac{g}{mol}} \times 331 \frac{g}{mol} = 5.33 \text{ mg}$$

$$\%wt_{C_{18}H_{37}Si(OH)_2O\text{-}} = \frac{m_{C_{18}H_{37}Si(OH)_2O\text{-}}}{m_{sample} - m_{H_2O \text{ physisorption}}} = \frac{5.33 \text{ mg}}{46.91 \text{ mg} - 2.81 \text{ mg}} \times 100\% = 12.08\%$$

Appendix H. Derivation of cyclopentanone self-aldol condensation initial rates on the MgO-NC catalytic surface

Denotations:

k	rate constant
K	equilibrium constant
C_t	total amount of sites
DP	deprotonation
C-C	C-C coupling
RP	reprotonation
DH	dehydration
*	vacant site
C	
[C]	
[OX]	
OL	
[C]C	
W	

Scenario 1. Langmuir-Hinshelwood reaction model. Deprotonation is rate-limiting.
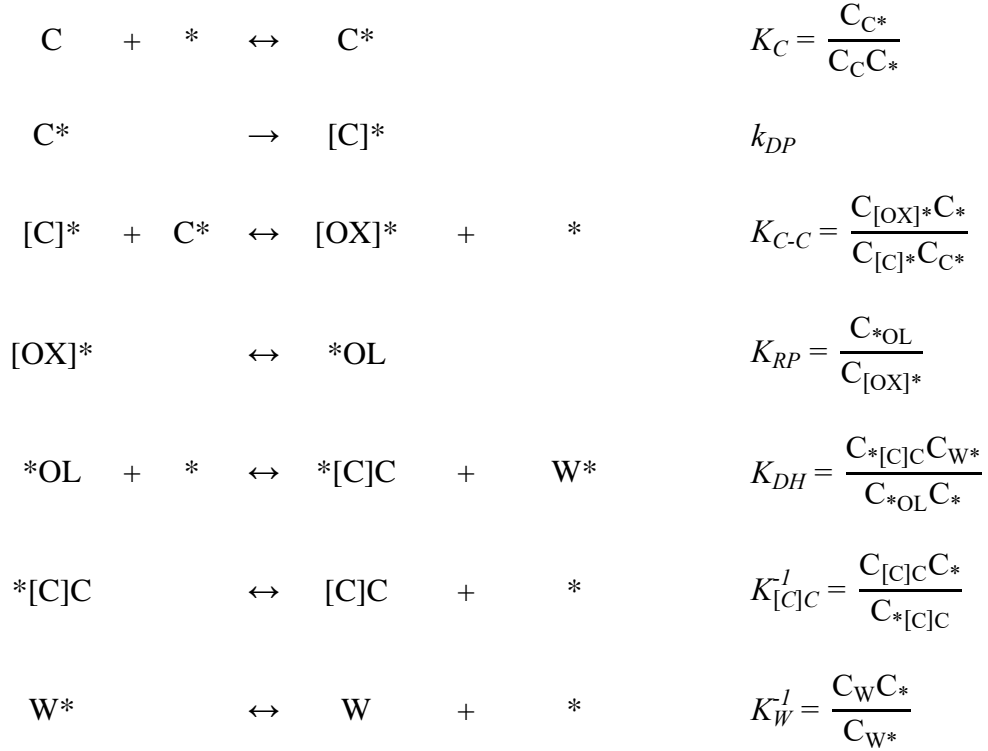
$$C \quad + \quad * \quad \leftrightarrow \quad C* \qquad\qquad K_C = \frac{C_{C*}}{C_C C_*}$$

$$C* \qquad\qquad \rightarrow \quad [C]* \qquad\qquad k_{DP}$$

$$[C]* \quad + \quad C* \quad \leftrightarrow \quad [OX]* \quad + \quad * \qquad\qquad K_{C\text{-}C} = \frac{C_{[OX]*} C_*}{C_{[C]*} C_{C*}}$$

$$[OX]* \qquad\qquad \leftrightarrow \quad *OL \qquad\qquad K_{RP} = \frac{C_{*OL}}{C_{[OX]*}}$$

$$*OL \quad + \quad * \quad \leftrightarrow \quad *[C]C \quad + \quad W* \qquad\qquad K_{DH} = \frac{C_{*[C]C} C_{W*}}{C_{*OL} C_*}$$

$$*[C]C \qquad\qquad \leftrightarrow \quad [C]C \quad + \quad * \qquad\qquad K_{[C]C}^{-1} = \frac{C_{[C]C} C_*}{C_{*[C]C}}$$

$$W* \qquad\qquad \leftrightarrow \quad W \quad + \quad * \qquad\qquad K_W^{-1} = \frac{C_W C_*}{C_{W*}}$$

$$C_t = C_* + C_{C*} + C_{[C]*} + C_{[OX]*} + C_{*OL} + C_{*[C]C} + C_{W*}$$

$$C_{C*} = K_C C_C C_*$$

$$C_{*[C]C} = K_{[C]C} C_{[C]C} C_*$$

$$C_{W*} = K_W C_W C_*$$

$$C_{*OL} = \frac{C_{*[C]C} C_{W*}}{K_{DH} C_*} = \frac{\left(K_{[C]C} C_{[C]C} C_* \right)\left(K_W C_W C_* \right)}{K_{DH} C_*} = \frac{K_{[C]C} K_W}{K_{DH}} C_{[C]C} C_W C_*$$

$$C_{[OX]*} = \frac{C_{*OL}}{K_{RP}} = \frac{K_{[C]C} K_W}{K_{RP} K_{DH}} C_{[C]C} C_W C_*$$

$$C_{[C]*} = \frac{C_{[OX]*} C_*}{K_{C\text{-}C} C_{C*}} = \frac{\left(\dfrac{K_{[C]C} K_W}{K_{RP} K_{DH}} C_{[C]C} C_W C_* \right) C_*}{K_{C\text{-}C} (K_C C_C C_*)} = \frac{K_{[C]C} K_W}{K_{C\text{-}C} K_{RP} K_{DH} K_C} \frac{C_{[C]C} C_W}{C_C} C_*$$

$$C_* = \cfrac{C_t}{1+K_C C_C+\cfrac{K_{[C]C}K_W}{K_{C\text{-}C}K_{RP}K_{DH}K_C}\cfrac{C_{[C]C}C_W}{C_C}+\cfrac{K_{[C]C}K_W}{K_{RP}K_{DH}}C_{[C]C}C_W+\cfrac{K_{[C]C}K_W}{K_{DH}}C_{[C]C}C_W+K_{[C]C}C_{[C]C}+K_W C_W}$$
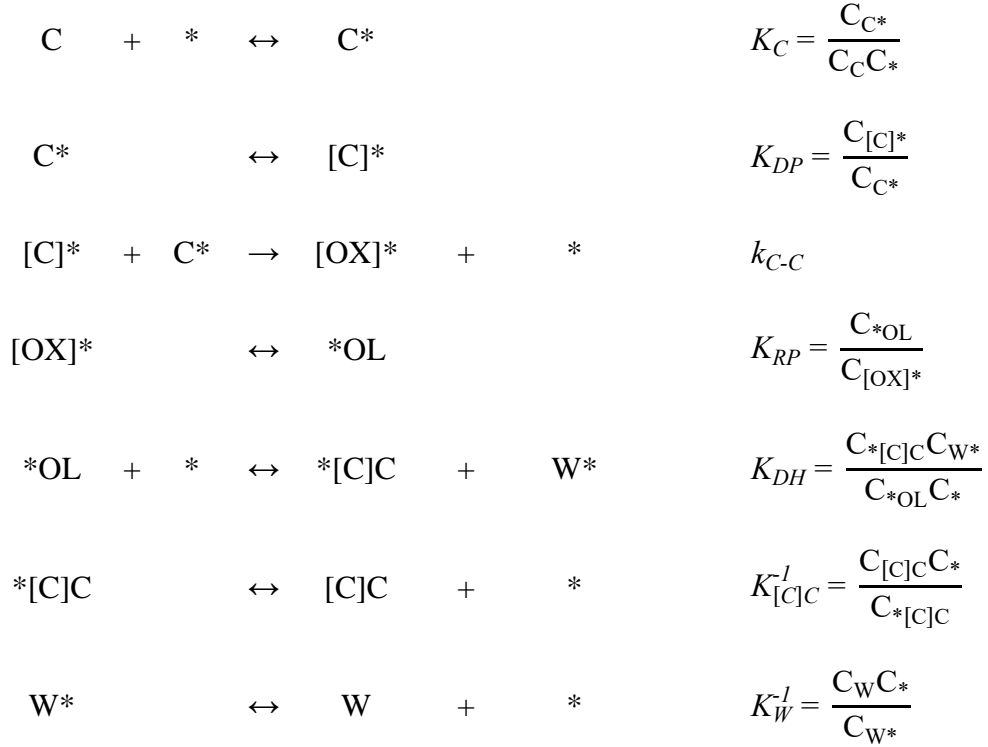
$$r = k_{DP}C_{C*} = k_{DP}(K_C C_C C_*)$$

$$r = \cfrac{k_{DP}C_t K_C C_C}{1+K_C C_C+\cfrac{K_{[C]C}K_W}{K_{C\text{-}C}K_{RP}K_{DH}K_C}\cfrac{C_{[C]C}C_W}{C_C}+\cfrac{K_{[C]C}K_W}{K_{RP}K_{DH}}C_{[C]C}C_W+\cfrac{K_{[C]C}K_W}{K_{DH}}C_{[C]C}C_W+K_{[C]C}C_{[C]C}+K_W C_W}$$

$$r_{\text{initial}} = \frac{k_{DP}C_t K_C C_C}{1+K_C C_C} = \frac{kK_C C_C}{1+K_C C_C}$$

Scenario 2. Langmuir-Hinshelwood reaction model. C-C coupling is rate-limiting.

$$C \quad + \quad * \quad \leftrightarrow \quad C* \qquad\qquad K_C = \frac{C_{C*}}{C_C C_*}$$

$$C* \quad\quad \leftrightarrow \quad [C]* \qquad\qquad K_{DP} = \frac{C_{[C]*}}{C_{C*}}$$

$$[C]* \quad + \quad C* \quad \rightarrow \quad [OX]* \quad + \quad * \qquad\qquad k_{C\text{-}C}$$

$$[OX]* \quad\quad \leftrightarrow \quad *OL \qquad\qquad K_{RP} = \frac{C_{*OL}}{C_{[OX]*}}$$

$$*OL \quad + \quad * \quad \leftrightarrow \quad *[C]C \quad + \quad W* \qquad\qquad K_{DH} = \frac{C_{*[C]C}C_{W*}}{C_{*OL}C_*}$$

$$*[C]C \quad\quad \leftrightarrow \quad [C]C \quad + \quad * \qquad\qquad K_{[C]C}^{-1} = \frac{C_{[C]C}C_*}{C_{*[C]C}}$$

$$W* \quad\quad \leftrightarrow \quad W \quad + \quad * \qquad\qquad K_W^{-1} = \frac{C_W C_*}{C_{W*}}$$

$$C_t = C_* + C_{C*} + C_{[C]*} + C_{[OX]*} + C_{*OL} + C_{*[C]C} + C_{W*}$$

$$C_{C*} = K_C C_C C_*$$

$$C_{*[C]C} = K_{[C]C}C_{[C]C}C_*$$

$$C_{W*} = K_W C_W C_*$$

$$C_{*OL} = \frac{C_{*[C]C}C_{W*}}{K_{DH}C_*} = \frac{\left(K_{[C]C}C_{[C]C}C_*\right)\left(K_W C_W C_*\right)}{K_{DH}C_*} = \frac{K_{[C]C}K_W}{K_{DH}}C_{[C]C}C_W C_*$$

$$C_{[OX]*} = \frac{C_{*OL}}{K_{RP}} = \frac{K_{[C]C}K_W}{K_{RP}K_{DH}}C_{[C]C}C_W C_*$$

$$C_{[C]*} = K_{DP}C_{C*} = K_{DP}K_C C_C C_*$$

$$C_* = \cfrac{C_t}{1+K_C C_C+K_{DP}K_C C_C+\cfrac{K_{[C]C}K_W}{K_{RP}K_{DH}}C_{[C]C}C_W+\cfrac{K_{[C]C}K_W}{K_{DH}}C_{[C]C}C_W+K_{[C]C}C_{[C]C}+K_W C_W}$$

$$r = k_{C\text{-}C}C_{[C]*}C_{C*} = k_{C\text{-}C}(K_{DP}K_C C_C C_*)(K_C C_C C_*) = k_{C\text{-}C}K_{DP}K_C^2 C_C^2 C_*^2$$

$$r = \cfrac{k_{C\text{-}C}K_{DP}C_t^2 K_C^2 C_C^2}{\left(1+K_C C_C+K_{DP}K_C C_C+\cfrac{K_{[C]C}K_W}{K_{RP}K_{DH}}C_{[C]C}C_W+\cfrac{K_{[C]C}K_W}{K_{DH}}C_{[C]C}C_W+K_{[C]C}C_{[C]C}+K_W C_W\right)^2}$$

$$r_{\text{initial}} = \cfrac{k_{C\text{-}C}K_{DP}C_t^2 K_C^2 C_C^2}{(1+K_C C_C+K_{DP}K_C C_C)^2} = \cfrac{k'K_C^2 C_C^2}{(1+K_C C_C+K_{DP}K_C C_C)^2}$$

Scenario 3. Eley-Rideal reaction model. C-C coupling is rate-limiting.

$$\text{C} \quad + \quad * \quad \leftrightarrow \quad \text{C*} \qquad\qquad K_C = \frac{C_{C*}}{C_C C_*}$$

$$\text{C*} \qquad\qquad \leftrightarrow \quad \text{[C]*} \qquad\qquad K_{DP} = \frac{C_{[C]*}}{C_{C*}}$$

$$\text{[C]*} \quad + \quad \text{C} \quad \rightarrow \quad \text{[OX]*} \qquad\qquad k'_{C\text{-}C}$$

$$\text{[OX]*} \qquad\qquad \leftrightarrow \quad \text{*OL} \qquad\qquad K_{RP} = \frac{C_{*OL}}{C_{[OX]*}}$$

$$\text{*OL} \quad + \quad * \quad \leftrightarrow \quad \text{*[C]C} \quad + \quad \text{W*} \qquad\qquad K_{DH} = \frac{C_{*[C]C} C_{W*}}{C_{*OL} C_*}$$

$$\text{*[C]C} \qquad\qquad \leftrightarrow \quad \text{[C]C} \quad + \quad * \qquad\qquad K_{[C]C}^{-1} = \frac{C_{[C]C} C_*}{C_{*[C]C}}$$

$$\text{W*} \qquad\qquad \leftrightarrow \quad \text{W} \quad + \quad * \qquad\qquad K_W^{-1} = \frac{C_W C_*}{C_{W*}}$$

$$C_t = C_* + C_{C*} + C_{[C]*} + C_{[OX]*} + C_{*OL} + C_{*[C]C} + C_{W*}$$

$$C_{C*} = K_C C_C C_*$$

$$C_{*[C]C} = K_{[C]C} C_{[C]C} C_*$$

$$C_{W*} = K_W C_W C_*$$

$$C_{*OL} = \frac{C_{*[C]C} C_{W*}}{K_{DH} C_*} = \frac{\left(K_{[C]C} C_{[C]C} C_*\right)\left(K_W C_W C_*\right)}{K_{DH} C_*} = \frac{K_{[C]C} K_W}{K_{DH}} C_{[C]C} C_W C_*$$

$$C_{[OX]*} = \frac{C_{*OL}}{K_{RP}} = \frac{K_{[C]C} K_W}{K_{RP} K_{DH}} C_{[C]C} C_W C_*$$
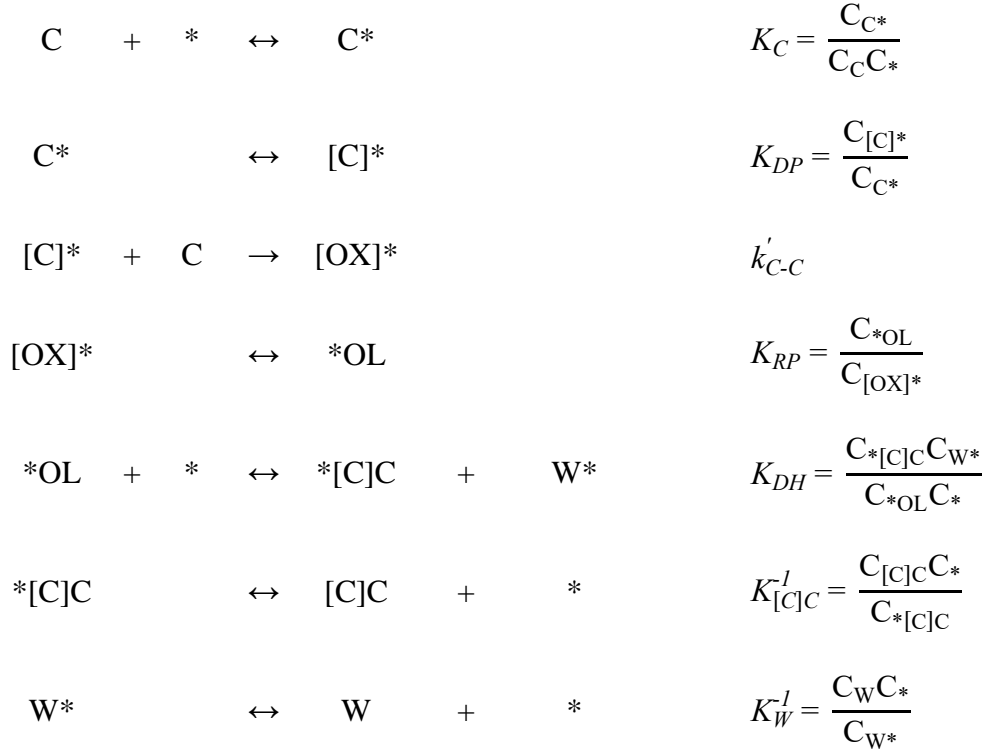
$$C_{[C]*} = K_{DP} C_{C*} = K_{DP} K_C C_C C_*$$

$$C_* = \frac{C_t}{1 + K_C C_C + K_{DP} K_C C_C + \dfrac{K_{[C]C} K_W}{K_{RP} K_{DH}} C_{[C]C} C_W + \dfrac{K_{[C]C} K_W}{K_{DH}} C_{[C]C} C_W + K_{[C]C} C_{[C]C} + K_W C_W}$$

$$r = k'_{C\text{-}C} C_{[C]*} C_C = k'_{C\text{-}C} (K_{DP} K_C C_C C_*) C_C = k'_{C\text{-}C} K_{DP} K_C C_C^2 C_*$$

$$r = \frac{k'_{C\text{-}C} C_t K_{DP} K_C C_C^2}{1 + K_C C_C + K_{DP} K_C C_C + \dfrac{K_{[C]C} K_W}{K_{RP} K_{DH}} C_{[C]C} C_W + \dfrac{K_{[C]C} K_W}{K_{DH}} C_{[C]C} C_W + K_{[C]C} C_{[C]C} + K_W C_W}$$

$$r_{\text{initial}} = \frac{k'_{C\text{-}C} C_t K_{DP} K_C C_C^2}{1 + K_C C_C + K_{DP} K_C C_C} = \frac{k'' K_{DP} K_C C_C^2}{1 + K_C C_C + K_{DP} K_C C_C}$$

134

Appendix I. Linearization of cyclopentanone self-aldol condensation initial rates derived from Langmuir-Hinshelwood and Eley-Rideal reaction models

| Model	RDS	Initial rate expression	Linearized function
L-H	Deprotonation	$r = \dfrac{kK_C C_C}{1+K_C C_C}$	$\dfrac{1}{r} = \dfrac{1}{kK_C}\dfrac{1}{C_C}+\dfrac{1}{k}$
L-H	C-C coupling	$r = \dfrac{k' K_C^2 C_C^2}{(1+K_C C_C + K_{DP}K_C C_C)^2}$	$\dfrac{1}{\sqrt{r}} = \dfrac{1}{K_C\sqrt{k'}}\dfrac{1}{C_C}+\dfrac{1+K_{DP}}{\sqrt{k'}}$
E-R	C-C coupling	$r = \dfrac{k'' K_{DP}K_C C_C^2}{1+K_C C_C + K_{DP}K_C C_C}$	$\dfrac{C_C^2}{r} = \dfrac{1+K_{DP}}{k'' K_{DP}}C_C+\dfrac{1}{k'' K_{DP}K_C}$
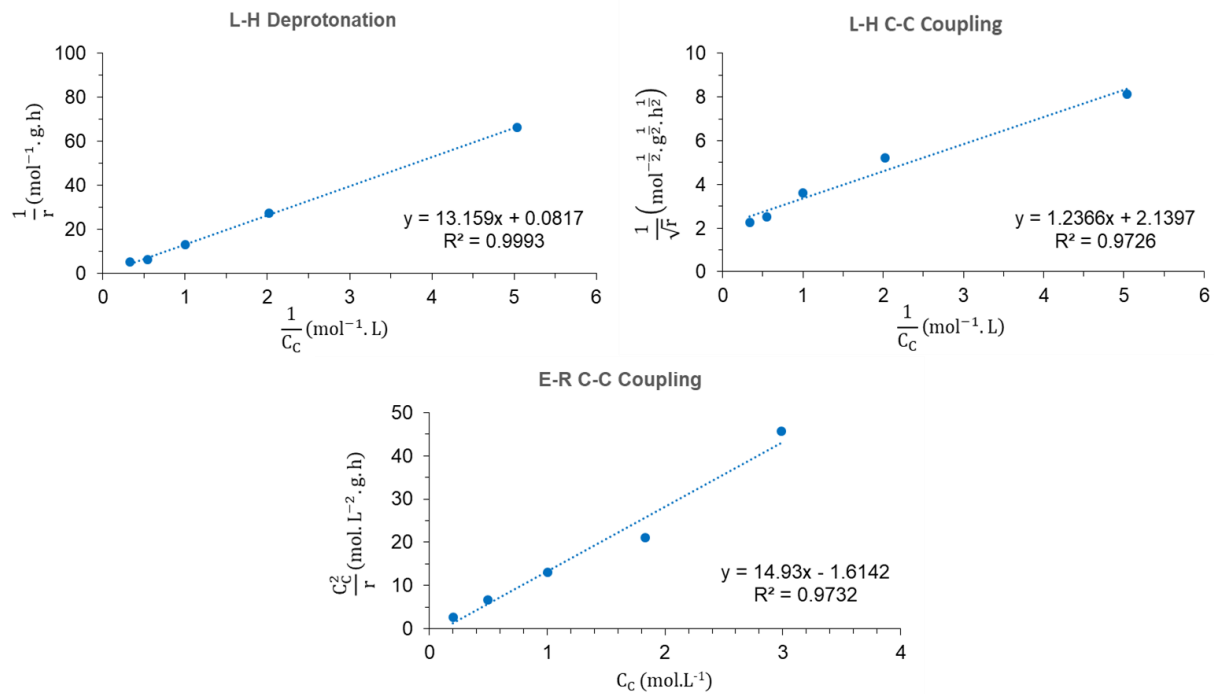
Figure I-1. Linearization of initial rates on MgO-NC.

<u>Reaction conditions:</u> 0.25 g of MgO-NC, 50 mL of feed, 150°C, 20 mins.
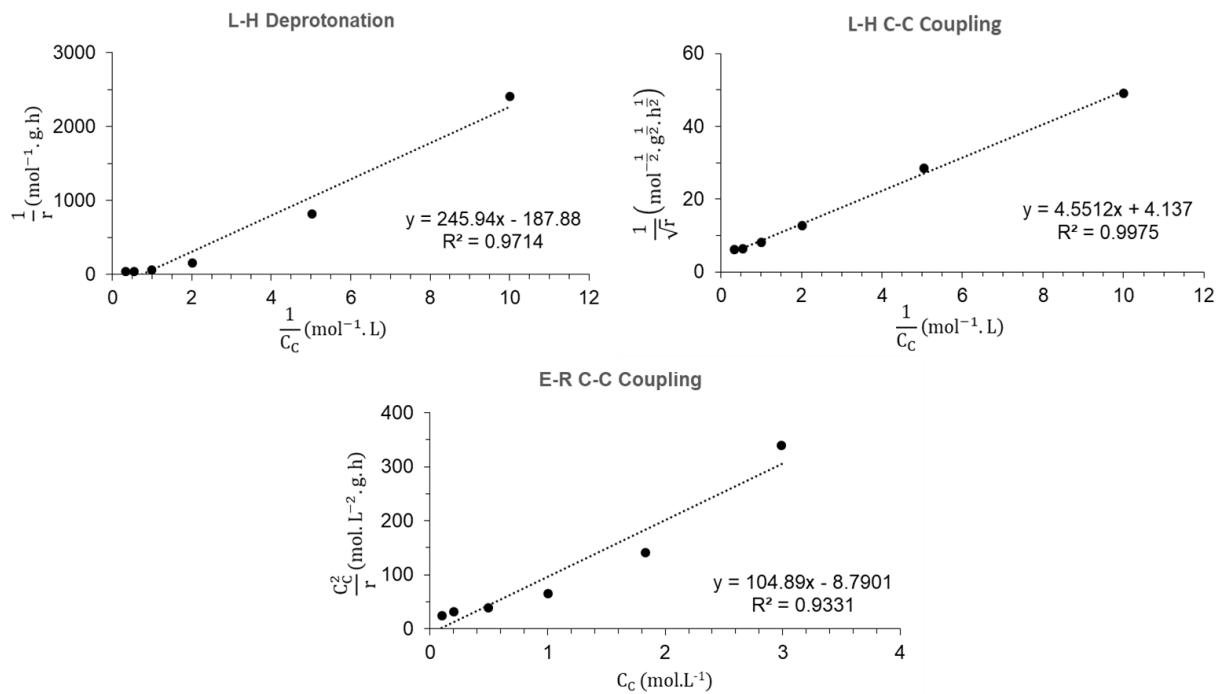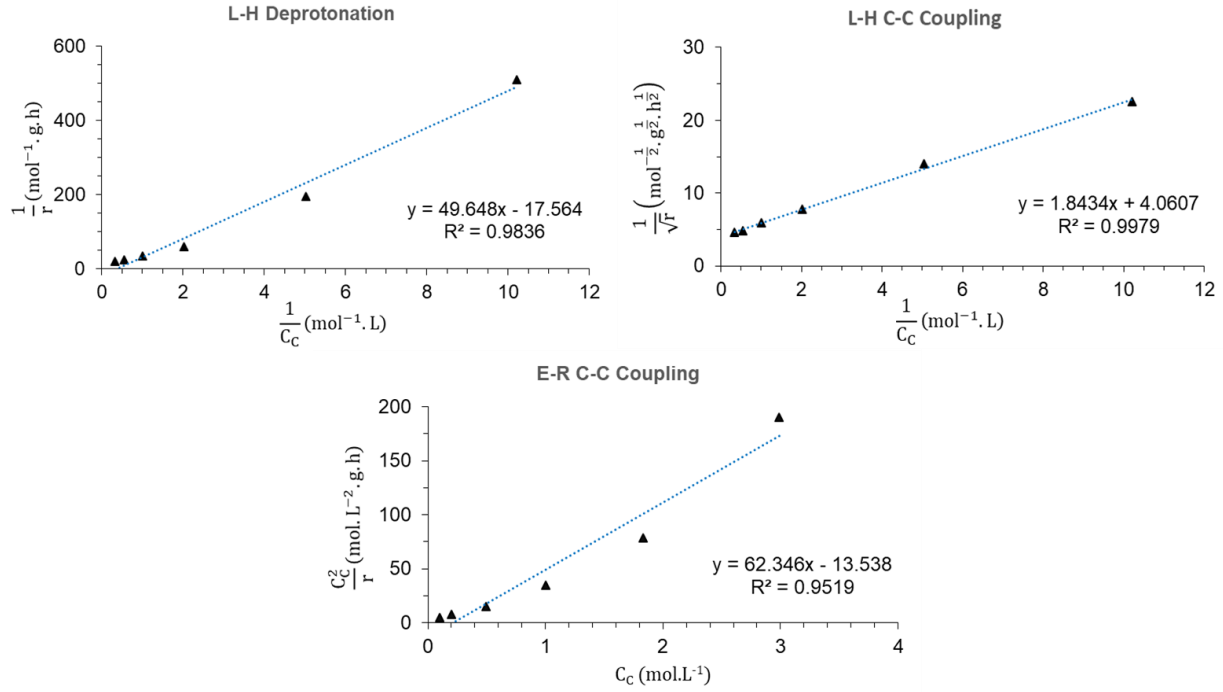
Figure I-2. Linearization of initial rates on MgO(70)-OTS(30).

Reaction conditions: 0.50 g of MgO(70)-OTS(30), 50 mL of feed, 200°C, 1 hour.
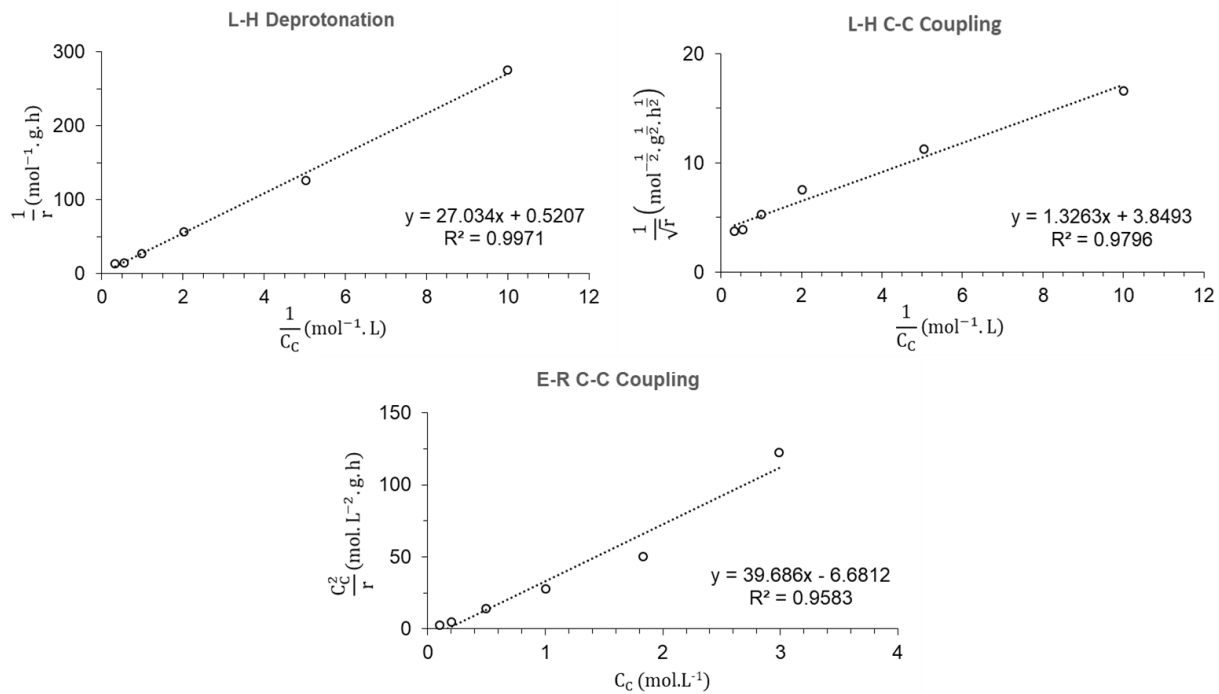
Figure I-3. Linearization of initial rates on MgO(70)-OTS(30) PC.

<u>Reaction conditions:</u> 0.325 g of MgO(70)-OTS(30) PC, 50 mL of feed, 200°C, 1 hour.

L-H Deprotonation

$y = 49.648x - 17.564$
$R^2 = 0.9836$

$\frac{1}{r}\ (\mathrm{mol^{-1}.g.h})$

$\frac{1}{C_C}\ (\mathrm{mol^{-1}.L})$

L-H C-C Coupling

$y = 1.8434x + 4.0607$
$R^2 = 0.9979$

$\frac{1}{\sqrt{r}}\left(\mathrm{mol^{-\frac{1}{2}}.g^{\frac{1}{2}}.h^{\frac{1}{2}}}\right)$

$\frac{1}{C_C}\ (\mathrm{mol^{-1}.L})$

E-R C-C Coupling

$y = 62.346x - 13.538$
$R^2 = 0.9519$

$\frac{C_C^2}{r}\ (\mathrm{mol.L^{-2}.g.h})$

$C_C\ (\mathrm{mol.L^{-1}})$

Figure I-4. Linearization of initial rates on MgO(70)-OTS(30) with added water.

<u>Reaction conditions:</u> 0.50 g of MgO(70)-OTS(30), 50 mL of feed, 355 µL of water, 200°C, 1 hour.

$$\frac{\mathrm{Slope_{MgO\text{-}OTS\ water}}}{\mathrm{Slope_{MgO\text{-}OTS}}} = \frac{\dfrac{1}{K_C\sqrt{k'_{water}}}}{\dfrac{1}{K_C\sqrt{k'}}} = \sqrt{\frac{k'}{k'_{water}}} = \sqrt{\frac{k_{C\text{-}C}K_{DP}C_t^2}{k_{C\text{-}C\ water}K_{DP}C_t^2}} = \sqrt{\frac{k_{C\text{-}C}}{k_{C\text{-}C\ water}}}$$

$$= \sqrt{\exp\left(-\frac{E_{a\ C\text{-}C} - E_{a\ C\text{-}C\ water}}{RT}\right)}$$

$$E_{a\ C\text{-}C\ water} - E_{a\ C\text{-}C} = 2RT\ln\left(\frac{\mathrm{Slope_{MgO\text{-}OTS\ water}}}{\mathrm{Slope_{MgO\text{-}OTS}}}\right)$$

$$= 2 \times 8.314 \times 10^{-3}\ \frac{\mathrm{kJ}}{\mathrm{mol.K}} \times 473\mathrm{K} \times \ln\left(\frac{1.84}{4.55}\right)$$

$$= -7.11\ \frac{\mathrm{kJ}}{\mathrm{mol}}$$